Luminescence in Two-Dimensional Materials and van der Waals Heterostructures

*Wenjing Jie, Zhibin Yang, Gongxun Bai, and Jianhua Hao**

Dr. W.J. Jie, Dr. Z.B. Yang, Dr. G.X. Bai, Prof. J.H. Hao
Department of Applied Physics, The Hong Kong Polytechnic University, Hung Hom, Hong Kong, P.R. China
E-mail: jh.hao@polyu.edu.hk
Dr. W.J. Jie
College of Chemistry and Materials Science, Sichuan Normal University, Chengdu 610068, P.R. China

Keywords: two-dimensional materials, photoluminescence, electroluminescence, nonlinear optics, van der Waals heterostructures

Due to the isolation and fabrication of a rapidly increasing number of two-dimensional (2D) materials, extensive attention has been drawn to investigate 2D materials for scientific and technological studies as well as potential applications. In recent years, a series of significant and fascinating properties are found and further modified in graphene and graphene-like 2D layered materials. Among them, luminescence is one of the important investigation aspects, which is relevant to the unique structural, carrier transport, photonic and optoelectronic properties of 2D materials. Herein, we provide a general overview of recent advances of luminescence in 2D systems, including 2D materials and van der Waals heterostructures. This review article provides an insight into the mechanism of luminescence and the luminescent characterizations and performance as well as the methods employed to modulate the luminescence behaviors of 2D systems. A number of recent works are introduced to specifically describe the new developments of photoluminescence, electroluminescence and nonlinear optics in 2D materials. We then discuss the applications of luminescence in 2D systems in terms of optoelectronics and biological fields. By summarizing the importance of luminescence in 2D materials and van der Waals

heterostructures, the challenges and opportunities for future investigation and applications are highlighted.

1. Introduction

Luminescence is the form of light emission as a consequence of a substance excited by external energy, which has been extensively studied in various material systems due to its scientific and technological importance and practical applications.[1-3] In addition to conventional luminescent materials, such as metal-ion-doped phosphors, semiconductors, organic phosphors, etc,[4-6] luminescence has further been investigated in recently emerged two-dimensional (2D) materials ever since the first discovery of graphene through the method of mechanical exfoliation by Geim's group in 2004.[7-9] Although pristine graphene could not offer luminescence due to the absence of bandgap,[10,11] it is possible to open a suitable bandgap via applying an external electric field or reducing graphene into ribbons/quantum dots or chemical/physical treatments.[10,12,13] Graphene oxide (GO) is a graphene sheet modified with oxygen functional groups, exhibiting broadband steady-state photoluminescence (PL) in wavelengths from ultraviolet (UV) to near-infrared (NIR).[14,15] Beyond graphene, a large variety of 2D materials can be exfoliated from some layered materials with the stacked structure in their bulk materials like graphite.[16,17] A big category in 2D family is transition metal dichalcogenides (TMDs), consisting of hexagonal layers of transition metal atoms sandwiched between two layers of chalcogen atoms (typically S, Se, or Te), like MoS_2, WS_2, etc.[18,19] Moreover, monolayer black phosphorene (BP), named phosphorene, has drawn much attention after it was firstly isolated by mechanical exfoliation method in 2014. 2D BP layers possess amazing physical properties, including an intrinsic and widely tunable direct bandgap from 0.3 eV (bulk) up to ~2.0 eV (monolayer).[20-23] Another widely studied 2D material is hexagonal boron nitride (*h*-BN), which is the layered insulator with wide bandgap.[24,25] **Table 1** shows the widely tunable bandgap energies of 2D materials from semimetal graphene, semiconducting 2D BP with a non-vanishing direct bandgap[20,21]

and 2D InSe with a widely tunable bandgap[26,27] as well as 2D TMDs with indirect-to-direct bandgap transition in monolayer[28] to insulating *h*-BN[24]. The big 2D family with broad tunable bandgaps shows diverse luminescence properties. Furthermore, the luminescent properties can be tuned by external conditions, including temperature, substrate, strain, magnetic field, chemical and electrical doping. Therefore, investigating luminescence and subsequently enhancing or modulating the luminescence in 2D materials is significant for researchers to understand and further modify the materials. Besides, luminescence in 2D materials also possesses important applications in light emitting diodes (LEDs)[29,30] and lasers[31-33] as well as applications in biomedicine of biomolecules detection and bioimaging and so on.[34,35]

Although there are many reviews providing a general overview of different aspects of graphene and graphene-like 2D materials, a specialized review focused on the luminescence behaviors of 2D materials is still in lack and a unified profile of luminescence in 2D system is much needed to provide. In this article, we will review the development in luminescence of 2D systems, including graphene and graphene-derived materials, other 2D layered materials beyond graphene as well as van der Waals (vdW) heterostructures (HSs) based on 2D materials (**Figure 1**). In order to describe the involved knowledge and science more fully, we will firstly discuss the physical mechanisms of luminescence, followed by the related electrical and optical properties of 2D materials as a function of layer numbers, as well as the characterizations, performance, and the applications of luminescence. Considering PL and electroluminescence (EL) are two major classes of luminescence in 2D materials, we will put our focus on PL and EL in this review article, from physical principles to luminescent behaviors of 2D materials and homo- and heterostructures and their practical applications. To be more specific, PL in graphene and its derivatives, TMDs and other 2D materials as well as PL in doped 2D materials and 2D vertical and lateral HSs are systematically discussed. Additionally, we will summarize EL in 2D materials, 2D homo- and heterojunctions. Besides,

nonlinear optics including two-photon luminescence (TPL), second-harmonic generation (SHG) and third-harmonic generation (THG) in 2D materials will be introduced in this review. At last, a brief summary and perspective around luminescence in 2D materials will be emphasized.

2. Mechanism of luminescence

In traditional bulk materials, luminescence is the emission of photon by a substance named a luminescent material or phosphor, when excited by some kinds of external energy. The luminescence can be stimulated by electromagnetic radiation, electron beams, electric field, chemical reactions, which ultimately lead to light emission. Simultaneously, the absorbed energy can be released in the form of photon and/or phonon. Therefore, the luminescence is actually the energy transformation of external stimulation into light emission during the process of electron transferring from excited state to ground state. Inside the luminescent materials such as semiconductors, the luminescence originates from the radiative recombination of excitons, and Coulomb-bound electron-hole pair states. The wavelength emitted is dependent on the electronic band structure. In the materials containing activators, the luminescence is generated from radiative transition between energy levels of the active centers, such as lanthanide and transition metal ions. The luminescence property is dependent on the activator ions themselves and the surrounding crystal structure. According to the excitation sources, there are several types of luminescence, namely PL, EL, mechanoluminescence (ML), cathodoluminescence (CL), thermoluminescence (TL), and so on.[36-38] Among them, PL and EL are the two major and widely studied types due to their high efficiency and broad applications in real devices. PL is the light emission from luminescent materials when the excitation and absorption of photons (electromagnetic radiation) are occurred. The time period between absorption and emission may range from femtoseconds up to milliseconds, even span to minutes or hours in the persistent luminescence. The PL properties are heavily dependent on the electronic band structure, or

the luminescent centers. EL is the consequence of radiative recombination of electrons and holes in a luminescent material, usually semiconductor. In advance of radiative recombination, doping the material to fabricate a p-n junction may lead to separated electrons and holes, or a strong electric field accelerates high-energy electrons. As a result, the material generates photon in response to the flow of an electric current or to a strong electric field.

On the other hand, luminescence not only depends on the external energy but also the carrier transport and optical properties of the luminescent materials. Recent advances in the fabrication of 2D layered materials down to monolayer have enabled explorations in a new low-dimensional platform. Taking prototypical TMD MoS_2 as an example, it is composed of covalently bonded S-Mo-S layers which are stacked by weak vdW forces. Bulk MoS_2 is a semiconductor with an indirect bandgap of about 1.30 eV. The bandgap of MoS_2 shifts from the indirect gap to direct gap of about 1.90 eV when decreasing the thickness of MoS_2 from bulk to single layer due to the quantum confinement effects on the electronic structure of MoS_2.[19] From bulk to monolayer, the suitable bandgap enables exploring photovoltaic and photocatalytic applications due to their strong absorption in solar spectrum region. However, the luminescent principles are varied in 2D forms due to the different electrical and optical properties from the bulk materials. In 2D materials, strong light-exciton interactions can be observed. The exciton binding energies in monolayer TMD materials is much larger than that in their bulk crystals owing to the enhanced Coulomb interactions caused by the reduced dimensionality.[39,40] Thus, an exciton-dominated optical response can be observed in 2D semiconductors. An exciton describes a two-particle excitation with simultaneous creation of both an electron and a hole. Monolayer semiconductors have several series of excitons with strong binding energy, stemming from different regions of the Brillouin zone. The split valence bands at *K* points can induce two direct interband optical transitions, namely the A and B excitonic states. The bulk TMD crystals also have the excitonic states, with binding energies in the range of 50 meV to 80 meV, due to the layered structure formed by the weak

vdW force and the heavy effective mass of valence/conduction bands. In contrast, the exciton binding energies of monolayer crystals are dramatically increased compared to their bulk materials with the value in excess of 0.6 eV, which is a significant fraction of the corresponding bandgap. The binding energy of exciton is extracted by the energy difference between the optical gap and the band-to-band transition energy. Besides, trions are complexes consisting of three charged particles.[41] To be more specific, a negative trion is composed of two electrons and one hole, while a positive one is composed of one electron and two holes. The trion is a quasi-particle, similar to the traditional exciton which consists of one electron and one hole. The binding energies of the trions in monolayer TMDs are also much larger than that in conventional bulk semiconductors, which makes the trion state easily visible in PL.[42] Furthermore, both the electronic bandgap and exciton binding energies can change substantially, depending on the external conditions, including the environment temperature,[43,44] chemical doping,[45,46] supporting substrates,[47-49] and so on. On top of the excitonic dominated luminescence, emission caused by defects,[50] two-photon absorption and non-linear optical properties have already been studied in 2D materials.[51,52] As a consequence, 2D materials exhibit versatile behaviors in luminescence. In the following three sections, we highlight some intriguing progress in luminescence, especially PL, EL and TPL in 2D materials as well as heterojunction and homojunction based on 2D materials.

3. PL in 2D Materials and vdW HSs

3.1 PL in graphene and its derivatives

Graphene is a single-atom-thick sheet of hexagonally arranged, sp^2-bonded carbon atoms.[53] Graphene possesses some outstanding properties, such as high mobility, optical transparency, flexibility, robustness and environmental stability,[54-56] making graphene to be one of the most promising materials for future applications in nanoelectronics.[57,58] So far, the main focuses of graphene have been put on fundamental physics and electronic devices.[59-62] In the band structure of graphene, the valence and conduction bands are cone-shaped and

meet at the *K* points of the Brillouin zone, giving rise to zero bandgap.[10,11] In spite of the absence of bandgap, graphene has been widely studied to achieve a tunable bandgap for the PL behaviors.[10,12,13] All these methods involve the generation or exploitation of defects. Actually, the generated defects in graphene and its derivatives play a critical role in generation of both a suitable bandgap and light emissions. GO is a chemically tailored graphene sheet covalently connected with some independent fluorophores, i.e., some functional groups of oxygen like epoxy, hydroxyl and carboxyl.[63] These fluorophores are aromatic n-conjugated sp^2-hybridized subsystems of carbon atoms surrounded by sp^3 regions. The PL of GO is pH dependent because of the presence of many oxygen containing groups in GO sheets. Reduced GO (rGO) is formed through reduction of GO.[64] The PL behaviors of rGO are somewhat different from GO because the reduced oxygen containing groups during the reduction process. Therefore, GO and rGO can emit versatile PL properties which can be tuned over a broad spectral range. Their diverse PL characteristics have been systematically studied.[65-68] Generally, the luminescent samples are GO/rGO solutions or solids.[69,70] In this subsection, the diverse PL characteristics, origin and potential applications for graphene layers and nanoribbons (GNRs) are reviewed.

3.1.1 PL in GNRs.

There are several ways to modify the electronic band structure of graphene in order to achieve a suitable bandgap. One of them is by cutting graphene into nanoribbons. Since the discovery of graphene, one-dimensional (1D) GNRs have been widely studied due to their substantial electronic bandgap and versatile optical properties which are fundamentally different from their pioneer graphene. The first-principles calculations suggest that it is possible to achieve a suitable bandgap via reducing graphene into GNRs, whose bandgap can be well controlled by their width and edge structures.[71-73] Actually, the bandgap is generally negligible in zigzag edged GNRs which possess a magnetic localized edge state. On the other hand, a tunable bandgap can be achieved in armchair GNRs without the magnetic localized

edge state.[74] The experimental demonstration shows that the bandgaps in lithographically patterned GNRs can be tuned through controlling the ribbon width during the fabrication process.[75-77] A bandgap with value as high as 200 meV was reported in such lithographically patterned GNRs with width as narrow as 15 nm. Furthermore, an expected bandgap can be achieved in GNRs by keeping the width narrow (below 10 nm) and maintaining the edge atomically smooth. In the carbon family, GNRs have recently been recognized as promising building blocks for future electronic, optoelectronic and spintronic devices since many methods have been proposed for their preparation.[78-81] However, it is difficult to obtain smooth edges and reduce the width below 10 nm by lithographical patterning method. Some chemical approaches have been proposed for the fabrication of GNRs. In 2008, Dai's group reported a chemical route to produce solution-phase-derived GNRs with ultra-narrow widths (<10 nm) and well-defined zigzag or armchair-edge structures.[79] The prepared GNRs are stably suspended in solvents with noncovalent polymer functionalization. The thickness of the GNRs was mostly between monolayer and trilayer. The proposed chemical method can achieve GNRs with tunable widths and expected electronic properties for fundamental and practical applications.[82,83] Then, a simple solution-based oxidative method was proposed to prepare GNRs by lengthwise cutting of multiwalled carbon nanotube (MWCNT) side walls.[84] Similarly, GNRs were achieved by unzipping MWCNT by plasma etching.[85] The prepared GNRs have smooth edges and a relatively narrow distribution width in the range of 10-20 nm. This provides us a method for producing accessible unzipping-derived GNRs with large scale. In 2010, Cai et al. reported a simple method for atomically precise GNRs by using surface-assisted coupling of molecular precursors on Au (111) and Ag (111) substrates.[86] The precursor monomers were well designed to control the topology, width and edge of the prepared GNRs. Such proposed bottom-up approach can atomically control the fabrication of GNRs, which provide a way to widely study the electronic, optoelectronic and spintronic properties of GNRs with well defined structures.[87-90]

The electronic bandgap of GNRs formed by the above methods suggests the possibility of observing PL in GNRs. However, unlike their electronic properties, optical properties of GNRs have not been widely studied. Optical absorption shows the strong dependence on the width of GNRs and the wavelength of the visible light.[91] PL has been seldom reported from substrate-supported GNRs since the metallic substrates typically quench the PL. Some structurally well-defined GNRs with functional chains show versatile PL properties.[92,93] Until very recently, it is reported that PL can be achieved in GNRs on insulating substrate by using focused light illumination.[94] The armchair GNRs with N = 7 carbon atoms width (7-AGNRs) are grown on Au and then transferred onto insulating substrates of SiO_2/Si and quartz wafers for experiments. It was reported that the focused light with wavelengths shorter than 510 nm could efficiently generate defects for the fabricated GNRs. Once defects were generated by initial exposure, PL could be enhanced due to the contribution from the generated defects. As shown in **Figure 2a**, a weak emission from the GNR sample was observed when excited with focused 440 nm wavelength light. The PL peak was located at about 1.8 eV when the GNR sample was continuously exposed to 440 nm radiation. The initial weak emission could be caused by the defects generated either during sample growth, transfer, or storage. The subsequent enhanced emission is ascribed to the generation of defects in GNRs through a photochemical reaction during the focused light exposure. The defects were generated by the reaction between fabricated GNRs and O_2 and/or H_2O in air as well as with the underlying SiO_2 which could generate several types of sp^3 defects and edge defects. The emission could be suppressed if the exposure was performed under high-vacuum conditions. For the excited light with wavelengths longer than 510 nm, the PL was negligible independent of the photon energy. Furthermore, the emission strongly depended on the polarization direction. When the polarizer and analyzer polarization directions were both along with the ribbon axis, the emission could achieve maximum, as schematically shown by the red vertical arrow in Figure 2b. On the other hand, when the polarization direction was

both perpendicular to the ribbon axis, as shown by the blue horizontal arrow in Figure 2b, the emission showed the minimum value. The detected significant polarization anisotropy could definitively prove the observed emission originated from the fabricated GNRs.

In addition to the aforementioned blue laser illumination in ambient conditions, bright PL can be achieved by hydrogenation in an ultrahigh vacuum (UHV) environment due to the generation of sp^3 defects formed by C-H bonds. The hydrogenation and PL measurements were performed in a homemade UHV PL system. Figure 2c shows the weak intrinsic PL spectra measured in UHV before hydrogenation with laser light (532 nm) polarized parallel and perpendicular to the GNR axis, respectively. The strong Raman modes and their higher orders are clearly shown in the spectra. Then the GNRs are exposed to a beam of atomic hydrogen to generate defects of C-H bond. After 10 min exposure, the polarized PL is enhanced and peaked at about 1.8 eV, as shown in Figure 2d. Furthermore, it was found that 40 min exposure could achieve the most chemisorbed H atoms. However, the PL was weakened for 40 min exposure compared to that for 10 min exposure. This was attributed to the decreased efficiency of the incident light absorption when many sp^2 bonds were broken. In their report, two ways of blue laser illumination in ambient and hydrogenation in UHV conditions were employed to enhance the pristine PL of GNRs with light emission at about 1.8 eV. The enhanced PL spectra and the peak positions for both methods to defect generation were very similar to each other since the electronic structures of sp^3 defects were almost same. This work not only demonstrated the optical properties of GNRs on insulating substrates, but also provided a template for precise functionalization by luminescent molecules as well as for further exploration of GNRs on in device geometries.

3.1.2 PL in graphene by chemical treatment.

There are several methods to modify the electronic band structure of graphene in order to achieve a suitable bandgap. One is by chemical or physical treatments. Hydrogen plasma is employed to reversibly modulate the electronic properties of individual graphene flakes,

turning them into insulators.[13] However, no luminescence was observed in the hydrogen plasma treated graphene flakes. It was reported that broad PL from 400 to 800 nm was achieved in monolayer mechanically exfoliated graphene using an oxygen plasma treatment.[50] In experimental, the exfoliated graphene was exposed to oxygen/argon (1:2) ratio frequency plasma. For a short time (3 s) exposure to oxygen plasma, the graphene sample showed spatially resolved PL, as shown in **Figure 3a** of the confocal PL image. When the treatment time was increased (5 s), the strong and spatially homogeneous PL behaviors were observed, as shown in Figure 3b. The PL exhibited broadband spectra with the peak centered at about 700 nm, as shown in Figure 3c. The PL transients were described by a triple-exponential with decay times, as shown in Figure 3d. The authors claimed that the observed PL could result from the CO-related localized electronic states formed at the oxidation sites. The broadband PL band was caused by a superposition of overlapping bands with narrow PL band centered at different energies controlled by their sizes. It should be mentioned that PL only can be detected in monolayer graphene after the plasma treatment. For multilayer graphene, only the topmost layer was etched, inducing the absence of PL. Similar behaviors have been reported by several other groups.[95,96] Oxygen plasma can be used to selectively convert the top-most layer when multilayer samples are treated. It was proposed that a suitable bandgap as well as the corresponding PL was achieved in monolayer graphene through oxygen treatment, while bilayer graphene maintains its semi-metallic behavior without the noticeable emission. The PL is spatially uniform across the flakes and connected to elastic scattering spectra distinctly, differing from that of gapless pristine graphene.

3.2 PL in TMDs

Since the discovery of single atomic layer carbon, a series of materials have attracted a huge interest due to their layered structure which makes them can be exfoliated from their bulk materials to form free-standing 2D atomic crystals.[16] Among them, TMDs are the

semiconducting alternatives to semimetal graphene. TMDs are formed by strong in-plane covalent bonding and weak out-of-plane vdW interactions and accordingly can be exfoliated into 2D crystals with mono- or few-layer thickness. 2D layered TMDs have been widely studied within the last few years because of their fascinating physical and optical properties as well as their promising applications in the fields of electronics, optoelectronics, photonics, spintronics and so on.[97,98] Bulk TMDs are semiconductors with indirect bandgaps, which could be converted into direct bandgaps by thinning them down to monolayer forms due to the geometrical confinement effect.[99] Thus monolayer TMDs are very attractive and also accessible to optical investigations such as PL measurements because of the existence of the direct bandgap. Besides, in their monolayer form, the crystal inversion symmetry is broken, hence spin and valley are capable of coupling to each other. Therefore, the monolayer TMDs possess unique electrical and optical properties different form their bulk crystals and accordingly they have the potential to be used in future electronic and optoelectronic applications. However, their room-temperature PL quantum yield (QY), which is the primary figure of merit, is extremely low even for monolayer TMDs. Many efforts have been put on the luminescent properties of TMDs and subsequently focus on enhancing or modulating the luminescence in TMDs. It was reported that the QY for monolayer TMDs was in the range of 0.01-6% for monolayer TMDs.[100] The low QY could be attributed to the defect states in TMDs which could give rise to non-radiative recombination and accordingly decrease the PL QY.[101] This also becomes one of the main constraints for TMDs. Consequently, a number of works have been done to improve the efficiency of PL for 2D TMD crystals.[102-104] Besides, PL in TMDs can be the affected by external conditions, such as temperature, substrate, strain, magnetic field, and so on. In this subsection, we focus on PL in TMDs. The PL characteristics, origins, methods employed to enhance their PL, and effects of external conditions are reviewed.

3.2.1 PL in MoS_2

MoS_2 is one of the most popular representative TMDs. Its prototype FETs demonstrate high electron mobility and high on/off ratio of nearly 10^8. The lattice structure of MoS_2 is shown in **Figure 4a**.[28] There are two hexagonal planes of S atoms and an intermediate hexagonal plane of Mo atoms in the sequence of S-Mo-S in one MoS_2 unit layer. The bulk MoS_2 crystal is formed by vdW bonded unit layer, which includes covalently boned Mo and S atoms. It is feasible to obtain ultra thin MoS_2 layers due to the relatively weak vdW interlayer interactions and the strong ionic-covalent intralayer interactions. There are three phases for MoS_2 crystal, namely 2H, 3R and 1T according to the stacking orders. Among them, 2H can be well exfoliated and subsequently is widely studied in laboratory. In the 2H stacking, the S atoms are located directly above and below the Mo atoms in the neighboring layer. The lattice constant is 0.316 nm and interlayer distance is about 0.65 nm. The simplified band structure of MoS_2 is shown in Figure 4b.[19] The bulk sample is indirect semiconductor with the indirect band energy of 1.29 eV. The band energy shifts to direct bandgap of about 1.90 eV when decreasing MoS_2 thickness to monolayer. Thus the PL behaviors in monolayer as well as several-layered MoS_2 are very attractive due to their tunable bandgap. Their electrical and optical properties have been widely studied.[105-107] In 2010, Heinz's group systematically studied the evolution of the electronic structure and optical properties of mechanically exfoliated ultrathin MoS_2 crystals as a function of layer number.[19] The PL behaviors of suspended monolayer and bilayer MoS_2 under identical excitation at 2.33 eV are shown in Figure 4c. A strong PL peak centered at about 1.9 eV with narrow feature of 50 meV width was found for monolayer MoS_2. On the other hand, the PL decreased dramatically when the thickness increased to bilayer and the PL became negligible in bulk MoS_2 due to its indirect bandgap. The PL efficiency can be well described by QY which is the ratio of the emitted photon number to the absorbed photon number. As shown in the inset of Figure 4c, the PL QY had a dramatic enhancement when the thickness decreasing to monolayer, suggesting the enhanced PL efficiency in the monolayer sample. Furthermore, PL spectra of few-layer

samples showed multiple emission peaks, one of them (named peak A) coincided with the monolayer emission peak (1.9 eV), as shown in Figure 4d. Peak A shifted to the red slightly and became broadened with increasing the layer number. Peak B located at about 150 meV above peak A. Besides, the broad peak I located at lowest energy in each spectrum. This peak had a red shift and became extremely weak with increasing the layer number. The optical absorption measurements suggested that PL peak A at 1.90 eV for monolayer sample matched well the lower absorption resonance in both position and width. Therefore, the PL of monolayer MoS_2 resulted from direct gap luminescence. The observed PL peaks A and B in bilayer and several-layer sample corresponded to the direct gap transitions located at the *K* point of the Brillouin zone from the lowest conduction band *c*1 to the highest split valence bands *v*1 and *v*2, respectively. The PL peak I at 1.59 eV was attributed to indirect gap luminescence and this peak finally became to 1.3 eV for bulk MoS_2.

3.2.2 PL in other TMDs

TMDs consist of a series of 2D layered materials recently studied, such as WS_2, WSe_2 and $MoSe_2$. To be more specific, TMDs are MX_2, where M is Mo, W ₋ and X is S, Se, or Te.[108-111] Recent advances in nanoscale science and technology have opened up new opportunities for 2D layered TMDs characterization and device fabrication. TMDs possess similar crystal structure and also physical and chemical properties to MoS_2. Due to the geometrical confinement effect, monolayer and several-layer TMDs exhibit amazing electrical, optical and optoelectronic properties different from their bulk materials. Like MoS_2, significant evolution emerges in the electronic band structure with a sizable bandgap when TMDs are exfoliated from bulk to 2D layers. The most amazing behavior of TMDs is the transition to direct bandgap in their monolayer crystal from indirect bandgap in bulk, offering the possibilities of device applications, such as photodetectors, phototransistors and luminescent devices. The direct bandgap for monolayer TMDs is in the range of 1 to 2 eV, which is significant for the electronic and optoelectronic applications.[112] Similarly, thanks to the direct bandgap in

monolayer, PL can be detected in monolayer TMDs, suggesting the potential applications in emission devices. Among them, WS_2 has been known to possess the highest PL efficiency among all 2D TMCs.[47,113] However, to enable their application in PL devices, numerous challenges are needed to be overcome, especially improving the efficiency of PL and understanding the mechanism of exciton based recombination.

Next, the electric and PL properties of 2D TMDs will be illustrated by examples of tungsten-based dichalcogenides WS_2 and WSe_2. Similar to MoS_2, the typical FETs based on 2D layered WS_2 or WSe_2 were reported to show high carrier mobility.[114,115] The lattice constant of the tungsten-based dichalcogenide WS_2 (WSe_2) is a = 3.15 Å (3.28 Å) and c = 1.298 nm (1.298 nm), while the interlayer distance for WS_2 and WSe_2 are about 0.7 nm. In WS_2 structure, W atoms is bonded to two S layers by strong covalent bonds in the hexagonal plane, and each 2D WS_2 layer is connected to adjacent layers by a weak vdW interaction. Similarly, WSe_2 is formed by covalently bonded Se-W-Se layers stacked by a weak vdW force. WS_2 and WSe_2 crystals are indirect gap semiconductors in their bulk form with trigonal prismatic structure.[112] For WS_2, its bulk indirect bandgap of about 1.35 eV shifts to direct bandgap of about 1.90 eV in monolayer form. The bulk indirect bandgap of WSe_2 exhibits similar transition from 1.2 eV to monolayer 1.7 eV.[116,117] Now we focus on the PL properties of the tungsten-based dichalcogenides. The normalized PL spectra for mono- to few-layer 2H WS_2 and 2H WSe_2 are shown in Figure 4e and f, respectively.[100] Here the 2H stacked 2D tungsten-based dichalcogenides flakes were prepared by mechanically exfoliating the 2H crystals synthesized by the chemical vapor transport (CVT) method. Peak A centered at 630 and 750 nm is the direct bandgap emission emerging in monolayer WS_2 and WSe_2, respectively. Peak I is an indirect gap emission exiting in the 2D tungsten-based dichalcogenides except monolayer samples. Besides, peaks A' and B, shown as dashed lines, are magnified for clarity. They are resulted from hot electrons and typically 100 to 1000 times weaker than the bandgap emission peaks. PL spectra for both tungsten-based dichalcogenides

show remarkable dependence on their thickness. It is noticeable that there is a sudden increase in PL intensity when both mechanically exfoliated samples are thinned to a monolayer. Both monolayer tungsten-based dichalcogenides demonstrate strong emission at the energy corresponding to direct bandgap A excitonic absorption, whereas the direct emission intensity is dramatically reduced for few-layer flakes, suggesting the indirect-to-direct gap transition when thinned to a single monolayer. And the emission intensity becomes weak with increasing number of layers, corresponding to the sizable bandgap in the 2D layered tungsten-based dichalcogenides similar to MoS_2.

It should be noted that Figure 4g and h show the relative QY for 2D flakes of tungsten-based dichalcogenides. In contrast to the CVT-grown crystal, the PL properties of commercial natural 2H-MoS_2 were also studied in this experiment. The PL intensity of monolayer tungsten-based dichalcogenides is about 20 to 40 times higher than that of monolayer MoS_2 sample exfoliated from the commercial natural crystal. Even the PL of bilayer WSe_2 is also more efficient than that of monolayer MoS_2. The relatively improved PL QY was attributed to the unintentional doping in the tungsten-based dichalcogenides flakes. Furthermore, the observation of biexciton states in monolayer WSe_2 was recently reported by the discovery of a new emission peak.[118] The biexciton is four-body quasiparticle, consisting of two distinct excitons. The biexciton exhibits large binding energy (52 meV), resulting from strong carrier confinement and reduced non-local dielectric screening.

3.2.3 Methods to improve the PL QY in TMDs

As aforementioned, the PL QY for monolayer TMDs is still extremely low in most of reports, generally less than 1%.[100] Thus, various strategies have been tried to improve the efficiency of PL.[119,120] It is feasible to modulate the optical properties of 2D TMDs by electrical doping.[121] In 2012, Mak et al. reported the gate voltage dependent optical properties of monolayer MoS_2.[40] By modulation of excitons and trions through the applied gate voltage, the PL and absorption of monolayer MoS_2 can be tuned, as shown in **Figure 5a**.

A trion is a quasiparticle, composed of three charged particles.[41] In monolayer MoS_2, the negative trion consisting of two electrons and a hole were optically created with valley and spin polarized holes. Indeed, both negative trion (A^-) and exciton (A) features were identified by optical absorption and emission spectra in a monolayer MoS_2 based FET by applying a tunable gate voltage from -100 to 80 V, corresponding to a doping density of about 10^{13} cm^{-2}. As shown in Figure 5a, the optical absorption was overall suppressed with increasing electron doping. The absorbance of exciton diminished rapidly and finally disappeared into the background for positive gate voltages. In contrast, trion absorption broadened gradually without changing its intensity. Similar to its absorption, the PL intensity of the exciton can be switched off by biasing of positive voltages. On the other hand, both exciton and trion resonances can be identified in PL and absorption spectra for negative gate voltages. In addition, the trion feature peak showed a slight red shift, which could be attributed to the doping-dependent Stokes shift. The gate voltage (carrier density) dependent PL and source-drain current are shown in Figure 5b. The intensity of trion PL remained almost unchanged regardless of the applying positive or negative gate voltages. Whereas, the PL of exciton is gate dependent, and more importantly, its intensity is enhanced by nearly two orders of magnitude. Thus, for negative gate voltage, the optical response, including absorption and PL, was dominated by excitons. For positive gate voltage, the excitons were suppressed and trions played the dominate role in optical response for monolayer MoS_2. Furthermore, not only the PL intensity, but also the PL peak position was changed by the gate voltages, especially when positive gate voltages were applied (when trion was dominated in the resonance of PL).

Moreover, chemical doping is a feasible way to modulate the carrier density of MoS_2. It was reported that the PL properties of monolayer MoS_2 could be well tuned by solution-based chemical doping.[106] To be more specific, the PL intensity could be dramatically enhanced by adsorption of p-type dopants (2,3,5,6-tetrafluoro-7,7,8,8-tetracyanoquinodimethane (F4TCNQ) and 7,7,8,8-tetracyanoquinodimethane (TCNQ)). This enhancement was explained by the

increased recombination of excitons induced by high doped electrons compared to pristine dominant recombination of negative trions. In contrast, the PL intensity could be reduced by the adsorption of n-type dopants (nicotinamide adenine dinucleotide (NADH)). This phenomenon was understood by the suppression of exciton PL due to the injection of excess doped electrons. Thus, the PL behaviors in monolayer MoS_2 can be controlled (enhanced or weakened) through extraction or injection of carriers by the solution-based chemical doping method. In 2015, a near-unity emission QY was reported in monolayer MoS_2 by Javey's group and their partners.[122] In their experiments, an air-stable, solution-based chemical doping was found to eliminate the contribution of defect induced nonradiative recombination by uniformly passivating and/or repairing monolayer MoS_2 samples via using organic superacid of bis(trifluoromethane) sulfonimide (TFSI). The treatment could remove defects induced nonradiative recombination, giving rising to a satisfactory QY of more than 95% with a long lifetime of about 10 ns. **Figure 6a** shows the PL spectra of a monolayer MoS_2 before and after the superacid treatment measured under identical illumination conditions. The modification induced the 190-fold increase in the PL intensity without changes in the emission peak shape, as shown in the inset of Figure 6a. The PL images before and after the superacid treatment are shown in Figure 6b and c, respectively. Insets show the corresponding optical images. The uniform increase of PL in the overall MoS_2 sample was be achieved, yielding the near-unity PL QY. More importantly, the enhancement in optical response could not induce the degradation in the transport or surface morphology by the superacid modification. Furthermore, time-resolved measurements suggested the original MoS_2 monolayer had extremely short PL lifetime on the order of 100 ps. After treatment, a substantial increase about 10 ns was found for the monolayer MoS_2 sample. Such chemically doped MoS_2 monolayers with near-perfect electronic and optoelectronic properties show potential for applications in highly efficient LEDs, solar cells and other optoelectronic devices.

Then, many efforts have been done to achieve near-unity QY in monolayer MoS_2 by other chemical doping methods.[45,46] By considering the TFSI treated monolayer samples whose surface are not stable in the typical semiconductor processing conditions, such as water and solvents, an encapsulation approach was proposed to improve the post-processing stability and also keep near near-unity QY for the monolayer MoS_2 samples.[45] It was reported that the monolayer samples were encapsulated by an amorphous fluoropolymer before TFSI treatment. The subsequent doped TFSI molecules could diffuse through the encapsulation layer and modify the surface defect states. This work provides us a feasible route to achieve high-stable monolayer sample for future fabrication of highly efficient optoelectronic devices.

Furthermore, many efforts have been put on to improve the PL efficiency of other TMDs. It was reported that chemical doping of F_4TCNQ and H_2O molecules could improve the electrical and emission properties of monolayer WS_2.[123] However, it should be noticed that the tunability of emission via the molecular adsorption is different for n- and p-typed 2D TMDs. For example, a broad-range modulation of emission has been reported in TMDs of both MoS_2, $MoSe_2$ and WSe_2 by the physical adsorption of O_2 and/or H_2O molecules.[124] The physical adsorption of molecules provides carrier doping on the 2D TMDs and serves as the role similar traditional electric field gating. Actually the reversible molecular gating provides orders of magnitude broader control of carrier density and gives rise to light emission over 100 times modulation of light emission efficiency of the 2D TMDs. For n-typed MoS_2 and $MoSe_2$, the physisorption of O_2 and/or H_2O molecules can deplete the electrons and lead to the drastic enhancement in PL. Whereas, for p-type WSe_2, the molecular physisorption induces the degradation of PL. The charge transfer depletes electrons in n-type MoS_2 and $MoSe_2$ and stabilizes excitons, activating a radiative recombination channel. As a consequence, a remarkable enhancement can be achieved in the PL for n-type monolayers. In contrast, the O_2 and H_2O molecules accumulate the majority holes in p-type WSe_2, resulting in strong suppression of the PL. Besides, the PL intensity can be remarkably enhanced in

monolayer $MoSe_2$ prepared by CVD method through hydrohalic acid treatment.[102] The overall PL intensity can be improved by a factor of 30. In fact, the HBr treatment not only enhances the PL intensity but also repairs the structural defects in monolayer CVD-grown $MoSe_2$ sample. After the HBr treatment, not only PL intensity is dramatically improved for more than 30 times, but also the emission energy demonstrates blue shifts at the centre of the CVD-grown monolayer triangle $MoSe_2$ sample. Several possible factors have been proposed to address the improvements in PL, including the repairing in the structural defects, external electrostatic doping, and the modification of chemical composition. Actually, in addition to HBr, hydrohalic acids of HCl and HI were also used to treat the sample. Similar enhancements were observed in the triangle sample after HCl and HI treatment. Among the three hydrohalic acids, HBr demonstrated the best PL performance.

As aforementioned PL improvement in MoS_2 by superacid (TFSI) treatment, the QY is improved from less than 1% to more than 95%.[122] The method has also been used to treat the TMDs monolayers of WS_2, MoS_2, WSe_2, and $MoSe_2$, whereas sulfur and selenium based TMDs show different response.[46] As shown in Figure 6d and e, PL improvements are clearly observed in sulfur based TMDs of WS_2, while PL degradation is found in selenium based TMDs of WSe_2. $MoSe_2$ monolayer shows similar behaviors to WSe_2 sample. The inset of each figure shows the corresponding normalized spectra for the exfoliated and TFSI treated samples, indicating that the treatment cannot induce any shifts in the direct bandgap exciton emission and/or significant changes in peak shape. It was proposed that the TFSI treatment could repair or passivate the sulfur based 2D materials. In contrast, this method is ineffective to selenium based TMDs and thus high QY cannot be obtained. 2D TMDs have a variety of defect types in naturally or synthesized monolayer samples. In sulfur vacancies dominant WS_2 and MoS_2 monolayer samples, near-unity QY can be achieved by TFSI doping. On the other hand, there is a small drop in PL intensity by the TFSI treatment in both WSe_2 and $MoSe_2$. In WSe_2 monolayers, defects are complexes consisting of chalcogen vacancies and metal atoms

rather than simple vacancy sites. High resolution scanning tunnel microscopy (STM) showed that selenide surfaces are dominated by hillock-like structures induced by donor impurities, while sulfide surfaces are dominated by structural defects and acceptor impurities. Thus, sulfur based TMDs can be passivated and the QY can be remarkably improved by TFSI treatment, while the treatment is ineffective to selenium based TMDs and consequently no PL improvements can be detected.

3.2.4 Effects of external conditions on PL in TMDs

In addition to electrical and chemical doping, PL in TMDs can be the tuned by external conditions like temperature, magnetic field, substrate, strain, and so on. Firstly, temperature is an important factor to measure PL and can change the observed exciton states in the forms of emission shape, peak energy and relative weight of exciton and trion.[43] For monolayer $MoSe_2$, trion binding energy of 30 meV can be clearly observed at low temperature. As the temperature increases, one may observe that the negatively charged trion drops significantly, which can be caused by the electrons escaping their bound trion state because of the thermal fluctuations. Both the neutral and negatively charged excitons show a blue shift for decreasing temperature according to the standard semiconductor bandgap dependence. The increase of photon energy at low temperature is caused by thermal increase of the $MoSe_2$ bandgap.[44] Under external magnetic field, valley Zeeman effect was reported in monolayer TMDs.[125,126] The PL properties of monolayer TMDs can be well controlled by the direction and magnitude.[127] The polarized PL emissions of neutral and charged excitons are studied under external magnetic field. Both emission energies shift monotonically with magnetic field. The shift direction is reversed for photons of opposite circular polarization due to emitted photons with reversed polarization states correspond to optical transitions from the different valleys, suggesting valley splitting has been produced. Even at high carrier doping by electric gating, Zeeman effect can be achieved in monolayer $MoSe_2$ where only trion emission is visible while the neutral exciton peak is very weak.[125] A linear Zeeman shift for the trion exhibits

opposite behavior in the two valleys. Besides, the substrate is essencial to the PL properties of monolayer TMDs. Taking WS_2 as an example, monolayer sample can be well prepared on different substrates, such as SiO_2, *h*-BN and graphite (or graphene).[47-49] Although WS_2 monolayer possessed high PL efficiency when prepared on SiO2 substrate, the full width at half-maximum (FWHM) was reported to be ~42-68 meV. Graphite and *h*-BN have been used as the substrate to grow monolayer TMDs by considering both of them not only prossess atomically flat surface but also are free of dangling bonds. Monolayer WS_2 prepared on *h*-BN substrate exhibited limited crystallographic orientation due to the interlayer Coulomb interaction with the underlying *h*-BN.[49] In addition, WS_2 monolayer showed intense emission peak with a quite small FWHM of 26 meV. Moreover, monolayer WS_2 grown on graphite with a cleaved surface exhibited a single PL peak with almost perfectly symmetric Lorentzian profiles.[48] The narrow emission peak showed a small FWHM of 21 meV at room temperature and 8 meV at 79 K. No additional excitonic peaks were observed, indicating nearly perfect monolayer crystal without charged impurities and structural defects were grown on cleaved graphite substrate.

Furthermore, strain engineering is a powerful strategy for improving the performance of electronic, optoelectronic, and spintronic devices. By applying a strain, the electric band structure of 2D materials can be modified. Generally, there are two types of strain, i.e., uniaxial and biaxial. The former one can be achieved by bending or stretching the 2D materials,[128,129] while the later one can be delivered to 2D materials by employing the piezoelectric materials.[130] When an uniaxial tensile strain is applied, a red shift in the optical band gap of MoS_2 that is approximately can be obviously detected.[128] The tunability of ~45 meV/% strain for monolayer MoS_2 and ~120 meV/% strain for bilayer MoS_2 can be achieved through the uniaxial tensile strain. Besides, a pronounced strain-induced decrease in PL intensity can be observed, which can be attributed to the direct-to-indirect transition of band gap for monolayer MoS_2. The decreased PL intensity disappears in bilayer sample.

Furthermore, under uniaxial tensile strain, emission peak broadening and side shoulder at the longer-wavelength can be observed in PL of monolayer WS_2, suggesting the direct-to-indirect bandgap transition.[129] As the strain increases further, the spectral weight of the indirect transition gradually increases. Over the entire strain range when increasing the tensile strain, the emission peaks attributed to direct and indirect bandgap transitions exhibit a monotonous linear red shift. Moreover, the binding energy of the direct transition is found to be a little smaller than that of the indirect transition. On the other hand, under biaxial compressive strain, a blue shift in bandgap of 300 meV/% strain was reported for tri-layer MoS_2 by a piezoelectric substrate.[130] The tunability of the indirect band gap by biaxial compressive strain is much high than the aforementioned one of the direct bandgap through uniaxial tensile strain. It is interesting that the applied biaxial strain can enhance the PL intensity, which can be well addressed by the indirect-to-direct band gap transitions in tri-layer MoS_2.

3.3 PL in doped TMDs

In general, dopants govern the inherent physical properties of numerous solid materials, especially semiconductors where chemical doping has been widely utilized to tune the features of the electronic devices[131,132]. Abundant doping methods have been developed for modulating other electronic and photonic materials (graphene, perovskite, organic semiconductors, etc.), and to date several doping approaches have been used for adjusting the emission in 2D semiconductor materials[133,134]. In principle, dopants can introduce novel electronic states or modulate the bandgap structure in 2D semiconductor materials, leading to the tuing of PL[135]. As a typical example, Robinson and co-workers fabricated the Mn-doped monolayer MoS_2 by vapor phase deposition techniques[136]. They found that the doping of Mn into the lattices (**Figure 7a**) modulates the photonic properties of monolayer MoS_2. The PL of monolayer MoS_2 presents a red shift and intensity quench. They deduce that the introductions of lattice defects and local electronic states caused by Mn doping may lead to change in PL. Then Koratkar and co-authors prepared Nb doped WS_2 and Re doped MoS_2 by CVD

methods[137]. Figure 7b presents the structure model attained from annular dark-field (ADF) scanning TEM (STEM) image of Nb doped WS_2, where the W and Nb atoms are signified in white and blue, respectively. Figure 7b suggests that the atomic distribution of Nb atoms differs from isolated dopants to clusters and 1D chains. The Nb atom content can be estimated as Nb/(Nb + W) ;: 6.7%. The PL spectra of monolayer undoped WS_2 and Nb doped WS_2 nanosheets are shown in Figure 7c. The A exciton PL band originating from direct-gap recombination between the *K*/*K*' points presents an almost 40 meV red shift. Differing from Mn-doped monolayer MoS_2, both their experimental results and theoretical prediction confirm that the *K*-point bandgap decreases and Nb doping does not provide any mid-gap states in the Brillouin zone. While the PL peak of Re doped MoS_2 shows a slight blue shift as compared with undoped MoS_2. The introduction of Re leads to an increase in the *K*-point gap and a shallow donor level. Kim and co-authors fabricated n-type chemical doping of MoS_2 nanosheets with reduced benzyl viologen (BV)[138]. As shown in Figure 7d, the confocal PL spectra adjusted by the reduced BV doping have a strong dependence on the layer number. The PL peaks presented a remarkable red shift in the monolayer MoS_2, ascribed to the reduction of the *K*-point gap energy. Meanwhile, the PL peaks from A and B excitons were significantly quenched in the monolayer MoS_2 whereas considerably less effect was presented in fewer layers. Differing from the above, our group realized the upconversion and downconversion NIR PL of rare earth ions Er by using layered MoS_2 nanosheets as hosts[139]. As shown in Figure 7e, atomic scale CS-STEM image of Er-doped MoS_2 nanosheets indicates Er atoms can substitute in the Mo sites. The PL mapping image in Figure 7f displays upconversion peaks around 800 nm in Er-doped MoS_2 nanosheets, originating from the energy transition of ${}^4I_{9/2} - {}^4I_{15/2}$ of Er^{3+}. Figure 7g shows the downconversion PL emitted at around 1540 nm of Er-doped MoS_2 nanosheets due to the energy transition of ${}^4I_{9/2} - {}^4I_{15/2}$ of Er^{3+}. The introduction of Er dopant greatly extends the emission band of MoS_2 nanosheets.

Considering the abundant energy levels of rare earth ions, this work opens a door to significantly extend and modify the emitting wavelengths of 2D semiconductors. Therefore, doping in 2D semiconductors will benefit for not only studying numerous appealing fundamental issues, but also developing novel photonic devices.

Furthermore, Pan's group recently reported a continuously modulated PL ranging from 680 to 755 nm in lateral composition graded bilayer $MoS_{2(1-x)}Se_{2x}$ nanosheets synthesized by continuous lateral growth using CVD method.[140] The x is the composition ratio, equal to Se/(Se+S). Through an improved CVD method, some lateral composition graded ternary $MoS_{2(1-x)}Se_{2x}$ alloys can be well fabricated by control of the vaporization of the source materials of MoO_3, sulfur and selenium powder. At the initial growth, a typical MoS_2 triangular nanosheet can be synthesized to serve as a seed. Followed by this, Se atoms begin to react with MoO_3 after the selenium powder is evaporated. As a consequence, the composition graded $MoS_{2(1-x)}Se_{2x}$ alloy in the lateral direction can be prepared, as schematically shown in **Figure 8a**. The composition of the nanosheet can be gradually tuned from $x = 0$ to $x = 0.68$ from the center to the edge. In the whole triangular nanosheet, Mo is uniformly distributed, while S composition is gradually decreasing from the center to the edge with essentially 1 at the center, and Se exhibits the opposite trend to S. Figure 8b shows the position (composition) dependent PL spectra of an individual nanosheet, as marked in the inset of Figure 8b. From the center (position a) to the edge (f) of the nanosheet, the spectra show single emission bands, with the peak wavelength gradually red-shifted from 680 to 755 nm. Figure 8c exhibits the corresponding position-dependent compositions and bandgap values where black triangles stand for the compositions of Se and the red circles are for the bandgap values extracted from the PL spectra which are in good consistency with the green rectangles obtained from the calculation according the bandgap relation. Thus, the bandgap of

the synthesized nanosheet possesses a tunable bandgap which can be continuously modulated from the center 1.82 eV (680 nm) to the edge 1.64 eV (755 nm).

Moreover, such tunable PL emission has been achieved through synthesis of a series of alloy nanosheets of $WS_{2(1-x)}Se_{2x}$ with continuously tunable alloy compositions by varying the growth parameters.[141] As shown in Figure 8d, triangular nanosheets with continuously tunable S ratio can be well synthesized by the well-controlled CVD method. Figure 8e demonstrates the PL spectra of a series of $WS_{2(1-x)}Se_{2x}$ nanosheets with emission peak from 626.6 nm continuously tunable to 751.9 nm where 626.6 and 751.9 nm corresponding to the emission peak of WS_2 and WSe_2, respectively. By adjusting the chemical composition of the nanosheets, the optical and electric properties can be well controlled. Very recently, Pan's group has utilized this method to synthesize the 2D lateral heterojunction of MoS_2-$MoS_{2(1-x)}Se_{2x}$ with a tunable bandgap. [142] The observed wide band and tunable emission behaviors for such chemical composition varying 2D TMDs nanosheets are important for exploring new functional electronic and optoelectronic devices.

3.4 PL in 2D materials beyond TMDs

3.4.1 PL in black phosphorus

Recently, BP attracts substantial research interest due to its 2D counterpart, namely phosphorene, exhibiting tunable bandgaps, strong light-matter interactions and excellent electronic transport properties.[21-23,143] In contrast to the semimetal nature of graphene, phosphorene is semiconducting with a non-vanishing direct bandgap. Meanwhile, the optical conductivities of phosphorene can be effectively tuned by different number of layers, which is highly preferred for semiconducting photonic devices.[23,144,145] The optical properties of phosphorene have been investigated by PL spectroscopy.[20,146,147] **Figure 9a** presents the PL spectra of few-layer phosphorene nano sheets with different thickness obtained by mechanical exfoliation (2~5 layers).[146] It is observable that both position and intensity of measured PL

peaks are strongly dependent on the number of layers. From 5-layer to monolayer phosphorene, the measured peak energies cover a broad range from 0.8 ± 0.02 eV to 1.75 ± 0.04 eV (Figure 9b).[20] Apart from the crystalline BP nano sheets, it is reported that the highly-disordered BP ultrathin films exhibit similar thickness dependent trend.[148] The PL emission represents the optical bandgap of phosphorene, which can be obtained from the difference between the electronic bandgap and the binding energy of BP excitons (inset of Figure 9b).[20] The rapidly increasing of optical bandgaps of phosphorene along with decreasing of thickness can be explained by the vdW interlayer interactions and strong quantum confinement effect.[149]

In addition to its tunable bandgaps, phosphorene also exhibits unique in-plane anisotropic optical and electrical properties.[149,150] The exfoliated monolayer BP nano sheets have been studied by polarization-resolved PL spectroscopy, showing highly distinct luminescent along different orientations.[151] Figure 9c illustrates the relationship between the intensity of PL emissions and probe directions for different polarization angles of excitation. The PL intensity attains its maximum value when both probe and excitation polarizations are along the *x* orientation, while it is minimized when the probe is along the *y* direction. Moreover, no matter what the excitation polarization is like, the PL intensities of *y* direction is always less than 3% of those along the *x* direction. The highly anisotropic feature of luminescent is dominated by the anisotropic BP excitons, which is also an evidence of the distinct transport behaviours of phosphorene along either zigzag or armchair directions. The binding energy of exciton in phosphorene has been obtained by PL excitation spectroscopy.[151] Figure 9d shows the 2D mapping of PL intensity as a function of both excitation and emission energies. The PL intensity of monolayer BP is largely enhanced when the excitation energy is around 2.45 eV. The optical bandgap can be obtained to be 1.3 ± 0.02 eV, while the quasi-particle bandgap can be estimated to be 2.2 ± 0.1 eV. Thus, the binding energy of excitons in phosphorene, which is the difference between the ground-state exciton energy and the quasi-

particle bandgap, can be calculated as 0.9 ± 0.12 eV, which is superior to those of reported monolayer TMDs.[39,152] The experimental results are consistent very well with the first principles calculation. In addition, typical quasi-1D exciton behaviour is clearly observed, which confirms the anisotropic nature of BP exciton once again.

In addition to the excitonic effect, quasi-1D trionic behaviors in phosphorene have also been observed.[20,153] In general, the density of trions can be controlled by electrostatic modulation. Figure 9e demonstrates the gate biases modulated PL spectra of tri-layer phosphorene, exhibiting two luminescent peaks located at ~1100 and ~1300 nm, which correspond to emissions of BP excitons and positive trions, respectively.[153] When gate voltage is around −50 V, the PL peak at 1300 nm is significantly enhanced while vanishing of peak at 1100 nm since the negative gate voltage could convert BP excitons to trions. With gradually increasing of the gate biases, the PL intensity of trions is progressively diminished. Such behaviour of trions modulation by gate biases has also been observed in monolayer MoS_2.[154] Moreover, the binding energy of BP trions is calculated to be ~162 meV, which is much larger than those found in other 2D semiconductors.[153] Same as the excitonic effect, the high trion binding energy obtained in tri-layer BP is also attributed to the anisotropic excitonic feature, which is verified from the results of angle-resolved PL characterization (Figure 9f).

Although the unique anisotropic optical properties of phosphorene provide new platform to investigate exciton dynamics of 2D materials, the quasi-1D excitons and trions may weaken the QY of luminescence due to the existence of local quenchers in the quasi-1D system.[153,155] On the other hand, these 0D local states may also act as seeds for luminescence, which would enhance the efficiency of photon emissions or emit light with new wavelength.[156,157] Recently, Xu et al. brightened the BP excitons with luminescent interfacial local states by exploiting plasma-enhanced CVD (PECVD) oxide substrates.[158] As illustrated in Figure 9g, the quasi-1D excitons in phosphorene can be trapped in the point defects at the

interface between phosphorene and PECVD oxide substrate, resulting in the formation of 0D exciton, which emits brighter luminescence than that from quasi-1D excitons. The localized 0D like excitons can be observed at elevated temperature, which is in contrary to the cryogenic temperature for observation of defect induced PL from TMDs. Figure 9h shows the PL spectra obtained from different spots on phosphorene/PECVD oxide. The large deviation of PL intensity reveals that the density of localized states is distributed non-homogeneous. Meanwhile, the QY of PL from 0D like excitons exhibits around 33.6 times higher than the original phosphorene, which may be attributed to the decreasing of non-radiative decay rate and raising of possibility of radiative recombination. Based on the above findings, phosphorene with quasi-1D excitons and trions, plus 0D localized states show great potential for future photonic applications.

3.4.2 PL from IIIA metal chalcogenides

Recently, group IIIA metal chalcogenides have attracted considerable attention thanks to their promising optical and optoelectronic properties.[159][160] Among the family of IIIA metal chalcogenides, InX and GaX (X = S, Se and Te) layered nanosheets have shown large and tunable optical bandgaps, dramatic nonlinear photonic effect and strong photoresponse, making them potentially useful for optoelectronic device design.[27,161] In particular, layered indium selenide (InSe) exhibits a thickness dependent bandgaps from 1.26 eV (bulk) to 2.11 eV (monolayer) due to the strong quantum confinement effect, covering a broad region from visible to infrared, which is comparable to that of BP.[26] Interestingly, ultrathin InSe shows a direct-to-indirect bandgap crossover along with decreasing of thickness (L < 6 nm), which is complete contrary to that of MoS_2.[159,162] As shown in **Figure 10**a, along with decreasing of film thickness, the emission energy of PL peaks from *γ*-InSe nanosheets shows strong blue shift to higher energy, while intensity of the peaks attenuates dramatically accordingly.[162] Specifically, the reduction of PL intensity is over 10 times when the thickness is below 10 nm, which is significantly beyond the expectation of regular attenuation by thickness. This effect

may be dominated by the crossover from direct to indirect bandgap for the extremely thin samples. At the same time, the FWHM of the PL peaks are gradually broadened with decreasing of thickness. These observations are consistent with the quantum confinement of photocarriers. Our group observed the similar thickness dependent PL spectra in wafer-scale InSe nanosheets prepared by pulsed laser deposition.[27]

The bendable optical properties of InSe nanosheets have been studied by PL spectroscopy for samples on flexible substrates.[163] Figure 10b exhibits the PL spectra from both bending and flat states of multilayer InSe nanosheet (thickness = 30 nm), which were excited by a 405 nm laser at temperature of 10 K.[163] The luminescence from both bound exciton complexes and free exciton can be observed. It is noteworthy that the PL intensity from InSe under bending is around 6 times stronger than that from the normal flat state, which may be attributed to the enlargement of emission angles of each luminescent InSe lattice upon bending the samples. This finding would promote the development of flexible devices based on layered InSe.

Apart from the multi-layered samples, the ultrathin InSe nanosheets (layer number :S 7) have been characterized by PL spectroscopy recently.[26] As atomically thin InSe is easily influenced by the chemicals in air, the exfoliated few-layer InSe nanosheets are covered by a thin layer of *h*-BN for protection. As a result, the PL spectra of 2 to 8 nm thick InSe excited by a higher energy show different emission peaks compared with those of lower excitation energy (Figure 10c).[26] Both high- and low-energy peaks exhibit blue shift along with decreasing of layer number, which is in consistent with the trend for multi-layer InSe. In particular, the PL emission of monolayer InSe can only be observed under high energy excitation. As shown in Figure 10d, no PL response is obtained from the PL mapping for monolayer InSe excited by 2.7 eV laser. The relatively higher visibility for PL excited by high energy can be explained by the large discrepancy of wave functions of electronic states in

different valence bands. The absence of emission from monolayer InSe may be caused by the preventing of optical response by the mirror symmetry of the single layer crystal.[26,164]

The magneto-PL effect has been observed in both bulk and 2D InSe nanosheets.[164] For the bulk InSe, the PL intensity increases and the position of peaks shows blue shift with increasing of magnetic field *B*. On the other hand, for the ultrathin InSe nanosheets (*L*~ 5 layer), the PL spectra exhibit two distinct peaks X_1 and X_2 under magnetic field. As shown in Figure 10e, with increasing of *B*, the position of X_2 shows a linear blue shift as well as dramatically enhancement of emission intensity, indicating that the emission is induced by the delocalized excitons. On the other hand, the intensity and peak position of X_1 are almost independent of *B*, which may be contributed by the excitons that are strongly confined.[164] In both theoretical and experimental ways, it has been confirmed that the excitons and electron in-plane masses of thin InSe nanosheets (< 5 layers) are nearly independent on the layer number. Although ultrathin InSe exhibits an indirect bandgap, the material still shows strong photoresponse due to the weakly dispersed valence band, which enables the development of novel optoelectronic devices based on 2D InSe.

Morphology engineering has been proved to be one of the effective ways to manipulate physical properties of 2D materials.[165,166] Recently, Brotons-Gisbert et al. have largely enhanced the photoresponse of atomically thin InSe nanosheets at room temperature by means of nanotexturing.[167] To modify the morphology of InSe nanosheets, a number of SiO_2 nanoparticles (NPs) with the size of ~100 nm have been grown on SiO_2/Si substrates before depositing 2D InSe (Figure 10f). The high roughness of the InSe nanosheets induced by these NPs can be clearly observed from the morphology mapping obtained by atomic force microscope (AFM) as shown in the middle image of Figure 10f, indicating a high degree of texturization in the nanosheet. As a result, the PL emission of this InSe sample is shown up by an integrated intensity map, revealing a highly correspondence with the morphology map, in which the enhanced PL emissions correspond to the highly textured areas (Figure 10f). This

manipulating of luminescence behaviour of InSe is mainly caused by the resultant effect of light scattering by the NPs and agglomerates as well as the large light anisotropy in ultrathin InSe nanosheets. This work opens the new platform to design the controllable and flexible optoelectronic devices based on 2D semiconductors.

3.5 PL in 2D vdW HSs

Thanks to the harvesting in 2D materials, mixed 2D HSs have sparked wide interest recently. 2D materials shift from gapless graphene to direct badgap TMDs as well as recently discovered black phospherene and demonstrate various physical properties in terms of electronic structure, exciton resonance, and optoelectronics. Even those TMDs share the same crystalline, their physical properties vary significantly. Therefore, stacking different 2D materials on top of one another to form 2D HSs is intriguing and show potential applications in some novel devices. By considering the dangling-bond-free surface contacts with another to form heterojunction through vdW interaction, the vdW coupled HSs can be constructed by vertically stacking two or more than two kinds of 2D materials.[168] In contrast to the vdW HSs, lateral 2D HSs were also reported by integrating two kinds of 2D materials in the same plane.[169] Besides, mixed-dimensional vdW HSs are constructed by integrating 2D and 0-, 1- and 3D materials.[170] In this subsection, we focus on 2D heterojunction consisting of 2D and 2D materials. Based on such 2D HSs, novel electronic and optoelectronic devices can be integrated, such as LEDs, photovoltaic devices, tunneling transistors.[29,171,172] Furthermore, some amazing functionalities that are not accessible in other HSs can be achieved in such 2D HSs. Herein, we review the recent development of PL as well as the underlying mechanism in the 2D HSs.

3.5.1 PL in vertical HSs

Among 2D HSs, much more attention has been put on vertical HSs where 2D materials are vertically stacking through the vdW forces. Actually, the PL spectra of the such HSs generally exhibit two peaks corresponding to the individual 2D layers.[173] It should be

pointed out that the interlayer charge transfer existing in the vdW HSs where the individual PL signals are quenched.[174-176] The interlayer charge transfer can induce the decreased PL intensity by considering the charge transfer between the two individual layer rather than forming excitons which can contribute to PL in each layer. In addition to the individual layer excitonic states existing in the vdW HSs, it is possible to achieve interlayer excitonic states in vdW HSs. The interlayer excitons are bounded electrons and holes that are localized in neighbouring layers. Such 2D HSs provide opportunity to investigate not only the intralayer but also the interlayer exciton optical responses in monolayer samples. In 2015, Xu's group reported the direct observation of interlayer excitonic states in vdW HSs of monolayer $MoSe_2/WSe_2$ though PL measurements.[177] The HSs are fabricated by stacking the mechanically exfoliated monolayer $MoSe_2$ and WSe_2. **Figure 11a** and b show the schematic and optical micrograph of the vertically stacked $MoSe_2$ and WSe_2 HS, respectively. The individual monolayers of $MoSe_2$ and WSe_2 as well as the vertically stacked HS provides a strategy to identify the interlayer excitonic state in the HS from the intralayer one in the individual monolayers. Figure 11c shows a typical PL spectrum measured at room temperature in the area of the HS where is outlined by the white line in Figure 11a. Three emission peaks can be clearly observed in the spectrum. Among them, the two dominate emission peaks locate at about 1.57 and 1.65 eV, resulting from the excitonic states in the intralayer of monolayer $MoSe_2$ and WSe_2, respectively. On the other hand, the emission peak at about 1.35 eV should correspond to interlayer excitons from the HS region. To confirm this, the 2D PL mapping integrated from the emission peak is performed and shown in the inset of Figure 11c. It is clear that the peak has uniform emission intensity and is observed only in area of the HS while no signal is found in the individual layers, suggesting the 1.35 eV emission peak corresponds to the interlayer excitons in the HS. The spectra of top WSe_2 monolayer and the bottom $MoSe_2$ monolayer as well as the HS are measured. All the intralayer excitonic states in both monolayers can be preserved in the HS PL spectrum.

Besides, the interlayer emission positions are slightly changed from different HSs due to the differences in the interlayer separation induced by the imperfect transfer as well as a different twisting angle between $MoSe_2$ and WSe_2 monolayers.

Furthermore, the electric field control of the interlayer emission is investigated. As schematically shown in Figure 11d, a vertical gate voltage is applied. The electron in $MoSe_2$ and hole in WSe_2 can form a dipole, pointing from $MoSe_2$ to WSe_2. When a gate voltage is applied, the electric field can tune the band structure of $MoSe_2$ and WSe_2 as well as the interlayer relative band-offset between the two monolayers. Figure 11e demonstrates the electrical control of the interlayer exciton resonance between of $MoSe_2$ and WSe_2. The relative band-offset can be reduced when a negative gate voltage is applied, giving rise to an increase in the energy separation between the WSe_2 valence band and the $MoSe_2$ conduction band. As a consequence, a blue shift can be observed in the interlayer emission, as shown in Figure 11f of the mapping image of interlayer exciton emission. Conversely, when $MoSe_2$ is put on top of WSe_2, the interlayer relative band-offset will be increased at a negative gate voltage, and finally a red shift will be observed on the interlayer excitonic emission spectrum. However, the interlayer excitonic emission can be enhanced as gate voltage decreases, suggesting the electric field induced carrier doping also can modify the interlayer emission intensity. Besides, time-resolved PL measurement demonstrates that the lifetime of the interlayer exciton is about 1.8 ns which is much longer than the intralayer exciton lifetime with the order of tens of ps. Similar work has been demonstrated by employing HS of n-type MoS_2 and p-type WSe_2.[172] All these works suggest that the HS can not only preserve the original intralayer excitonic states from monolayer samples, but also generate new interlayer excitonic states.

Moreover, it should be mentioned that stacking configuration is another very important modulation method to engineer band structure of 2D materials in vdW HSs. It was reported interlayer coupling effect in MoS_2 bilayers is strongly dependent on the twist angles

(*0*)between the two layers.[178] The excitonic states shift to low energies for AA- (*0* = 0°) and AB-stacked (*0* = 60°) bilayers, and a significantly smaller but obvious red shift for all other twist angles, suggesting different interlayer separations in various stacking configurations. The twist angles dependent PL properties have been investigated in 2D HSs.[173] Figure 11g-i shows the optical image of MoS_2/WS_2 bilayers with different twist angles of 0° 60° and 38°, respectively. In the MoS_2/WS_2 HS, CVD-grown large triangle layer of MoS_2 is located at the bottom, and the small triangle layer on top is WS_2 monolayer. Figure 11j shows the PL spectra of monolayer MoS_2 and MoS_2/WS_2 bilayers with differnet twist angles. The A exciton states for both MoS_2 (peak I) and WS_2 (peak II) with slight red shift can be clearly observed in all bilayer HSs. Furthermore, PL intensity for Peak I in HSs is significantly decreased compared to that in MoS_2 monolayer due to the interlayer charge transfer mentioned at the beginning of this section. Similar PL beahviors was reported in WSe_2/WS_2 bilayer HSs as well.[179]

3.5.2 PL in lateral HSs

In addition to aforementioned vertical HSs, lateral HSs fabricated by in-plane epitaxial growth have drawn much attention recently.[180-182] This may provide a new strategy for future applications in pure 2D optoelectronic devices, such as 2D lasers, 2D LEDs and 2D photovoltaic devices. Differing from vertical vdW HSs, the lateral HSs require the lattice match. Monolayer TMDs are good candidates for fabrication of lateral HSs due to their same crystal structure and very close lattice constants. And more importantly, some new HS properties may be stimulated by their unique electronic and optoelectronic properties. The lateral HSs can be fabricated by in-plane heteroepitaxy, as schematically shown in **Figure 12**a.[180] The lateral HS of $MoSe_2$ (lattice constant: 3.288 Å, bandgap: 1.550 eV) and WSe_2 (3.280 Å, 1.653 eV) can be well grown by physical vapor transport method. Generally, some equilateral triangles with size of 15 μm have been prepared. The scanning electronic miscroscope (SEM) image clearly show the triangular HSs, as shown in Figure 12b. The dark

equilateral triangles are monolayer $MoSe_2$ crystal, while the outer triangles are monolayer WSe_2. High-resolution TEM image demonstrates the 1D lateral interface of the fabricated HSs, as shown in Figure 12c of the aberration-corrected ADF STEM image. All the atoms (Mo, W, Se) lie on their honeycomb lattice. There are no structural dislocations or grain boundaries or phase transitions. The PL properties of the fabricated lateral HSs have been studied by scanning micro-photoluminescence measurements, as shown in the integrated PL intensity mapping image of Figure 12d. Figure 12e shows PL spectra measured at the three positions ($MoSe_2$, WSe_2, and the interface) marked by the colored arrows (red, green and dark) in Figure 12d. The spectra peaks of monolayer $MoSe_2$ and WSe_2 are located at 1.57 eV and 1.63 eV, corresponding to the direct bandgap excitons of them, respectively. On the other hand, the HSs exhibit a broader and brighter emission compared to the individual monolayer samples. The emission peak located at the intermediate energy of monolayer $MoSe_2$ and WSe_2. It should be noted that the enhanced PL in the lateral HSs may result from the trapping of excitons by defects or the increased radiative recombination at the interface. Similar works have been reported around lateral HSs based on monolayer TMDs, such as $MoS_2/MoSe_2$, WS_2/WSe_2, WSe_2/MoS_2, and so on.[183,184] Figure 12f show the SEM image of triangular WSe_2/MoS_2 lateral HS prepared firstly by van der Waals epitaxy of WSe_2 followed by edge epitaxy MoS_2.[181] Through the two-step epitaxy growth, atomically sharp transition can be achieved at the interface of the lateral HS, as shown in the high-resolution ADF STEM image of Figure 12g. Further investigations on the lateral HSs suggest the existence in the subsequent MoS_2 layer of large compressive (up to 1.1%) and tensile strain (up to 1.59%) originating from the lattice mismatch between WSe_2 and MoS_2. Figure 12h shows the PL spectra marked as 1 to 9 are measured at locations adjacent to the interface gradually changing from WSe_2 to MoS_2 through the interface. Among them, the spectra marked as 1 to 3 exhibit emission peaks at 1.62 eV, corresponding to WSe_2 direct bandgap exciton, while, spectra marked as 7 to 9 exhibit emission peaks at 1.85 eV, corresponding to MoS_2 direct

bandgap exciton. And, similar to aforementioned $MoSe_2/WSe_2$ lateral HSs, the emission measured at more adjacent to the interface exhibits stronger and narrower peak compared to the individual monolayer sample. The spectra marked as 4 to 6 clearly demonstrate the emission transition from WSe_2 to MoS_2 at the lateral interface. However, the interlayer emission observed in vertical HSs cannot be detected in such reported lateral junctions. In a word, such lateral HSs exhibit unique optical properties different from individual monolayer samples as well as their vertical counterparts.

4. EL in 2D Materials and vdW HSs

2D materials exhibit amazing electrical properties as well as fascinating optical properties as we mentioned above. The combination of electrical and optical properties in 2D materials not only provides opportunities to stimulate novel properties but also exhibits promising applications for future optoelectronic devices. Investigation of EL of 2D materials can provide us opportunity to combine the electrical and optical properties in such 2D form, leading to optoelectronic applications toward practical devices. However, there has been less work done on EL compared to the PL results of 2D materials due to relatively difficult device fabrication and weak signal measurements of EL. Herein, we review recent development of EL in 2D materials. Especially, the EL in lateral and vertical HSs constructed by 2D materials is introduced. The EL behaviors and the methods to modify the EL as well as the underling mechanism are summarized in this section.

4.1 EL in 2D TMDs

By considering the tunable and suitable bandgap in 2D TMDs, we take the most widely studied monolayer MoS_2 as an example to introduce the EL in 2D materials. **Figure 13a** shows EL spectrum of monolayer MoS_2 when the source drain voltage is biased with 5 V and the current is 100 μA.[185] To achieve the optimum EL spectrum, the source drain voltages are tuned to examine the EL emission by means of a single photon counting detector. The EL spectrum shows a feature peak located at about 685 nm with the FWHM of 40 nm. For

comparison, the PL and absorption spectra along with a high-bias EL spectrum are exhibited in Figure 13b. The two absorption features located at about 610 and 670 nm correspond to A and B excitons of monolayer MoS_2, respectively. The related PL peaks are located at about 620 and 680 nm, respectively. The EL emission peak matched well with the PL peak located at about 680 nm, suggesting the same exciton of B dominated EL and PL. However, the exciton observed in PL (620 nm) is not shown in EL spectrum. This may be caused by the relatively low electrical power density which is not enough to efficiently stimulate the higher energy excitonic state at 620 nm. The excitonic state at 620 nm, i.e., the trion, is formed when the photogenerated exciton binds to the free electron. In fact, sufficient kinetic or thermal energy is needed for electrons to generate excitons. Thus, there should be a threshold power density for EL emission which is dependent on the exciton binding energy, the channel semiconductor as well as the contacts between semiconductor and the source and drain electrodes. When the power density is in excess of the threshold value and the electrical bias is increased, spectral broadening and increased thermal background in EL can be observed, while no significant spectral shifts can be observed. Furthermore, the efficiency of EL is not homogeneously radiated in the overall monolayer MoS_2 sample. Figure 13c shows the overlapping image of EL mapping and the electrode positions, demonstrating that the EL emission is localized at one of the metal contacts. The exciton generation can achieve maximum in the area where the carrier injection occurs. Thus, at the source and drain electrodes, the efficiency of exciton generation is the strongest in the monolayer sample. In summary, EL in monolayer MoS_2 sample stems from the direct bandgap excitons located at 1.8 eV. Different from PL, EL exhibits threshold behaviors and is spatially localized near the electrode.

4.2 EL in 2D p-n homojunctions

Recently, EL has been reported to be observed in the lateral p-n homojunctions based on exfoliated monolayer WSe_2 and WS_2. The lateral p-n homojunctions can be constructed by

individual monolayer sample with the separated n-and p-type regions achieved by applying two independent gate voltages within the same layer.[169,186,187] Based on such lateral homojunctions, functions of solar energy conversion and light emitting can be achieved in the monolayer TMDs. Figure 14a show the schematic of the lateral p-n homojunction based on monolayer WSe_2.[169] The lateral p-n homojunction is formed by applying independent gate voltages to the two palladium gate electrodes underlying the exfoliated *h*-BN which can create two individually doped regions in monolayer WSe_2 layer separated by a undoped channel with the width of 300 nm. Figure 14b shows the EL intensity as a function of bias (source-drain) current and photon energy measured at 60 K. There are three EL emission peaks, i.e., a narrow higher-energy peak (centered at ~1.69 eV, corresponding to neutral exciton X^0, marked as green arrow), a broad central peak (~1.64 eV, the negatively charged trion X^-, brown arrow) with a high-energy shoulder (the positively charged trion X^+, grey arrow), and a lower-energy peak (~1.59 eV, impurity-bound exciton, X^I, black arrow). The shapes and relative intensities of the three feature peaks are current-dependent. To be more specific, the EL spectra with different currents are shown in Figure 14c, demonstrating sequential population of the excitons. As the current increases, the emission peaks corresponding to X^0, X^- and X^+ are all enhanced, while the X^I feature peak becomes broaden and weaken. At the lowest current (24 nA), only the excitons with lowest energy (X^- and X^I) can be observed, while X^+ shoulder and X^0 become visible at a higher current of 27 nA. The EL spectrum can be decomposed into four Gaussian peaks at current of 33 nA. Besides, the EL well matches the PL, suggesting the EL also results from the valley excitons. To fully understand the EL behaviors, the band diagram of the lateral p-n homojunction is plotted in Figure 14d. The filled and empty circles stand for carriers (electrons and holes) in the +K and −K valleys. The electrons and holes move to each other and then recombine to emit light. The doped electrons

and holes populate both the +K and −K valleys equally. As a consequence, the EL has both right and left polarization and the lateral junction produce unpolarized light.

Furthermore, the circularly polarized EL was observed from p-i-n junctions formed by 2D TMD monolayers in the electric double-layer transistor (EDLT) structures.[30] Similar to aforementioned p-n homojunctions, the p-i-n junction was fabricated. Since the WSe_2 based FETs exhibit ambipolar properties, simultaneous accumulation of both electrons and holes in the p-i-n junction can be achieved, giving rise to EL when controlling the potential difference between source and drain electrodes. Actually, the circularly polarized PL has already been observed in monolayer TMDs and biased bilayer samples when the 2D layers are excited by polarized incident light.[188-191] The observed polarized EL can be controlled by changing the current direction.

4.3 EL 2D in vdW HSs

As mentioned in the subsection 3.5, vdW HSs have drawn more and more attention recently. In this section, we review the recent development of EL in vdW HSs. In 2015, the electric-field-induced enhancement of EL in multilayer MoS_2 was reported.[192] The EL efficiency in multilayer sample is comparable to or even higher than that in monolayer MoS_2. By creating the HS of GaN-Al_2O_3-MoS_2, the multilayer MoS_2 exhibits direct bandgap excitonic EL emission over the entire vertical junction area. Furthermore, electrically tunable chiral EL was reported in monolayer CVD-grown WS_2 by constructing a p-i-n heterojunction with p-type Si and n-type ITO.[193] The EL emission can be achieved by injecting the forward current in monolayer WS_2, and can be tuned by varying the injection current. The degree of circular polarization reaches as high as 81%, which can be effectively modulated by forward current. In addition, EL was reported in vertical heterojunctions consisting of n-type monolayer MoS_2 and p-type silicon.[194] These EL studies provide an insight for realization of more sophisticated optoelectronic devices based on HSs.[29,195,196]

Figure 15a and b show the top and side view of the schematics for the vertical HS based on mechanically exfoliated MoS_2 and CVD-grown WSe_2.[195] By vertically stacking the 2D TMDs, the WSe_2/MoS_2 p-n junctions can be fabricated. The monolayer WSe_2 typically with a bilayer region in the center can be prepared by CVD method on Si/SiO_2 substrate. Then mechanically exfoliated MoS_2 is transferred onto the top surface of the WSe_2 layers. Thus, mono- and bilayer WSe_2/MoS_2 p-n junctions can be well fabricated in the experiments. Figure 15c demonstrates the ideal band structure of WSe_2/MoS_2 p-n junction with zero bias. Both the p-type WSe_2 and n-type MoS_2 layers are assumed to be neutral. The built-in potential can be formed in the depletion layer. Figure 15d shows the false color EL image of the WSe_2/MoS_2 p-n junction under an injection current of 100 μA. Differing from the photocurrent generated from the entire junction region, EL is localized at the junction area near the electrodes. Similar behaviors were observed in aforementioned PL of vertical HSs. This issue can be addressed by the electric field distribution in the p-n junction with different injection current. For photocurrent measured at zero bias voltage or a smaller one than the turn on voltage, the p-n junction resistance dominates the entire diode, and therefore, photocurrent can be created from the entire junction. For the EL observed under much larger forward bias in excess of the turn-on voltage, the resistance of the junction becomes less than that of the monolayer WSe_2. Thus a large potential difference can be formed at the junction edge near the electrodes due to the large series resistance of the monolayer WSe_2. Figure 15e and f show the EL spectra of the fabricated monolayer and bilayer WSe_2/MoS_2 p-n junction with different injection current, respectively. The EL intensity is negligible below the threshold junction current. Then EL shows a linear increase with the applied current in excess of threshold for both mono- and bilayer WSe_2/MoS_2 p-n junction. There are several feature emission peaks in the PL spectra. Among them, the peaks located at ~792 nm and ~626 nm can be assigned as excitonic peaks A and B, respectively. While, ~546 nm and ~483 nm peaks are ascribed to the hot electron luminescence (HEL) peaks A' and B', respectively. The indirect bandgap emission peak I is

located at ~880 nm. For monolayer WSe_2/MoS_2 p-n junction, the excitonic emission A is significant in the spectra of the EL. On the other hand, for bilayer WSe_2/MoS_2 p-n junction, the indirect bandgap emission I is comparable to the excitonic emission A. The two emission peaks are dominated in the PL spectra in bilayer WSe_2/MoS_2 p-n junction. It should be noted that the intensities of the HEL peaks are about 3~10 times weaker than A excitonic peak in the vertical junctions. Actually, the HEL peaks are usually 100~1000 times weaker than the excitonic peaks and seldom reported in EL. The enhanced HEL emission peaks can be attributed to the electric field induced carrier redistribution.

Similar vertically stacked p-n junctions have been reported by using n-type InSe and p-type GaSe.[197] Room-temperature EL was observed from the p-n junctions. Besides, EL has been reported in some other vertical HS by stacking different 2D materials in the well-designed sequences, such as metallic graphene, insulating *h*-BN and semiconducting monolayer TMDs in the sequence of BN/Graphene/BN/WS_2/BN/Graphene/BN.[29] Based on such vdW HS, the prepared LEDs exhibit an extrinsic quantum efficiency of nearly 10%. Such vdW HS can introduce quantum wells (QWs) engineering with one atomic thickness. The advent of HSs based on the atomically thin crystals provides extremely versatile 2D electronic and optoelctronic devices of FETs, LEDs, and photovoltaic devices.

5. Nonlinear optics in 2D Materials

5.1 Nonlinear PL in pristine graphene

The aforementioned emission in graphene and its derivatives can roughly be classified into two primary categories. One is originated from the generated energy bandgaps and the other is associated with the created defects. However, nonlinear optical properties of graphene have also been studied.[198-201] Among them, nonlinear broadband PL in graphene induced by excitation of femtosecond (fs) laser irradiation was reported by Wang's group in 2010.[202] Upon the fs laser excitation, an unusually bright, broadband light emission was observed from graphene layers with the emitting frequencies well above the excitation frequency. The

graphene sample was prepared by mechanical exfoliation method. **Figure 16a** shows the PL image of the same graphene sample under 1.5 eV excitation. The PL signal was integrated between 1.66 and 3.11 eV. The trend shows the thicker the graphene layer the stronger the PL signal, as demonstrated in the inset of Figure 16a. Figure 16b shows the PL spectra of a few-layer graphene sample under fs laser excitation of various frequencies, as marked by the arrows with different colors. The blue-shifted PL from the graphene sample was clearly observed. It should be noted that the red-shifted PL under 2.2 eV excitation is caused by the *G* and 2*D* Stokes Raman modes marked by asterisks "*". Moreover, the spectral profile remained similarly under different excitation laser and for the graphene sample with different thickness. The blue-shifted PL of comparable brightness and bandwidth to that in graphene was seldom reported in graphene. The possible mechanism of this unusually blue-shifted PL can be well addressed. The bright and broadband PL can be caused by the following three points. Firstly, the linear electronic bands of graphene can well satisfy both energy and momentum conservations for carrier-carrier scattering, while, the nonlinearly dispersive bands is much more limited for the process. Secondly, the nonequilibrium electrons and holes possess the symmetric distribution of in the linear bands, giving rise to the direct recombination of electrons and holes pairs. Thirdly, the energy acquired by an electron and hole pair via intraband scattering is the maximum in zerogap materials of graphene. Lastly, a high Coulomb scattering rate can be achieved and the dielectric screening can be greatly reduced in 2D graphene.

Additionally, significant ultrafast PL was reported from pristine monolayer graphene under excitation by fs laser pulses by Heinz's group.[203] Under excitation by fs laser pulses (1.5 eV), the graphene produced readily observable light emission across the visible to near ultraviolet spectral range (1.7-3.5 eV). For continuous-wave excitation of the same photon energy (1.5 eV), no light emission could be detected from graphene. Differing from conventional PL, this ultrafast PL has a nonlinear dependence on the pump excitation and the

integrated emission follows a power-law relation over the entire wavelength range. Moreover, the emitted light appears at photon energies well above that of the excitation. The observed spectrally broad light emission can be understood as a direct consequence of a transient regime in which the electron distribution is driven strongly out of equilibrium by ultrafast laser excitation. The strong dependence of the PL with pump energy rules out the possibility of hot luminescence due to a two-photon absorption process. PL intensity decreased with increasing photon energy, implying thermal nature of the emission.

5.2 Two-photon luminescence in TMDs

TPL occurs when 2D materials absorbing two photons simultaneously for the photons' energy less than the direct bandgap of the 2D material, while one-photon PL occurs when the excited photon energy larger than the bandgap energy of the measured sample.[204,205] Thus, TPL is a third order of nonlinear optical process.[206,207] Generally, high intensity pulse laser is needed as the excited light. Figure 16c schematically shows the TPL process in monolayer WS_2.[51] The electron transition occurs from the valence band maximum (VBM) to one of the excitonic dark states with odd parity (2*p*) through the process of two-photon absorption (TPA). After the excitation, the exciton experiences a fast relaxation to the excitonic ground state (1*s*) followed by emitting a photon (red arrow). Figure 16d shows the emission spectrum of monolayer WS_2 excited by an ultrafast fs laser with energy of 1.25 eV measured at 10 K. The peaks at 2.04 eV and 2 eV are the A exciton (1s state) and its trion peak, respectively. The trion peak is stronger than the A exciton one due to the exciton-trion equilibrium reached during the emission stage at low temperature. The strong peak located at 2.5 eV is the double energy of the excited fs laser, i.e., the SHG signal. Both the TPL and SHG signals can be confirmed by the quadratic power dependence, as shown in the inset of Figure 16d. At a low excitation level, both of them exhibit quadratic power dependence, confirming the two-photon absorption nature of the luminescence. The TPL signal saturates at a high excitation level due to heating or exciton-exciton annihilation effects. Besides, two resonances located at 2.28 and

2.48 eV can be detected, corresponding to two excitonic dark 2*p* and 3p excited states, respectively. Thus, TPL can be used to detect the exciton banding energy.

5.3 SHG and THG

It should be pointed out that the difference between the two types of nonlinear optical properties of TPL and SHG. TPL is a light emission process, involving the absorption of two photons simultaneously. SHG is a light scattering process, involving the simultaneous interaction of two photons with the nonlinear material without absorption. The nonlinear material is essential for SHG. Recently, SHG has been studied in 2D materials. For example, 2D GaSe crystal possess unique structure where a centrosymmetric centre is absent.[52] Its 2D layers have unique electronic and optoelectronic properties and can be used in Si integrated nano-devices, including FETs and photodetectors.[208-211] And more importantly, the nonlinear properties can be retained in its 2D form. Hence, SHG can be observed in 2D GaSe nanosheets.[212-214] Furthermore, SHG can be observed in monolayer and odd-number layered TMDs due to the absence of inversion symmetry.[215-219] In contrast, the SHG effects vanished or degraded in even-number layered TMDs because of the restoration of inversion symmetry. 2D *h*-BN layers also exhibit similar layer-number dependent SHG behaviors.[219,220] As shown in Figure 16d, the sharp and strong emission peak located at 2.5 eV (double energy of the excited fs laser of 1.25 eV) corresponds to SHG generated due to the absence of inversion symmetry in monolayer WS_2. Besides, SHG can be observed in some artificially stacked bilayer 2D materials with broken inversion symmetry.[216,220] Furthermore, a strong dependence of SHG intensity from monolayer WS_2 on the excitation energy was observed when excitation power is kept constant.[221] It should be pointed that strong SHG signal appears when the two-photon laser energy is in resonance with 1s A exciton (1.75 eV) and the 1s B exciton (2.17 eV). Besides, there are some other resonances in the SHG spectrum which need employing TPL to confirm the origin of these transitions.[51] Different from the SHG results, the 1s transitions are not observed in TPL from monolayer WS_2 due to forbidden

dipole selection rules. The resonance SHG can be used to further detect the exciton banding energy when combined with TPL.

THG is the third-order nonlinear optics. THG has been reported in 2D materials. Figure 16e shows the power dependence of the third harmonic for a graphene sample.[222] Inset shows the THG spectrum excited by fs laser of 1720.4 nm. THG peak is centered at 575.5 nm, which is very nearly equal to one-third of incident light wavelength. The observed emission signal is consistent with a cubic dependence on the incident power shown by the solid line which is the as expected THG signal power dependence. In comparison, no THG signal can be observed when the incident laser spot is moved from the graphene flake to the bare substrate. Besides, it should be noted that SHG signals from the graphene flakes are not measurable in this experiment by considering the symmetry of graphene. The SHG signals in graphene are expected to be weak due to its centrosymmetric structure. An effective third order susceptibility can be calculated to be in the order of 10^{-16} m^2/V^2. The strong third order response originates from the resonant nature of the light-graphene interaction, which also causes strong absorption of light. Furthermore, the THG effect in ultrathin MoS_2 crystals prepared by mechanical exfoliation method was reported by Zhao's group.[223] 586 nm (one-third of 1758 nm) signals can be detected when 1758 nm fs pulse laser is pumped. The effective third-order nonlinear optical susceptibilities are deduced on the order of 10^{-19} m^2/V^2. The nonlinear optical responses, including SHG and THG, can be enhanced if the bandgap energies of the 2D crystals are resonant with the incident light frequencies. The observed nonlinear response can be used to explore the band structure of the prepared 2D crystals. Figure 16f demonstrates the extracted third-order nonlinear susceptibility as a function of the incident wavelength (bottom axis) and the generated THG wavelength (top axis). There are two peaks, located at 650 and 595 nm, in the incident wavelength dependent nonlinear susceptibility. These two peaks are about 20 nm shorter than the excitonic peaks of A (670 nm) and B (620 nm), respectively. Thus the two peaks are attributed to the excitonic enhancement

of the SHG signals. Note that no THG signal can be detected when the incident wavelength is longer than 1980 nm as THG signal is below the excitonic resonances in this wavelength range. The observed THG effect is not restrictive on the selection of substrates. Thus, the THG effect can be utilized for identification of MoS_2 multilayer flakes with higher contrast compared to linear optical microscopy.

6. Applications of luminescence in 2D materials

6.1 Applications in LEDs.

2D layered materials are considered favorable for developing light-emitting devices thanks to their broadband photoresponse, flat and uniform surface, good electronic transport properties and strong light-matter interaction.[224,225] Among the 2D family, monolayer TMDs exhibit predominance for light emitting applications because the interband transitions of TMD are relevant to both momentum and spin degree of freedom, respectively.[224,226] A chiral light-emitting transistor has been designed by fabricating a p-i-n junction using architecture of electric-double-layer transistors with channel of WSe_2 nanosheet (**Figure 17**a).[30] The circularly polarized EL emission has been observed by the device demonstration, which can be explained by the overlapping of electron-hole pairs controlled by the external electric field. In addition, the monolayer WSe_2 based lateral p-n junction has also been developed to LEDs electrostatically, which exhibits large photo emission rate of ~16 milion/s under applied current of 35 nA (Figure 17b).[169] This light emission is mainly attributed to the neutral excitons, trions and the impurity excitons, respectively, which can be tuned by controlling the injection bias. Moreover, the good matching of EL and PL results indicates that the EL is also generated by the valley excitons.

The TMDs-based HSs have been proved to be another promising candidate for producing LEDs.[29] A vertical HS based on insulating *h*-BN, conducting graphene and semiconductive WS_2 has been designed for light-emitting device, which shows many advantages compared with the lateral p-n junction, such as low contact resistance, high current density and large

area for light emitting (Figure 17c).[29] The electrons and holes from graphene layers recombine after injecting into WS_2, which then emit light accordingly. The LED fabricated by single HS shows external quantum efficiency (EQE) of 1 % and line widths down to 18 meV. Moreover, by using 3 or 4 quantum wells based on the HS, the devices exhibit EQE up to 8.4 %, which is comparable to that of commercial organic LED.[29] Apart from the mechanical exfoliated samples, the CVD grown large scale monolayer WS_2 has been developed into LEDs by fabricating a p-i-n heterojunction of p-Si/WS_2/ITO (Figure 17d).[193] Typical rectifying characteristic of LED was obtained from the $I-V$ curve at room temperature. The emission from monolayer WS_2 can be tuned by the injection current. In addition, the new circular polarization can be observed from the EL spectra, exhibiting a large degree of circular polarization of 81%, which are tunable by the applied current. The demonstration of LEDs based on CVD grown WS_2 brings new opportunities to develop real light emitting applications based on 2D materials and their HSs. Furthermore, single quantum emitters (SQEs) based on excitons were reported in 2D TMDs recently.[227-229] SQEs are the essential devices for quantum optics and photonic quantum technologies. The observation of photon antibunching from the monolayer WSe_2 based SQEs suggests the practical applications in quantum information processing. Single-photon sources have been demonstrated in 2D monolayers, which offer potential for developing integrated quantum technologies.[230,231]

Moreover, graphene and its derivates have been widely used in light emitting devices. Graphene has the potential to serve as transparent and flexible electrode to potentially substitute traditional indium tin oxide anodes in LEDs.[232] However, the efficiency of graphene-based LEDs has been limited due to its low work function and large sheet resistance. It was reported that graphene layers can reach a high carrier doping level and low sheet resistance by ferroelectric gating s.[233-235] Besides, flexible organic LEDs (OLEDs) with modified graphene anode was reported to exihbit high efficiency by increasing its surface work function via creating a work function gradient from the graphene to the overlying

organic layer and reducing its sheet resistance via chemical doping.[232] Compared to graphene, GO is fluorescent over a wide range of wavelength, suggesting potential applications in electronics and optoelectronics of electroluminescent cells, photodetectors and so on[63]

6.2 Applications in 2D Lasers.

Recently, monolayer TMDs have been employed in 2D lasers. In 2015, Xu' group reported an ultralow-threshold nanocavity laser by introducing monolayer WSe_2 into the pre-fabricated photonic crystal cavity.[31] In the laser device, monolayer WSe_2, serving as a gain medium, confines direct-gap excitons within one nanometer of the PCC surface. Gain-cavity coupling is experimentally achieved by directly transferring the monolayer onto the surface of the cavity through the well developed transferring method for 2D materials. When pumped by continuous-wave laser (632 nm), a very sharp polarized laser emission with line width of 0.3 nm at the half maximum is located at 739.7 nm. Furthermore, Zhang' group reported monolayer excitonic laser by embedding monolayer WS_2 into a microdisk resonator.[33] Monolayer WS_2 was introduced between two dielectric layers (Si_3N_4 and hydrogen silsesquioxane) which generates strong optical confinement and leads to a larger modal gain. Coherent light emission from a TMDC monolayer can be achieved. In 2017, room-temperature 2D laser was reported by embedding monolayer WS_2 into a half-wavelength-thick nanocavity.[32] The fabricated vertical-cavity surface-emitting laser suggests a major step to practical applications of monolayer materials in 2D lasers.

6.3 Applications in biomedicine

Biomedicine is one of important application areas of luminescence.[236-239] The intrinsic luminescence of GO in a broad range makes it attractive for biological applications of drug delivery and live cell imaging.[240,241] Recently, utilizing the rather large surface area and excellent optical properties, the atomically thin 2D TMDs have drawn considerable attention in biomedicine areas, including cancer treatment, detection of biomolecules, and bioimaging.[34,35] In general, several 2D nanosheets have high absorbance in the NIR region,

can be utilized as photothermal agents for cancer therapy.[242] As a typical example, Liu's group has developed a series of metal ions into WS_2 nanoflakes, and they chose Gd^{3+}-doped WS_2 with polyethylene glycol (PEG) modification as a multifunctional agent for imaging-guided combination cancer therapy[243]. They use WS_2:Gd^{3+}-PEG to carry out *in vivo* united photothermal/radiation therapy. Mice bearing 4T1 tumors were first injected WS_2:Gd^{3+}-PEG nanoflakes (2 mg/mL, 200 μL for each mouse) for 24 h, and then exposed to the 808 nm laser (0.5 W/cm^2). As shown in **Figure 18a**, the tumors' surface temperature for mice injected with WS_2:Gd^{3+}-PEG fast raised to ~47 °C within 1 min of laser irradiation and stayed at this temperature for 10 min. By contrast, the tumor temperature on mice without injection showed no significant heating effect under the same laser irradiation. Their works suggest that metal ions doped WS_2 nanoflakes can be applied in cancer therapy. Notably, TMD nanosheets are very favourable for the application of biosensors for detection of biomolecules, because of the direct dispersion in aqueous solution and large-scale production. As shown in Figure 18b, the surface of monolayer TMD nanosheets can absorb the dye-labeled single-stranded DNA (ssDNA) probe (P) via the vdW force between the basal plane of nanosheets and nucleobases, leading to the high fluorescenc quenching of the dye.[244] In contrast, the double-stranded DNA (dsDNA) presented much weaker interaction with the monolayer TMD nanosheet, therefore the luminescence intensity can be recovered once the dsDNA forming via the probe DNA hybridized with the target DNA. Consequently, the fluorescence intensity of probe can offer a quantitative detection for the target DNA. Zhang's group has demonstrated that several monolayer TMD nanosheets could be an efficient sensing platform for the detection of DNA and small molecules, based on their adsorption and fluorescence-sensor abilities.[245] As a representative example in Figure 18c and d, the PL intensity improved apparently along with raising the concentration of T1 from 0 to 20 nM and exhibited linear relationship over the range from 0 to 5 nM in TaS_2 nanosheet-based nanosensors. The limit of detection can reach up to 0.05 nM. More importantly, such detection could be completed within 5 min. Lin's

group has developed MoS_2@Fe_3O_4-ICG/Pt(IV) nanoflowers for magnetic resonance/infrared thermal/photoacoustic trimodal bioimaging and combined photothermal therapy/photodynamic therapy/chemotherapy triggered by 808 nm laser.[246] As shown in Figure 18e, an intensive green fluorescence can be observed in the MoS_2@Fe_3O_4-ICG nanocomposites, indicating that MoS_2@Fe_3O_4-ICG group can make more ROS generation in Hela cells. The results suggest the good application outlook of MoS_2@Fe_3O_4-ICG nanocomposites as a promising photodynamic agent.

7. Conclusions and Perspectives

Luminescence in 2D materials is not only essential for characterization of basic physical properties of 2D materials, especially the bandgap energies, excitonic energies and binding energies, but also significantly important for devices applications in optoelectronics, biomedicine and future quantum information technologies. The unique 2D structure and the amazing properties provide 2D materials an unprecedented platform for the scientific research and future applications. The luminescent behaviors in 2D materials can be triggered by the source of light or electricity due to the existence of the suitable bandgap, various excitonic states, doped ions, fabricated vdW HSs, as well as the intrinsic and external defects. Furthermore, the luminescence can be controlled or enhanced by applying one or two tunable gate voltage and chemical and/or physical treatments. A near-unity emission QY could be achieved in monolayer TMDs. A wide range of PL position and intensity in 2D InSe and BP can be achieved due to the existence of widely tunable bandgaps from multilayer to monolayer formed by the strong quantum confinement effect. PL and EL in 2D lateral and vertical heterojunctions as well as homojunctions demonstrate potential application for future light-emitting and photovoltaic devices. Besides, nonlinear luminescence in 2D materials suggests the applications in ultrafast optics.

Despite rapid progress has been made, there are still numerous challenges that need to be overcome for further study and applications of luminescence in 2D systems. The first one is the issue on improving their emission efficiency. Although many methods have been introduced to improve the emission QY in 2D TMDs, relevant research are seldom reported in 2D materials beyond TMDs. The second one is to better understand exciton based recombination kinetics. A number of theoretical and experimental studies are put on the mechanism of exciton in 2D platform. It is much needed to develop a unified model to provide an insight into the physical mechanism of the excitonic emission as well as the effects from intrinsic inhomogeneity, external doping, contaminants and surrounding environment. Thirdly, the tunability of luminescent range from the individual 2D crystal is very restrictive even though the versatile electronic bandgaps are achieved in 2D family. It may be beneficial to extend the luminescent spectral range by utilizing various homo- and heterojunctions as well as introducing dopants, which is similar to the observation on near infrared up-/down-conversion luminescence by introducing lanthanide dopant to 2D materials firstly done by our group.[139] All these problems to be solved provide us opportunities to further investigate and explore luminescence behaviors in 2D materials in hope of finding new luminescent properties in the 2D limit or new luminescent 2D materials.

Moreover, there are some bottlenecks in fundamental studies and future applications relevant to luminescence of 2D materials. One lies in unstable physical and chemical properties of 2D materials and the induced imperfect crystal quality. The induced defects and existence of imperfections often blur the intrinsic information. For example, the external factors could induce the broad linewidth of the intrinsic emission peak. Furthermore, the complicated process and rigorous environment of fabricating of 2D platform, especially the 2D vdWs HSs, restrict the widespread scientific research and practical applications. Although reliable HSs are previously explored, large-area fabrication of high-quality 2D hetero- and homojunctions is likely to have diffculties in meeting the requrements for real applications.

Given that 2D materials show potential for future applications, ranging from photovoltaic and LEDs to photodetectors and ultrafast lasers, many research topics centered on the luminescence in 2D materials are considerablly significant. Overall, the vast isolation and preparition of 2D materials as well as integration vdW HSs suggest considerable future fabrication of 2D system devices, and more importantly, provide potential applications in future optoelectronics and biological and quntum-technology fields.

Acknowledgements
This work was supported by the grants from Research Grants Council of Hong Kong (GRF No. PolyU 153281/16P) and National Natural Science Foundation of China (No. 61604100).

Received: ((will be filled in by the editorial staff))
Revised: ((will be filled in by the editorial staff))
Published online: ((will be filled in by the editorial staff))

References

[1] K. Ziemelis, *Nature* **1999**, *399*, 408.
[2] M. A. McCarthy, B. Liu, E. P. Donoghue, I. Kravchenko, D. Y. Kim, F. So, A. G. Rinzler, *Science* **2011**, *332*, 570.
[3] M.-K. Tsang, G. Bai, J. Hao, *Chem. Soc. Rev.* **2015**, *44*, 1585.
[4] M. Nirmal, L. Brus, *Acc. Chem. Res.* **1999**, *32*, 407.
[5] J. C. Goldschmidt, S. Fischer, *Adv. Opt. Mater.* **2015**, *3*, 510.
[6] Z. Wu, G. Bai, Q. Hu, D. Guo, C. Sun, L. Ji, M. Lei, L. Li, P. Li, J. Hao, W. Tang, *Appl. Phys. Lett.* **2015**, *106*, 2.
[7] K. S. Novoselov, A. K. Geim, S. V. Morozov, D. Jiang, Y. Zhang, S. V. Dubonos, I. V. Grigorieva, A. A. Firsov, *Science* **2004**, *306*, 666.
[8] A. K. Geim, K. S. Novoselov, *Nat. Mater.* **2007**, *6*, 183.
[9] A. K. Geim, *Science* **2009**, *324*, 1530.
[10] E. Castro, K. Novoselov, S. Morozov, N. Peres, J. dos Santos, J. Nilsson, F. Guinea, A. Geim, A. Neto, *Phys. Rev. Lett.* **2007**, *99*, 216802.
[11] B. Partoens, F. M. Peeters, *Phys. Rev. B* **2006**, *74*, 1.
[12] S. Park, R. S. Ruoff, *Nat. Nanotechnol.* **2009**, *4*, 217.
[13] D. C. Elias, R. R. Nair, T. M. G. Mohiuddin, S. V. Morozov, P. Blake, M. P. Halsall, A. C. Ferrari, D. W. Boukhvalov, M. I. Katsnelson, A. K. Geim, K. S. Novoselov, *Science* **2009**, *323*, 610.
[14] S. Zhu, Y. Song, X. Zhao, J. Shao, J. Zhang, B. Yang, *Nano Res.* **2015**, *8*, 355.
[15] L. Cao, M. J. Meziani, S. Sahu, Y.-P. Sun, *Acc. Chem. Res.* **2013**, *46*, 171.
[16] K. S. Novoselov, D. Jiang, F. Schedin, T. J. Booth, V. V Khotkevich, S. V Morozov, A. K. Geim, *Proc. Nati. Acad. Sci.* **2005**, *102*, 10451.
[17] G. R. Bhimanapati, Z. Lin, V. Meunier, Y. Jung, J. Cha, S. Das, D. Xiao, Y. Son, X. M. S. Strano, X. V. R. Cooper, O. L. Liang, S. G. Louie, E. Ringe, W. Zhou, O. S. S. Kim, R. R. Naik, B. G. Sumpter, O. H. Terrones, F. Xia, Y. Wang, J. Zhu, D. Akinwande, N.

Alem, J. A. Schuller, R. E. Schaak, Â. M. Terrones, J. A. Robinson, *ACS Nano* **2015**, *9*, 11509.
[18] R. Mas-Ballesté, C. Gómez-Navarro, J. Gómez-Herrero, F. Zamora, *Nanoscale* **2011**, *3*, 20.
[19] K. F. Mak, C. Lee, J. Hone, J. Shan, T. F. Heinz, *Phys. Rev. Lett.* **2010**, *105*, 136805.
[20] J. Yang, R. Xu, J. Pei, Y. W. Myint, F. Wang, Z. Wang, S. Zhang, Z. Yu, Y. Lu, *Light Sci. Appl.* **2015**, *4*, e312.
[21] H. Liu, Y. Du, Y. Deng, P. D. Ye, B. Ozdol, J. S. Kang, H. A. Bechtel, S. B. Desai, F. Kronast, A. A. Unal, G. Conti, C. Conlon, G. K. Palsson, M. C. Martin, A. M. Minor, C. S. Fadley, E. Yablonovitch, R. Maboudian, A. Javey, *Chem. Soc. Rev.* **2015**, *44*, 2732.
[22] L. Li, Y. Yu, G. J. Ye, Q. Ge, X. Ou, H. Wu, D. Feng, X. H. Chen, Y. Zhang, *Nat. Nanotechnol.* **2014**, *9*, 372.
[23] R. Gusmão, Z. Sofer, M. Pumera, *Angew. Chem. Int. Ed.* **2017**, *56*, 8052.
[24] M. Topsakal, E. Aktürk, S. Ciraci, *Phys. Rev. B* **2009**, *79*, 115442.
[25] L. Song, L. Ci, H. Lu, P. B. Sorokin, C. Jin, J. Ni, A. G. Kvashnin, D. G. Kvashnin, J. Lou, B. I. Yakobson, P. M. Ajayan, *Nano Lett.* **2010**, *10*, 3209.
[26] D. A. Bandurin, A. V. Tyurnina, G. L. Yu, A. Mishchenko, V. Zólyomi, S. V. Morozov, R. K. Kumar, R. V. Gorbachev, Z. R. Kudrynskyi, S. Pezzini, Z. D. Kovalyuk, U. Zeitler, K. S. Novoselov, A. Patane, L. Eaves, I. V. Grigorieva, V. I. Fal'ko, A. K. Geim, Y. Cao, *Nat. Nanotechnol.* **2016**, *12*, 223.
[27] Z. Yang, W. Jie, C. H. Mak, S. Lin, H. Lin, X. Yang, F. Yan, S. P. Lau, J. Hao, *ACS Nano* **2017**, *11*, 4225.
[28] J. E. Padilha, H. Peelaers, A. Janotti, C. G. Van De Walle, *Phys. Rev. B* **2014**, *90*, 205420.
[29] F. Withers, O. Del Pozo-Zamudio, A. Mishchenko, A. P. Rooney, A. Gholinia, K. Watanabe, T. Taniguchi, S. J. Haigh, A. K. Geim, A. I. Tartakovskii, K. S. Novoselov, *Nat. Mater.* **2015**, *14*, 301.
[30] Y. J. Zhang, T. Oka, R. Suzuki, J. T. Ye, Y. Iwasa, *Science* **2014**, *344*, 725.
[31] S. Wu, S. Buckley, J. R. Schaibley, L. Feng, J. Yan, D. G. Mandrus, F. Hatami, W. Yao, J. Vuckovic, A. Majumdar, X. Xu, *Nature* **2015**, *520*, 69.
[32] J. Shang, C. Cong, Z. Wang, N. Peimyoo, L. Wu, C. Zou, Y. Chen, X. Y. Chin, J. Wang, C. Soci, W. Huang, T. Yu, *Nat. Commun.* **2017**, *8*, 543.
[33] Y. Ye, Z. J. Wong, X. Lu, X. Ni, H. Zhu, X. Chen, Y. Wang, X. Zhang, *Nat. Photonics* **2015**, *9*, 733.
[34] C. Tan, Z. Lai, H. Zhang, *Adv. Mater.* **2017**, *29*, 1701392.
[35] R. Kurapati, K. Kostarelos, M. Prato, A. Bianco, *Adv. Mater.* **2016**, *28*, 6052.
[36] X. Huang, S. Han, W. Huang, X. Liu, *Chem. Soc. Rev.* **2013**, *42*, 173.
[37] G. Bai, M. K. Tsang, J. Hao, *Adv. Funct. Mater.* **2016**, *26*, 6330.
[38] G. Bai, M. K. Tsang, J. Hao, *Adv. Opt. Mater.* **2015**, *3*, 431.
[39] B. Zhu, X. Chen, X. Cui, *Sci. Rep.* **2015**, *5*, 9218.
[40] K. F. Mak, K. He, C. Lee, G. H. Lee, J. Hone, T. F. Heinz, J. Shan, *Nat. Mater.* **2012**, *12*, 207.
[41] M. Z. Bellus, F. Ceballos, H.-Y. Chiu, H. Zhao, *ACS Nano* **2015**, *9*, 6459.
[42] H. L. Zeng, X. D. Cui, *Chem. Soc. Rev.* **2015**, *44*, 2629.
[43] J. S. Ross, S. Wu, H. Yu, N. J. Ghimire, A. M. Jones, G. Aivazian, J. Yan, D. G. Mandrus, D. Xiao, W. Yao, X. Xu, *Nat. Commun.* **2013**, *4*, 1474.
[44] M. M. Ugeda, A. J. Bradley, S. F. Shi, F. H. Da Jornada, Y. Zhang, D. Y. Qiu, W. Ruan, S. K. Mo, Z. Hussain, Z. X. Shen, F. Wang, S. G. Louie, M. F. Crommie, *Nat. Mater.* **2014**, *13*, 1091.
[45] H. Kim, D. H. Lien, M. Amani, J. W. Ager, A. Javey, *ACS Nano* **2017**, *11*, 5179.

[46] M. Amani, P. Taheri, R. Addou, G. H. Ahn, D. Kiriya, D. H. Lien, J. W. Ager, R. M. Wallace, A. Javey, *Nano Lett.* **2016**, *16*, 2786.
[47] H. R. Gutie, N. Perea-lopez, A. Laura, A. Berkdemir, B. Wang, M. Terrones, *Nano Lett.* **2013**, *13*, 3447.
[48] Y. Kobayashi, S. Sasaki, S. Mori, H. Hibino, Z. Liu, K. Watanabe, T. Taniguchi, K. Suenaga, Y. Maniwa, Y. Miyata, *ACS Nano* **2015**, *9*, 4056.
[49] M. Okada, T. Sawazaki, K. Watanabe, T. Taniguch, H. Hibino, H. Shinohara, R. Kitaura, *ACS Nano* **2014**, *8*, 8273.
[50] T. Gokus, R. R. Nair, A. Bonetti, M. Bohmler, A. Lombardo, K. S. Novoselov, A. K. Geim, A. C. Ferrari, A. Hartschuh, *ACS Nano* **2009**, *3*, 3963.
[51] Z. Ye, T. Cao, K. O. Brien, H. Zhu, X. Yin, Y. Wang, S. G. Louie, X. Zhang, *Nature* **2014**, *513*, 214.
[52] D. J. Late, B. Liu, H. S. S. R. Matte, C. N. R. Rao, V. P. Dravid, *Adv. Funct. Mater.* **2012**, *22*, 1894.
[53] A. Bianco, H.-M. Cheng, T. Enoki, Y. Gogotsi, R. H. Hurt, N. Koratkar, T. Kyotani, M. Monthioux, C. R. Park, J. M. D. Tascon, J. Zhang, *Carbon* **2013**, *65*, 1.
[54] W. Jie, J. Hao, *Nanoscale* **2014**, *6*, 6346.
[55] Q. Bao, K. P. Loh, *ACS Nano* **2012**, *6*, 3677.
[56] Y. Zhu, S. Murali, W. Cai, X. Li, J. W. Suk, J. R. Potts, R. S. Ruoff, *Adv. Mater.* **2010**, *22*, 3906.
[57] K. S. Novoselov, Z. Jiang, Y. Zhang, S. V Morozov, H. L. Stormer, U. Zeitler, J. C. Maan, G. S. Boebinger, P. Kim, A. K. Geim, *Science* **2007**, *315*, 1379.
[58] F. Schwierz, *Nat. Nanotechnol.* **2010**, *5*, 487.
[59] S. Yuan, Z. Yang, C. Xie, F. Yan, J. Dai, S. P. Lau, H. L. W. Chan, J. Hao, *Adv. Mater.* **2016**, *28*, 10048.
[60] W. Jie, Y. Y. Hui, N. Y. Chan, Y. Zhang, S. P. Lau, J. Hao, *J. Phys. Chem. C* **2013**, *117*, 13747.
[61] W. Jie, Y. Y. Hui, Y. Zhang, S. P. Lau, J. Hao, *Appl. Phys. Lett.* **2013**, *102*, 223112.
[62] W. Jie, F. Zheng, J. Hao, *Appl. Phys. Lett.* **2013**, *103*, 233111.
[63] G. Eda, M. Chhowalla, *Adv. Mater.* **2010**, *22*, 2392.
[64] A. Bagri, C. Mattevi, M. Acik, Y. J. Chabal, M. Chhowalla, V. B. Shenoy, *Nat. Chem.* **2010**, *2*, 581.
[65] C. T. Chien, S. S. Li, W. J. Lai, Y. C. Yeh, H. A. Chen, I. S. Chen, L. C. Chen, K. H. Chen, T. Nemoto, S. Isoda, M. Chen, T. Fujita, G. Eda, H. Yamaguchi, M. Chhowalla, C. W. Chen, *Angew. Chem. Int. Ed.* **2012**, *51*, 6662.
[66] G. Eda, Y. Y. Lin, C. Mattevi, H. Yamaguchi, H. A. Chen, I. S. Chen, C. W. Chen, M. Chhowalla, *Adv. Mater.* **2010**, *22*, 505.
[67] A. Neogi, S. Karna, R. Shah, U. Phillipose, J. Perez, R. Shimada, Z. M. Wang, *Nanoscale* **2014**, *6*, 11310.
[68] Z. Gan, S. Xiong, X. Wu, T. Xu, X. Zhu, X. Gan, J. Guo, J. Shen, L. Sun, P. K. Chu, *Adv. Opt. Mater.* **2013**, *1*, 926.
[69] S. K. Pal, *Carbon* **2015**, *88*, 86.
[70] Q. Quan, X. Lin, N. Zhang, Y.-J. Xu, *Nanoscale* **2017**, *9*, 2398.
[71] Y. W. Son, M. L. Cohen, S. G. Louie, *Phys. Rev. Lett.* **2006**, *97*, 216803.
[72] L. Yang, M. L. Cohen, S. G. Louie, *Nano Lett.* **2007**, *7*, 3112.
[73] V. Barone, O. Hod, G. E. Scuseria, *Nano Lett.* **2006**, *6*, 2748.
[74] K. Nakada, M. Fujita, G. Dresselhaus, M. S. Dresselhaus, *Phys. Rev. B* **1996**, *54*, 17954.
[75] M. Han, B. Özyilmaz, Y. Zhang, P. Kim, *Phys. Rev. Lett.* **2007**, *98*, 206805.
[76] M. Y. Han, B. Oezyilmaz, Y. Zhang, P. Kim, *Phys. Rev. Lett.* **2007**, *98*, 7.
[77] P. Wagner, C. P. Ewels, J.-J. Adjizian, L. Magaud, P. Pochet, S. Roche, A. Lopez-Bezanilla, V. V. Ivanovskaya, A. Yaya, M. Rayson, P. Briddon, B. Humbert, *J. Phys.*

Chem. C **2013**, *117*, 26790.
[78] X. Yang, X. Dou, A. Rouhanipour, L. Zhi, H. J. Räder, K. Müllen, *J. Am. Chem. Soc.* **2008**, *130*, 4216.
[79] X. Li, X. Wang, L. Zhang, S. Lee, H. Dai, *Science* **2008**, *319*, 1229.
[80] M. J. Jaison, T. N. Narayanan, T. Prem Kumar, V. K. Pillai, *J. Mater. Chem. A* **2015**, *3*, 18222.
[81] J. Wang, L. Ma, Q. Yuan, L. Zhu, F. Ding, *Angew. Chem. Int. Ed.* **2011**, *50*, 8041.
[82] J. Cai, C. A. Pignedoli, L. Talirz, P. Ruffieux, H. Söde, L. Liang, V. Meunier, R. Berger, R. Li, X. Feng, K. Müllen, R. Fasel, *Nat. Nanotechnol.* **2014**, *9*, 896.
[83] C. Q. Qu, C. Y. Wang, L. Qiao, S. S. Yu, H. B. Li, *Chem. Phys. Lett.* **2013**, *578*, 97.
[84] D. V. Kosynkin, A. L. Higginbotham, A. Sinitskii, J. R. Lomeda, A. Dimiev, B. K. Price, J. M. Tour, *Nature* **2009**, *458*, 872.
[85] L. Jiao, L. Zhang, X. Wang, G. Diankov, H. Dai, *Nature* **2009**, *458*, 877.
[86] J. Cai, P. Ruffieux, R. Jaafar, M. Bieri, T. Braun, S. Blankenburg, M. Muoth, A. P. Seitsonen, M. Saleh, X. Feng, K. Müllen, R. Fasel, *Nature* **2010**, *466*, 470.
[87] Y.-Z. Tan, B. Yang, K. Parvez, A. Narita, S. Osella, D. Beljonne, X. Feng, K. Müllen, *Nat. Commun.* **2013**, *4*, DOI: 10.1038/ncomms3646.
[88] P. Ruffieux, J. Cai, N. C. Plumb, L. Patthey, D. Prezzi, A. Ferretti, E. Molinari, X. Feng, K. Müllen, C. A. Pignedoli, R. Fasel, *ACS Nano* **2012**, *6*, 6930.
[89] K. a. Simonov, N. a. Vinogradov, A. S. Vinogradov, A. V. Generalov, E. M. Zagrebina, G. I. Svirskiy, A. a. Cafolla, T. Carpy, J. P. Cunniffe, T. Taketsugu, A. Lyalin, N. Martensson, A. B. Preobrajenski, *ACS Nano* **2015**, *9*, 8997.
[90] K. A. Simonov, N. A. Vinogradov, A. S. Vinogradov, A. V. Generalov, E. M. Zagrebina, N. Mårtensson, A. A. Cafolla, T. Carpy, J. P. Cunniffe, A. B. Preobrajenski, *J. Phys. Chem. C* **2014**, *118*, 12532.
[91] R. Denk, M. Hohage, P. Zeppenfeld, J. Cai, C. A. Pignedoli, H. Söde, R. Fasel, X. Feng, K. Müllen, S. Wang, D. Prezzi, A. Ferretti, A. Ruini, E. Molinari, P. Ruffieux, *Nat. Commun.* **2014**, *5*, 4253.
[92] Y. Huang, Y. Mai, U. Beser, J. Teyssandier, G. Velpula, H. Van Gorp, L. A. Straasø, M. R. Hansen, D. Rizzo, C. Casiraghi, R. Yang, G. Zhang, D. Wu, F. Zhang, D. Yan, S. De Feyter, K. Müllen, X. Feng, *J. Am. Chem. Soc.* **2016**, *138*, 10136.
[93] S. Zhao, L. Rondin, G. Delport, C. Voisin, U. Beser, Y. Hu, X. Feng, K. Müllen, A. Narita, S. Campidelli, J. S. Lauret, *Carbon* **2017**, *119*, 235.
[94] B. V. Senkovskiy, M. Pfeiffer, S. K. Alavi, A. Bliesener, J. Zhu, S. Michel, A. V. Fedorov, R. German, D. Hertel, D. Haberer, L. Petaccia, F. R. Fischer, K. Meerholz, P. H. M. Van Loosdrecht, K. Lindfors, A. Grüneis, *Nano Lett.* **2017**, *17*, 4029.
[95] A. Nourbakhsh, M. Cantoro, T. Vosch, G. Pourtois, F. Clemente, M. H. van der Veen, J. Hofkens, M. M. Heyns, S. De Gendt, B. F. Sels, *Nanotechnology* **2010**, *21*, 435203.
[96] A. Nourbakhsh, M. Cantoro, A. V. Klekachev, G. Pourtois, T. Vosch, J. Hofkens, M. H. Van Der Veen, M. M. Heyns, S. De Gendt, B. F. Sels, *J. Phys. Chem. C* **2011**, *115*, 16619.
[97] W. Jie, Z. Yang, F. Zhang, G. Bai, C. W. Leung, J. Hao, *ACS Nano* **2017**, *11*, 6950.
[98] X. Huang, Z. Zeng, H. Zhang, *Chem. Soc. Rev.* **2013**, *42*, 1934.
[99] A. Splendiani, L. Sun, Y. Zhang, T. Li, J. Kim, C. Y. Chim, G. Galli, F. Wang, *Nano Lett.* **2010**, *10*, 1271.
[100] W. Zhao, Z. Ghorannevis, L. Chu, M. Toh, C. Kloc, P.-H. Tan, G. Eda, *ACS Nano* **2013**, *7*, 791.
[101] H. Wang, C. Zhang, F. Rana, *Nano Lett.* **2015**, *15*, 339.
[102] H. V. Han, A. Y. Lu, L. S. Lu, J. K. Huang, H. Li, C. L. Hsu, Y. C. Lin, M. H. Chiu, K. Suenaga, C. W. Chu, H. C. Kuo, W. H. Chang, L. J. Li, Y. Shi, *ACS Nano* **2016**, *10*, 1454.

[103] B. G. Jeong, Y. S. Park, J. H. Chang, I. Cho, J. K. Kim, H. Kim, K. Char, J. Cho, V. I. Klimov, P. Park, D. C. Lee, W. K. Bae, *ACS Nano* **2016**, *10*, 9297.
[104] M. S. Kim, G. Nam, S. Park, H. Kim, G. H. Han, J. Lee, K. P. Dhakal, J.-Y. Leem, Y. H. Lee, J. Kim, *Thin Solid Films* **2015**, *590*, 318.
[105] Y. Li, Z. Qi, M. Liu, Y. Wang, X. Cheng, G. Zhang, L. Sheng, *Nanoscale* **2014**, *6*, 15248.
[106] S. Mouri, Y. Miyauchi, K. Matsuda, *Nano Lett.* **2013**, *13*, 5944.
[107] Q. Wang, S. Ge, X. Li, J. Qiu, Y. Ji, J. Feng, D. Sun, *ACS Nano* **2013**, *7*, 11087.
[108] H. Fang, M. Tosun, G. Seol, T. C. Chang, K. Takei, J. Guo, A. Javey, *Nano Lett.* **2013**, *13*, 1991.
[109] H. Li, G. Lu, Y. Wang, Z. Yin, C. Cong, Q. He, L. Wang, F. Ding, T. Yu, H. Zhang, *Small* **2013**, *9*, 1974.
[110] N. Perea-Lõpez, A. L. Elías, A. Berkdemir, A. Castro-Beltran, H. R. Gutiérrez, S. Feng, R. Lv, T. Hayashi, F. Lõpez-Urías, S. Ghosh, B. Muchharla, S. Talapatra, H. Terrones, M. Terrones, *Adv. Funct. Mater.* **2013**, *23*, 5511.
[111] H. S. S. Ramakrishna Matte, A. Gomathi, A. K. Manna, D. J. Late, R. Datta, S. K. Pati, C. N. R. Rao, *Angew. Chem. Int. Ed.* **2010**, *49*, 4059.
[112] Q. H. Wang, K. Kalantar-Zadeh, A. Kis, J. N. Coleman, M. S. Strano, *Nat. Nanotechnol.* **2012**, *7*, 699.
[113] L. Yuan, L. Huang, *Nanoscale* **2015**, *7*, 7402.
[114] W. Sik Hwang, M. Remskar, R. Yan, V. Protasenko, K. Tahy, S. Doo Chae, P. Zhao, A. Konar, H. Xing, A. Seabaugh, D. Jena, *Appl. Phys. Lett.* **2012**, *101*, 13107.
[115] V. Podzorov, M. E. Gershenson, C. Kloc, R. Zeis, E. Bucher, *Appl. Phys. Lett.* **2004**, *84*, 3301.
[116] H. Fang, S. Chuang, T. C. Chang, K. Takei, T. Takahashi, A. Javey, *Nano Lett.* **2012**, *12*, 3788.
[117] D. Braga, I. Gutiérrez Lezama, H. Berger, A. F. Morpurgo, *Nano Lett.* **2012**, *12*, 5218.
[118] Y. You, X. X. Zhang, T. C. Berkelbach, M. S. Hybertsen, D. R. Reichman, T. F. Heinz, *Nat. Phys.* **2015**, *11*, 477.
[119] Y. Li, X. Li, H. Chen, J. Shi, Q. Shang, S. Zhang, X. Qiu, Z. Liu, Q. Zhang, H. Xu, W. Liu, X. Liu, Y. Liu, *ACS Appl. Mater. Interfaces* **2017**, *9*, 27402.
[120] P. Rastogi, S. Kumar, S. Bhowmick, A. Agarwal, Y. S. Chauhan, *J. Phys. Chem. C* **2014**, *118*, 30309.
[121] J. Shang, X. Shen, C. Cong, N. Peimyoo, B. Cao, M. Eginligil, T. Yu, *ACS Nano* **2015**, *9*, 647.
[122] M. Amani, D. Lien, D. Kiriya, J. Xiao, A. Azcatl, J. Noh, S. R. Madhvapathy, R. Addou, S. Kc, M. Dubey, K. Cho, R. M. Wallace, S. Lee, J. He, J. W. A. Iii, X. Zhang, E. Yablonovitch, A. Javey, *Science* **2015**, *350*, 1065.
[123] N. Peimyoo, W. Yang, J. Shang, X. Shen, Y. Wang, T. Yu, *ACS Nano* **2014**, *8*, 11320.
[124] S. Tongay, J. Zhou, C. Ataca, J. Liu, J. S. Kang, T. S. Matthews, L. You, J. B. Li, J. C. Grossman, J. Q. Wu, *Nano Lett* **2013**, *13*, 2831.
[125] Y. Li, J. Ludwig, T. Low, A. Chernikov, X. Cui, G. Arefe, Y. D. Kim, A. M. Van Der Zande, A. Rigosi, H. M. Hill, S. H. Kim, J. Hone, Z. Li, D. Smirnov, T. F. Heinz, *Phys. Rev. Lett.* **2014**, *113*, 266804.
[126] A. Srivastava, M. Sidler, A. V. Allain, D. S. Lembke, A. Kis, A. Imamollu, *Nat. Phys.* **2015**, *11*, 141.
[127] G. Aivazian, Z. Gong, A. M. Jones, R. L. Chu, J. Yan, D. G. Mandrus, C. Zhang, D. Cobden, W. Yao, X. Xu, *Nat. Phys.* **2015**, *11*, 148.
[128] H. J. Conley, B. Wang, J. I. Ziegler, R. F. Haglund, S. T. Pantelides, K. I. Bolotin, *Nano Lett.* **2013**, *13*, 3626.
[129] Y. Wang, C. Cong, W. Yang, J. Shang, N. Peimyoo, Y. Chen, J. Kang, J. Wang, W.

Huang, T. Yu, *Nano Res.* **2015**, *8*, 2562.
[130] Y. Y. Hui, X. Liu, W. Jie, N. Y. Chan, J. Hao, Y.-T. Hsu, L.-J. Li, W. Guo, S. P. Lau, *ACS Nano* **2013**, *7*, 7126.
[131] Y. C. Lin, D. O. Dumcenco, H. P. Komsa, Y. Niimi, A. V. Krasheninnikov, Y. S. Huang, K. Suenaga, *Adv. Mater.* **2014**, *26*, 2857.
[132] Z. Wu, G. Bai, Y. Qu, D. Guo, L. Li, P. Li, J. Hao, W. Tang, *Appl. Phys. Lett.* **2016**, *108*, 1.
[133] V. P. Pham, G. Y. Yeom, *Adv. Mater.* **2016**, *28*, 9024.
[134] A. W. Robertson, Y. C. Lin, S. Wang, H. Sawada, C. S. Allen, Q. Chen, S. Lee, G. Do Lee, J. Lee, S. Han, E. Yoon, A. I. Kirkland, H. Kim, K. Suenaga, J. H. Warner, *ACS Nano* **2016**, *10*, 10227.
[135] Q. Sun, L. Yadgarov, R. Rosentsveig, G. Seifert, R. Tenne, J. L. Musfeldt, *ACS Nano* **2012**, *2*, 1.
[136] K. Zhang, S. Feng, J. Wang, A. Azcatl, N. Lu, R. Addou, N. Wang, C. Zhou, J. Lerach, V. Bojan, M. J. Kim, L. Q. Chen, R. M. Wallace, M. Terrones, J. Zhu, J. A. Robinson, *Nano Lett.* **2015**, *15*, 6586.
[137] J. Gao, Y. D. Kim, L. Liang, J. C. Idrobo, P. Chow, J. Tan, B. Li, L. Li, B. G. Sumpter, T. M. Lu, V. Meunier, J. Hone, N. Koratkar, *Adv. Mater.* **2016**, *28*, 9735.
[138] K. P. Dhakal, D. L. Duong, J. Lee, H. Nam, M. Kim, M. Kan, Y. H. Lee, J. Kim, *Nanoscale* **2014**, *6*, 13028.
[139] G. Bai, S. Yuan, Y. Zhao, Z. Yang, S. Y. Choi, Y. Chai, S. F. Yu, S. P. Lau, J. Hao, *Adv. Mater.* **2016**, *28*, 7472.
[140] H. Li, Q. Zhang, X. Duan, X. Wu, X. Fan, X. Zhu, X. Zhuang, W. Hu, H. Zhou, A. Pan, X. Duan, *J. Am. Chem. Soc.* **2015**, *137*, 5284.
[141] X. Duan, C. Wang, Z. Fan, G. Hao, L. Kou, U. Halim, H. Li, X. Wu, Y. Wang, J. Jiang, A. Pan, Y. Huang, R. Yu, X. Duan, *Nano Lett.* **2016**, *16*, 264.
[142] H. Li, X. Wu, H. Liu, B. Zheng, Q. Zhang, X. Zhu, Z. Wei, X. Zhuang, H. Zhou, W. Tang, X. Duan, A. Pan, *ACS Nano* **2017**, *11*, 961.
[143] M. Z. Bellus, Z. Yang, J. Hao, S. P. Lau, H. Zhao, *2D Mater.* **2017**, *4*, 25063.
[144] V. Eswaraiah, Q. Zeng, Y. Long, Z. Liu, *Small* **2016**, *12*, 3480.
[145] A. Castellanos-Gomez, *J. Phys. Chem. Lett.* **2015**, *6*, 4280.
[146] S. Zhang, J. Yang, R. Xu, F. Wang, W. Li, M. Ghufran, Y. W. Zhang, Z. Yu, G. Zhang, Q. Qin, Y. Lu, *ACS Nano* **2014**, *8*, 9590.
[147] S. Ge, L. Zhang, P. Wang, Y. Fang, *Sci. Rep.* **2016**, *6*, 27307.
[148] Z. Yang, J. Hao, S. Yuan, S. Lin, H. M. Yau, J. Dai, S. P. Lau, *Adv. Mater.* **2015**, *27*, 3748.
[149] V. Tran, R. Soklaski, Y. Liang, L. Yang, *Phys. Rev. B* **2014**, *89*, 1.
[150] P. D. Ye, H. Liu, A. T. Neal, Z. Zhu, Z. Luo, X. Xu, C. Engineering, W. Lafayette, U. States, E. Lansing, U. States, M. Engineering, W. Lafayette, U. States, *ACS Nano* **2014**, *8*, 4033.
[151] X. Wang, A. M. Jones, K. L. Seyler, V. Tran, Y. Jia, H. Zhao, H. Wang, L. Yang, X. Xu, F. Xia, *Nat. Nanotechnol.* **2015**, *10*, 517.
[152] Z. Li, Y. Xiao, Y. Gong, Z. Wang, Y. Kang, S. Zu, P. M. Ajayan, P. Nordlander, Z. Fang, *ACS Nano* **2015**, *9*, 10158.
[153] R. Xu, S. Zhang, F. Wang, J. Yang, Z. Wang, J. Pei, Y. W. Myint, B. Xing, Z. Yu, L. Fu, Q. Qin, Y. Lu, *ACS Nano* **2016**, *10*, 2046.
[154] K. F. Mak, K. He, C. Lee, G. H. Lee, J. Hone, T. F. Heinz, J. Shan, *Nat. Mater.* **2012**, *12*, 207.
[155] T. Hertel, S. Himmelein, T. Ackermann, D. Stich, J. C. K, *ACS Nano* **2010**, *4*, 7161.
[156] Y. Miyauchi, M. Iwamura, S. Mouri, T. Kawazoe, M. Ohtsu, K. Matsuda, *Nat. Photonics* **2013**, *7*, 715.

[157] S. Ghosh, S. M. Bachilo, R. A. Simonette, K. M. Beckingham, R. B. Weisman, *Science* **2010**, *330*, 1656.
[158] R. Xu, J. Yang, Y. W. Myint, J. Pei, H. Yan, F. Wang, Y. Lu, *Adv. Mater.* **2016**, *28*, 3493.
[159] W. Huang, L. Gan, H. Li, Y. Ma, T. Zhai, *CrystEngComm* **2016**, *18*, 3968.
[160] W. Jie, W. Jie, J. Hao, in Advanced 2D Materials. Vol. 1 (Eds: A. Tiwari, M. Syvajarvi), John Wiley & Sons, Hoboken, NJ, USA, 2016, Ch. 1.
[161] W. Feng, W. Zheng, W. Cao, P. Hu, *Adv. Mater.* **2014**, *26*, 6587.
[162] G. W. Mudd, S. A. Svatek, T. Ren, A. Patanè, O. Makarovsky, L. Eaves, P. H. Beton, Z. D. Kovalyuk, G. V. Lashkarev, Z. R. Kudrynskyi, A. I. Dmitriev, *Adv. Mater.* **2013**, *25*, 5714.
[163] C. H. Ho, Y. J. Chu, *Adv. Opt. Mater.* **2015**, *3*, 1750.
[164] G. W. Mudd, M. R. Molas, X. Chen, V. Zólyomi, K. Nogajewski, Z. R. Kudrynskyi, Z. D. Kovalyuk, G. Yusa, 0. Makarovsky, L. Eaves, M. Potemski, V. I. Fal'ko, A. Patane, *Sci. Rep.* **2016**, *6*, 39619.
[165] D. Geng, H. Wang, G. Yu, *Adv. Mater.* **2015**, *27*, 2821.
[166] W. Bao, F. Miao, Z. Chen, H. Zhang, W. Jang, C. Dames, C. N. Lau, *Nat. Nanotechnol.* **2009**, *4*, 562.
[167] M. Brotons-Gisbert, D. Andres-Penares, J. Suh, F. Hidalgo, R. Abargues, P. J. Rodriguez-Canto, A. Segura, A. Cros, G. Tobias, E. Canadell, *Nano Lett.* **2016**, *16*, 3221.
[168] K. S. Novoselov, A. Mishchenko, A. Carvalho, A. H. Castro Neto, *Science* **2016**, *353*, aac9439.
[169] J. S. Ross, P. Klement, A. M. Jones, N. J. Ghimire, J. Yan, D. G. Mandrus, T. Taniguchi, K. Watanabe, K. Kitamura, W. Yao, D. H. Cobden, X. Xu, *Nat. Nanotechnol.* **2014**, *9*, 268.
[170] D. Jariwala, T. J. Marks, M. C. Hersam, *Nat. Mater.* **2016**, *16*, 170.
[171] L. Wang, *Science* **2013**, *342*, 614.
[172] M. M. Furchi, A. Pospischil, F. Libisch, J. Burgd??rfer, T. Mueller, *Nano Lett.* **2014**, *14*, 4785.
[173] Z. Ji, H. Hong, J. Zhang, Q. Zhang, W. Huang, T. Cao, R. Qiao, C. Liu, J. Liang, C. Jin, L. Jiao, K. Shi, S. Meng, K. Liu, *ACS Nano* **2017**, *11*, 12020.
[174] X. Hong, J. Kim, S.-F. Shi, Y. Zhang, C. Jin, Y. Sun, S. Tongay, J. Wu, Y. Zhang, F. Wang, *Nat. Nanotechnol.* **2014**, *9*, 682.
[175] H. Zhu, J. Wang, Z. Gong, Y. D. Kim, J. Hone, X. Y. Zhu, *Nano Lett.* **2017**, *17*, 3591.
[176] F. Ceballos, M. Z. Bellus, H. Y. Chiu, H. Zhao, *ACS Nano* **2014**, *8*, 12717.
[177] P. Rivera, J. R. Schaibley, A. M. Jones, J. S. Ross, S. Wu, G. Aivazian, P. Klement, K. Seyler, G. Clark, N. J. Ghimire, J. Yan, D. G. Mandrus, W. Yao, X. Xu, *Nat. Commun.* **2015**, *6*, 6242.
[178] K. Liu, L. Zhang, T. Cao, C. Jin, D. Qiu, Q. Zhou, A. Zettl, P. Yang, S. G. Louie, F. Wang, *Nat. Commun.* **2014**, *5*, 4966.
[179] K. Wang, B. Huang, M. Tian, F. Ceballos, M.-W. Lin, M. Mahjouri-Samani, A. Boulesbaa, A. A. Puretzky, C. M. Rouleau, M. Yoon, H. Zhao, K. Xiao, G. Duscher, D. B. Geohegan, *ACS Nano* **2016**, *10*, 6612.
[180] C. Huang, S. Wu, A. M. Sanchez, J. J. P. Peters, R. Beanland, J. S. Ross, P. Rivera, W. Yao, D. H. Cobden, X. Xu, *Nat. Mater.* **2014**, *13*, 1096.
[181] M.-Y. Li, Y. Shi, C.-C. Cheng, L.-S. Lu, Y.-C. Lin, H.-L. Tang, M.-L. Tsai, C.-W. Chu, K.-H. Wei, J.-H. He, W.-H. Chang, K. Suenaga, L.-J. Li, *Science* **2015**, *349*, 524.
[182] X. Duan, C. Wang, J. C. Shaw, R. Cheng, Y. Chen, H. Li, X. Wu, Y. Tang, Q. Zhang, A. Pan, J. Jiang, R. Yu, Y. Huang, X. Duan, *Nat. Nanotechnol.* **2014**, *9*, 1024.
[183] P. Rivera, J. R. Schaibley, A. M. Jones, J. S. Ross, S. Wu, G. Aivazian, P. Klement, K.

Seyler, G. Clark, N. J. Ghimire, J. Yan, D. G. Mandrus, W. Yao, X. Xu, *Nat. Commun.* **2015**, *6*, 6242.
[184] M. Mahjouri-Samani, M.-W. Lin, K. Wang, A. R. Lupini, J. Lee, L. Basile, A. Boulesbaa, C. M. Rouleau, A. A. Puretzky, I. N. Ivanov, K. Xiao, M. Yoon, D. B. Geohegan, *Nat. Commun.* **2015**, *6*, 7749.
[185] R. S. Sundaram, M. Engel, A. Lombardo, R. Krupke, A. C. Ferrari, P. Avouris, M. Steiner, *Nano Lett.* **2013**, *13*, 1416.
[186] A. Pospischil, M. M. Furchi, T. Mueller, *Nat. Nanotechnol.* **2014**, *9*, 257.
[187] B. W. H. Baugher, H. O. H. Churchill, Y. Yang, P. Jarillo-Herrero, *Nat. Nanotechnol.* **2014**, *9*, 262.
[188] H. Zeng, J. Dai, W. Yao, D. Xiao, X. Cui, *Nat. Nanotechnol.* **2012**, *7*, 490.
[189] K. F. Mak, K. He, J. Shan, T. F. Heinz, *Nat. Nanotechnol.* **2012**, *7*, 494.
[190] A. M. Jones, H. Yu, N. J. Ghimire, S. Wu, G. Aivazian, J. S. Ross, B. Zhao, J. Yan, D. G. Mandrus, D. Xiao, W. Yao, X. Xu, *Nat. Nanotechnol.* **2013**, *8*, 634.
[191] S. Wu, J. S. Ross, G.-B. Liu, G. Aivazian, A. Jones, Z. Fei, W. Zhu, D. Xiao, W. Yao, D. Cobden, X. Xu, *Nat. Phys.* **2013**, *9*, 149.
[192] D. Li, R. Cheng, H. Zhou, C. Wang, A. Yin, Y. Chen, N. O. Weiss, Y. Huang, X. Duan, *Nat. Commun.* **2015**, *6*, 7509.
[193] W. Yang, J. Shang, J. Wang, X. Shen, B. Cao, N. Peimyoo, C. Zou, Y. Chen, Y. Wang, C. Cong, W. Huang, T. Yu, *Nano Lett.* **2016**, *16*, 1560.
[194] O. Lopez-Sanchez, E. Alarcon Llado, V. Koman, A. Fontcuberta I Morral, A. Radenovic, A. Kis, *ACS Nano* **2014**, *8*, 3042.
[195] R. Cheng, D. Li, H. Zhou, C. Wang, A. Yin, S. Jiang, Y. Liu, Y. Chen, Y. Huang, X. Duan, *Nano Lett.* **2014**, *14*, 5590.
[196] L. Britnell, R. M. Ribeiro, A. Eckmann, R. Jalil, B. D. Belle, A. Mishchenko, Y. Kim, R. V Gorbachev, T. Georgiou, S. V Morozov, A. N. Grigorenko, A. K. Geim, C. Casiraghi, A. H. C. Neto, K. S. Novoselov, **2013**, *340*, 1311.
[197] N. Balakrishnan, Z. R. Kudrynskyi, M. W. Fay, G. W. Mudd, S. A. Svatek, O. Makarovsky, Z. D. Kovalyuk, L. Eaves, P. H. Beton, A. Patanè, *Adv. Opt. Mater.* **2014**, *2*, 1064.
[198] E. Hendry, P. J. Hale, J. Moger, A. K. Savchenko, S. A. Mikhailov, *Phys. Rev. Lett.* **2010**, *105*, 97401.
[199] Y. Wang, M. Tokman, A. Belyanin, *Phys. Rev. B* **2016**, *94*, 195422.
[200] R. Wu, Y. Zhang, S. Yan, F. Bian, W. Wang, X. Bai, X. Lu, J. Zhao, E. Wang, *Nano Lett.* **2011**, *11*, 5159.
[201] J. Wang, Y. Hernandez, M. Lotya, J. N. Coleman, W. J. Blau, *Adv. Mater.* **2009**, *21*, 2430.
[202] W. T. Liu, S. W. Wu, P. J. Schuck, M. Salmeron, Y. R. Shen, F. Wang, *Phys. Rev. B* **2010**, *82*, 081408(R).
[203] C. H. Lui, K. F. Mak, J. Shan, T. F. Heinz, *Phys. Rev. Lett.* **2010**, *105*, 127404.
[204] H. Zeng, X. Cui, *Chem. Soc. Rev.* **2015**, *44*, 2629.
[205] K. Wang, J. Wang, J. Fan, M. Lotya, A. Neill, D. Fox, Y. Feng, X. Zhang, B. Jiang, Q. Zhao, H. Zhang, J. N. Coleman, L. Zhang, W. J. Blau, *ACS Nano* **2013**, *7*, 9260.
[206] K. R. Allakhverdiev, T. Baykara, S. Joosten, E. Günay, A. A. Kaya, A. Kulibekov (Gulubayov), A. Seilmeier, E. Y. Salaev, *Opt. Commun.* **2006**, *261*, 60.
[207] I. B. Zotova, Y. J. Ding, *Appl. Opt.* **2001**, *40*, 6654.
[208] S. Lei, L. Ge, Z. Liu, S. Najmaei, G. Shi, G. You, J. Lou, R. Vajtai, P. M. Ajayan, *Nano Lett.* **2013**, *13*, 2777.
[209] P. Hu, Z. Wen, L. Wang, P. Tan, K. Xiao, *ACS Nano* **2012**, *6*, 5988.
[210] P. Hu, L. Wang, M. Yoon, J. Zhang, W. Feng, X. Wang, Z. Wen, J. C. Idrobo, Y. Miyamoto, D. B. Geohegan, K. Xiao, *Nano Lett.* **2013**, *13*, 1649.

[211] D. J. Late, B. Liu, J. Luo, A. Yan, H. S. S. R. Matte, M. Grayson, C. N. R. Rao, V. P. Dravid, *Adv. Mater.* **2012**, *24*, 3549.
[212] L. Karvonen, A. Säynätjoki, S. Mehravar, R. D. Rodriguez, S. Hartmann, D. R. T. Zahn, S. Honkanen, R. a. Norwood, N. Peyghambarian, K. Kieu, H. Lipsanen, J. Riikonen, *Sci. Rep.* **2015**, *5*, 10334.
[213] W. Jie, X. Chen, D. Li, L. Xie, Y. Y. Hui, S. P. Lau, X. Cui, J. Hao, *Angew. Chem. Int. ed.* **2015**, *54*, 1185.
[214] X. Zhou, J. Cheng, Y. Zhou, T. Cao, H. Hong, Z. Liao, S. Wu, H. Peng, K. Liu, D. Yu, *J. Am. Chem. Soc.* **2015**, *137*, 7994.
[215] H. Zeng, G.-B. Liu, J. Dai, Y. Yan, B. Zhu, R. He, L. Xie, S. Xu, X. Chen, W. Yao, X. Cui, *Sci. Rep.* **2013**, *3*, 1608.
[216] W. Hsu, Z. Zhao, L. Li, C. Chen, *ACS Nano* **2014**, *8*, 2951.
[217] N. Kumar, S. Najmaei, Q. Cui, F. Ceballos, P. Ajayan, J. Lou, H. Zhao, *Phys. Rev. B* **2013**, *87*, 161403.
[218] L. M. Malard, T. V. Alencar, A. P. M. Barboza, K. F. Mak, A. M. de Paula, *Phys. Rev. B* **2013**, *87*, 201401.
[219] Y. Li, Y. Rao, K. F. Mak, Y. You, S. Wang, C. R. Dean, T. F. Heinz, *Nano Lett.* **2013**, *13*, 3329.
[220] C.-J. Kim, L. Brown, M. W. Graham, R. Hovden, R. W. Havener, P. L. McEuen, D. A. Muller, J. Park, *Nano Lett.* **2013**, *13*, 5660.
[221] G. Wang, X. Marie, I. Gerber, T. Amand, D. Lagarde, L. Bouet, M. Vidal, A. Balocchi, B. Urbaszek, *Phys. Rev. Lett.* **2015**, *114*, 97403.
[222] N. Kumar, J. Kumar, C. Gerstenkorn, R. Wang, H. Y. Chiu, A. L. Smirl, H. Zhao, *Phys. Rev. B* **2013**, *87*, 121406(R).
[223] R. Wang, H. C. Chien, J. Kumar, N. Kumar, H. Y. Chiu, H. Zhao, *ACS Appl. Mater. Interfaces* **2014**, *6*, 314.
[224] X. Wang, F. Xia, *Nat. Mater.* **2015**, *14*, 2.
[225] K. F. Mak, J. Shan, *Nat. Photonics* **2016**, *10*, 216.
[226] S. Jo, N. Ubrig, H. Berger, A. B. Kuzmenko, A. F. Morpurgo, *Nano Lett.* **2014**, *14*, 2019.
[227] Y. He, G. Clark, J. R. Schaibley, Y. He, M. Chen, Y. Wei, X. Ding, Q. Zhang, W. Yao, X. Xu, C.-Y. Lu, J.-W. Pan, *Nat. Nanotechnol.* **2015**, *10*, 497.
[228] A. Srivastava, M. Sidler, A. V. Allain, D. S. Lembke, A. Kis, A. Imamoglu, *Nat. Nanotechnol.* **2015**, *10*, 491.
[229] M. Koperski, K. Nogajewski, A. Arora, V. Cherkez, P. Mallet, J. Y. Veuillen, J. Marcus, P. Kossacki, M. Potemski, *Nat. Nanotechnol.* **2015**, *10*, 503.
[230] I. Aharonovich, M. Toth, *Science* **2017**, *358*, 170.
[231] V. Perebeinos, *Nat. Nanotechnol.* **2015**, *10*, 485.
[232] T.-H. Han, Y. Lee, M.-R. Choi, S.-H. Woo, S.-H. Bae, B. H. Hong, J.-H. Ahn, T.-W. Lee, *Nat. Photonics* **2012**, *6*, 105.
[233] W. Jie, J. Hao, *Nanoscale* **2018**, *10*, 328.
[234] G. Ni, Y. Zheng, S. Bae, C. Tan, 0. Kahya, J. Wu, B. H. Hong, K. Yao, B. Ozyilmaz, *ACS Nano* **2012**, *6*, 3935.
[235] S.-H. Bae, O. Kahya, B. K. Sharma, J. Kwon, H. J. Cho, B. Ozyilmaz, J.-H. Ahn, *ACS Nano* **2013**, *7*, 3130.
[236] M.-K. Tsang, Y.-T. Wong, J. Hao, *Small Methods* **2017**, *2*, 1700265.
[237] Y. Li, X. Li, Z. Xue, M. Jiang, S. Zeng, J. Hao, *Adv. Healthc. Mater.* **2017**, *6*, 1601231.
[238] M. K. Tsang, W. Ye, G. Wang, J. Li, M. Yang, J. Hao, *ACS Nano* **2016**, *10*, 598.
[239] Z. Yi, X. Li, Z. Xue, X. Liang, W. Lu, H. Peng, H. Liu, S. Zeng, J. Hao, *Adv. Funct. Mater.* **2015**, *25*, 7119.
[240] K. P. Loh, Q. Bao, G. Eda, M. Chhowalla, *Nat. Chem.* **2010**, *2*, 1015.

[241] D. Chimene, D. L. Alge, A. K. Gaharwar, *Adv. Mater.* **2015**, *27*, 7261.
[242] H. Zhu, Z. Lai, Y. Fang, X. Zhen, C. Tan, X. Qi, D. Ding, P. Chen, H. Zhang, K. Pu, *Small* **2017**, *13*, 1.
[243] L. Cheng, C. Yuan, S. Shen, X. Yi, H. Gong, K. Yang, Z. Liu, *ACS Nano* **2015**, *9*, 11090.
[244] Y. Zhang, B. Zheng, C. Zhu, X. Zhang, C. Tan, H. Li, B. Chen, J. Yang, J. Chen, Y. Huang, L. Wang, H. Zhang, *Adv. Mater.* **2015**, *27*, 935.
[245] C. Zhu, Z. Zeng, H. Li, F. Li, C. Fan, H. Zhang, *J. Am. Chem. Soc.* **2013**, *135*, 5998.
[246] B. Liu, C. Li, G. Chen, B. Liu, X. Deng, Y. Wei, J. Xia, B. Xing, P. Ma, J. Lin, *Adv. Sci.* **2017**, *4*, 1600540.

Table 1. Electronic Bandgap energies of 2D materials from monolayer to bulk.

Layer Number	Semimetal	Semiconductor			Insulator
	Graphene [eV][10,11]	BP [eV][20,21]	InSe [eV] [26,27]	TMDs (MoS_2) [eV][28]	*h*-BN [eV][24]
Monolayer	0	~2.0	2.2	1.90	4.64
Bilayer	0	~1.3	1.82	1.60	4.64
Trilayer	0	~1.0	1.68	1.45	4.64
Bulk	-0.04	0.30	1.26	1.29	4.47

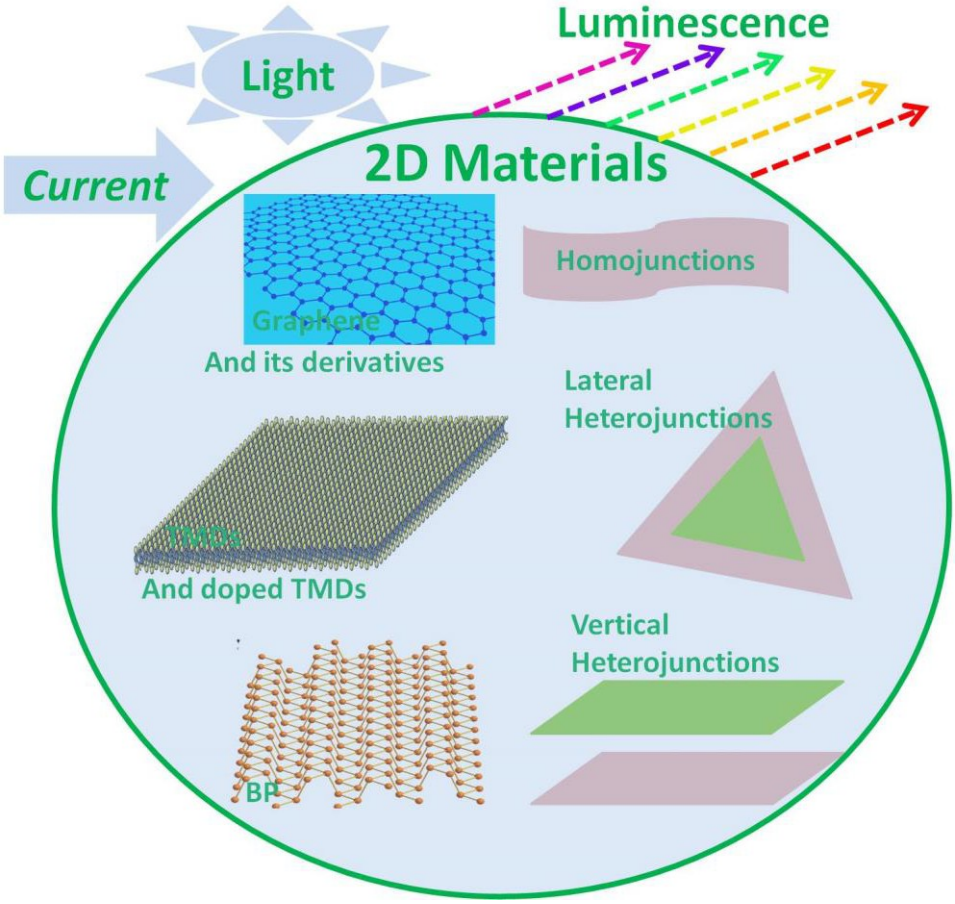

Figure 1. Schematic of luminescence in 2D systems in cluding graphene and its derivatives, TMDs and doped TMDs, recently discovered 2D layered BP crystals and homo- and heterojunctions based on 2D materials.

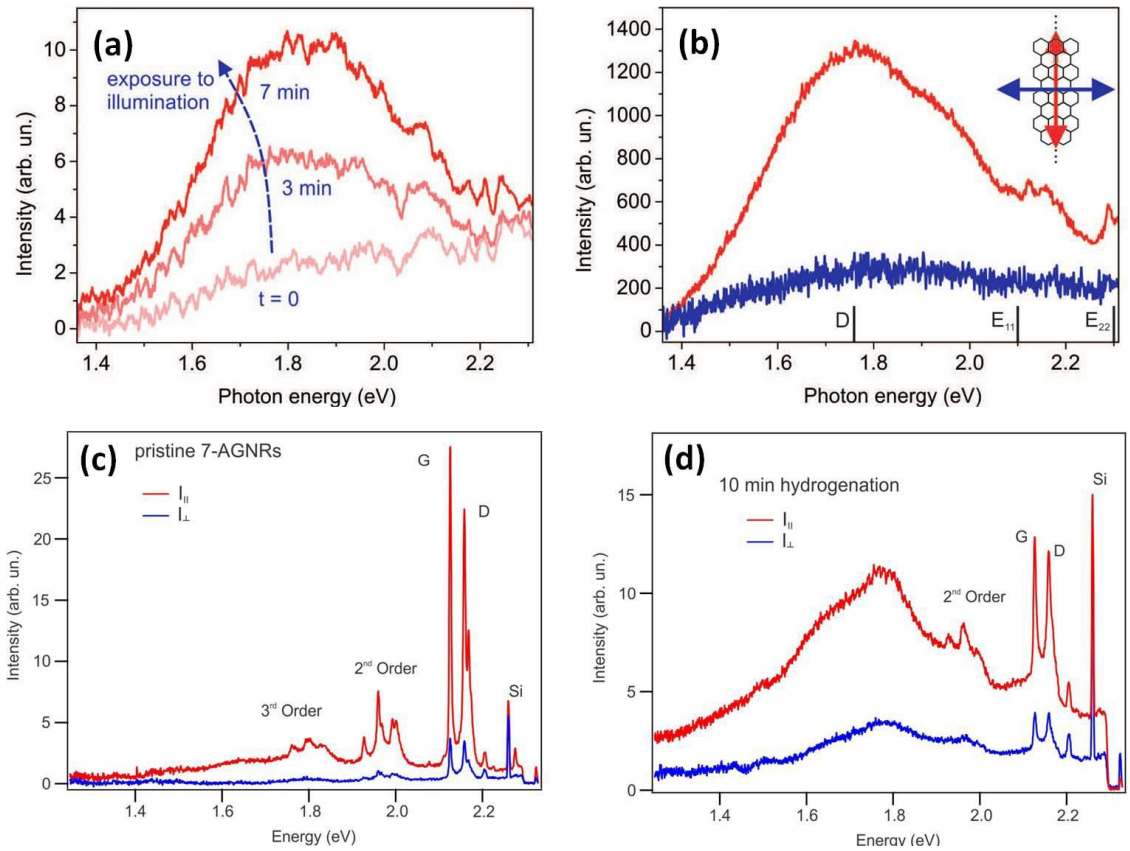

Figure 2. PL in graphene nanoribboms. (a) The enhanced PL spectra when the GNR sample is continuously exposed to 440 nm radiation for 3 and 7 min. (b) The PL spectra with the polarizer and analyzer polarization directions are both along with the ribbon axis, (red vertical arrow) or perpendicular to the ribbon axis (blue horizontal arrow). (c) PL and Raman spectra of the fabricated GNRs on SiO_2 substrate measured in a UHV chamber with the excited laser light (532 nm) polarized parallel (red line) and perpendicular (blue line) to the GNR axis, respectively. (d) PL and Raman spectra of the system after 10 minutes of atomic hydrogen exposure with the excited laser light (532 nm) polarized parallel (red line) and perpendicular (blue line) to the GNR axis, respectively.[94] Copyright 2017, American Chemical Society.

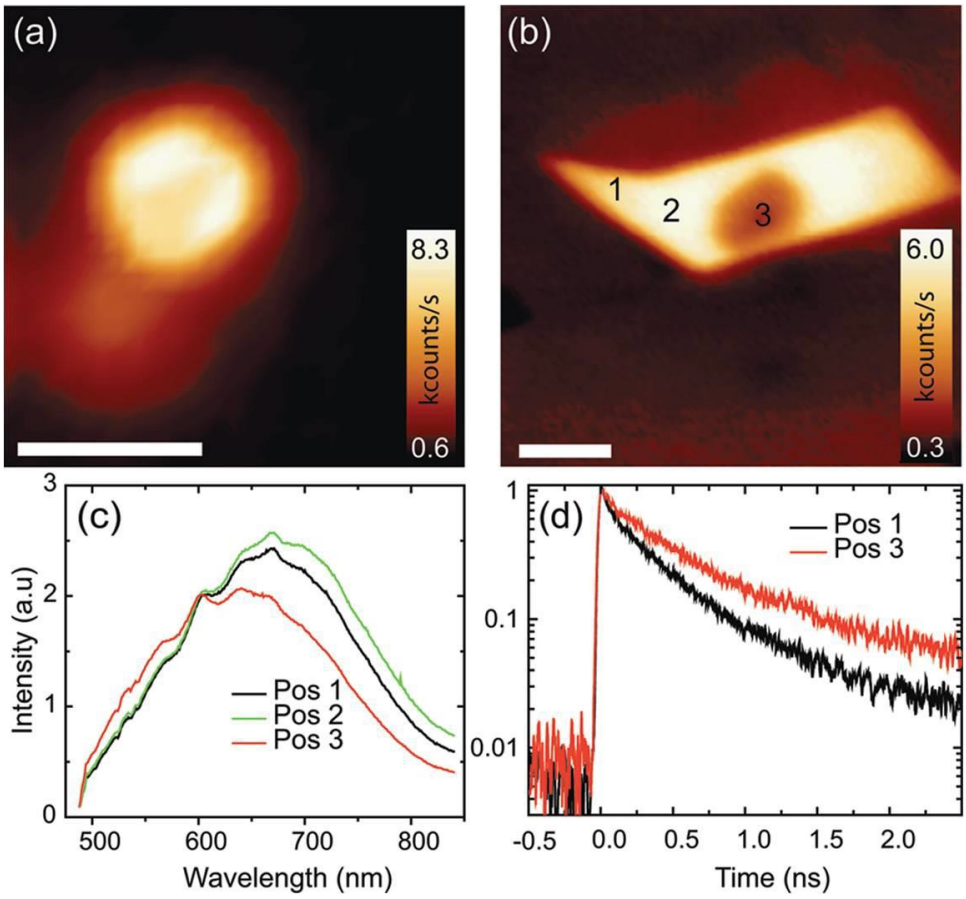

Figure 3. PL in monolayer graphene treated by oxygen plasma (a) Confocal PL image with spatially localized emission for a graphene flake after 3 s oxidation. Scale bar: 5 μm. (b) Confocal PL image with uniform emission for a graphene flake after 5 s oxidation. Scale bar: 10 μm. (c) PL spectra for graphene located at the positions indicated in (b). (d) PL transients for graphene detected at the positions marked in (b).[50] Copyright 2009, American Chemical Society.

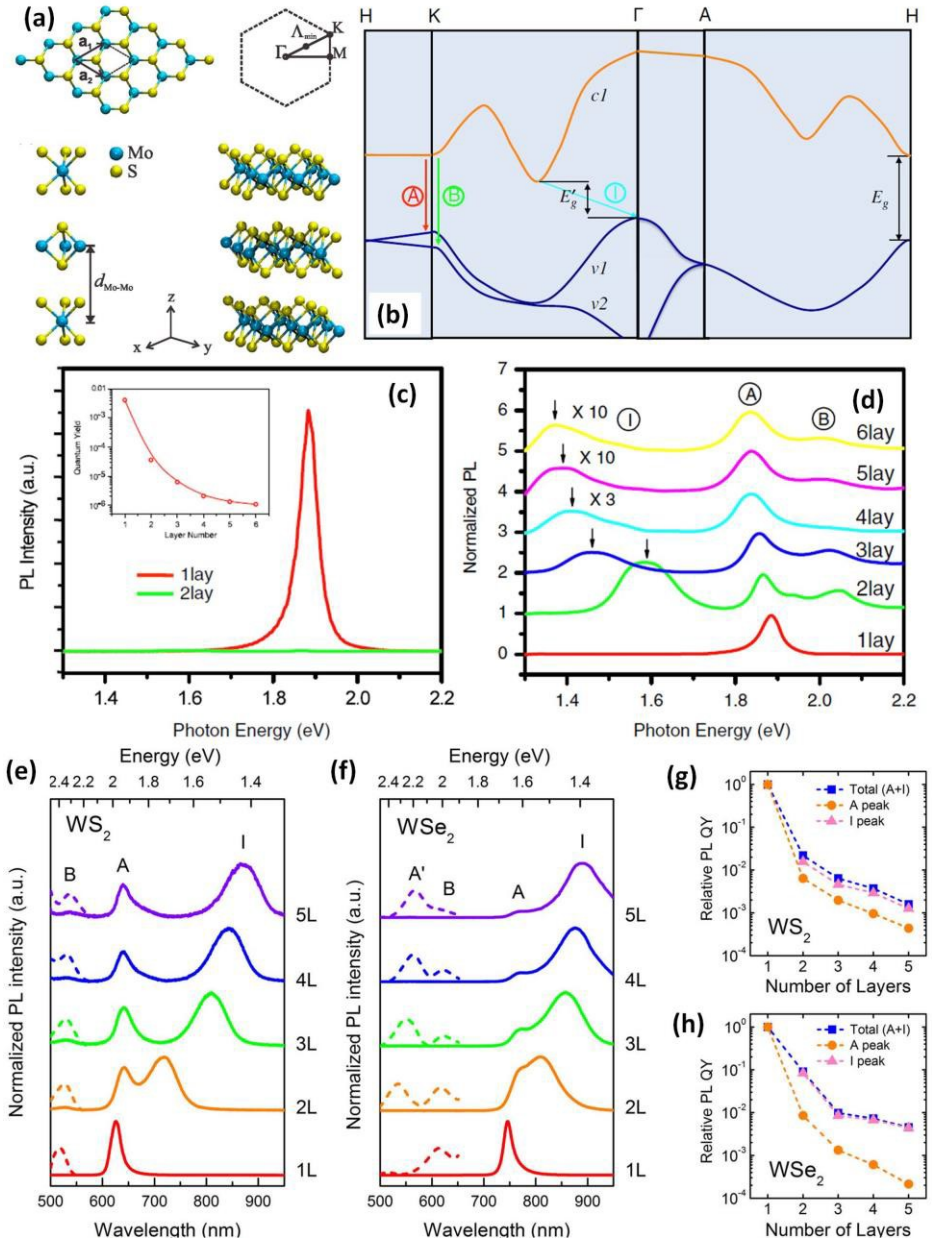

Figure 4. PL in 2D TMDs. (a) Lattice structure. The top left panel exhibits the top view of the lattice structure for a monolayer of MoS_2. The top right panel shows the Brillouin zone. The bottom panel demonstrates 2H-stacking tri-layer MoS_2.[28] Copyright 2014, The American Physical Society. (b) Simplified band structure of bulk MoS_2. The lowest conduction band is named *c*1, while the highest split valence bands are named *v*1 and *v*2, respectively. *A* and *B* are the direct-gap transitions, while *I* is the indirect-gap transition. E'_g is the indirect gap for the bulk, while E_g is the direct gap for the monolayer. (c) PL spectra of mono- and bilayer mechanically exfoliated MoS_2. Inset: Layer number dependent Quantum yield. (d) Normalized PL spectra by the intensity of peak A for 2D MoS_2 crystals with layer number from 1 to 6.[19] Copyright 2010, The American Physical Society. (e) Normalized PL spectra of 2D WS_2 nano flakes prepared by mechanical exfoliation method. (f) Normalized PL spectra of 2D WSe_2 nano flakes prepared by mechanical exfoliation method. (g) Layer number dependent PL QY for WS_2; (h) Layer number dependent PL QY for WSe_2.[100] Copyright 2013, American Chemical Society.

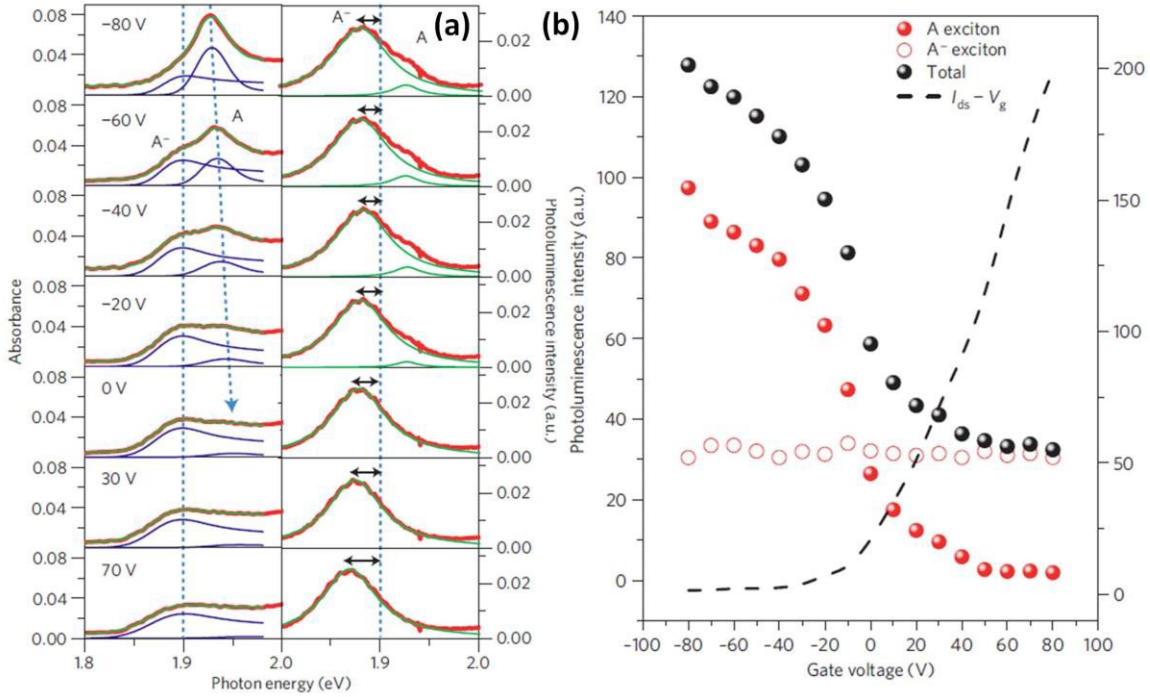

Figure 5. PL in monolayer MoS_2 modulated by gate voltage. (a) Gate voltage dependence of the optical response of a monolayer MoS_2, including absorption (left panel) and photoluminescence (right panel) spectra (red lines) in the range of 1.8-2.0 eV. for the indicated back-gate voltages. A stands for the exciton and A^- stands for the trion. (b) Gate voltage dependence of the integrated PL intensity (left) for A the exciton and $A^-$the trion as well as their total intensity. The gate voltage dependent source drain current is shown by the black dash line.[40] Copyright 2012, Nature Publishing Group.

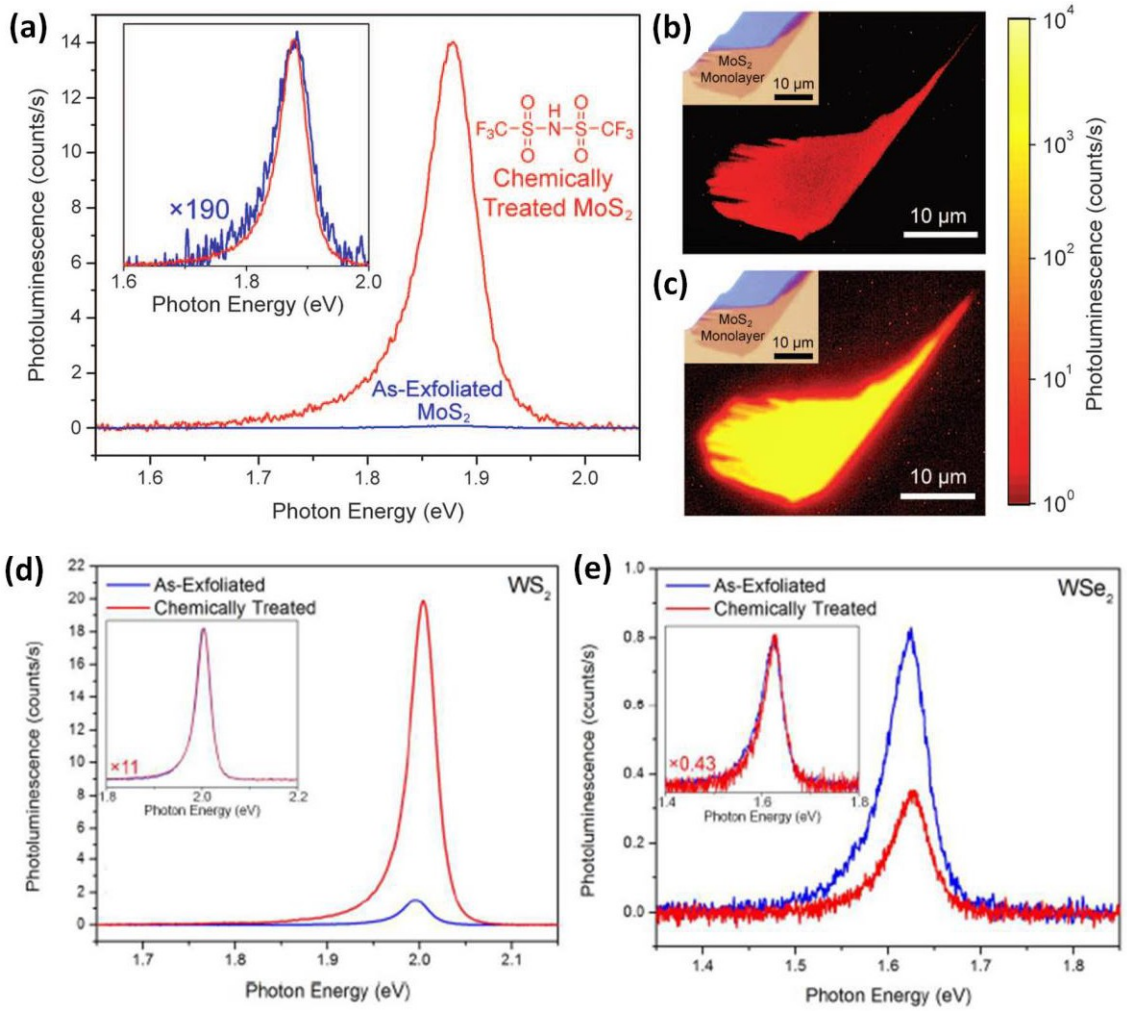

Figure 6. PL in TMDs modulated by chemical treatment (a) PL spectra of the exfoliated monolayer MoS_2 and TFSI-treated sample. Inset: normalized spectra. PL images of a monolayer MoS_2 sample before (b) and after (c) chemical doping. Inset: the corresponding optical images.[106] Copyright 2015, American Association for the Advancement of Science. PL spectra for mechanically exfoliated monolayer TMDCs before and after TFSI treatment (d) WS_2 and (e) WSe_2. The inset in each figure shows the corresponding normalized spectra for the exfoliated and TFSI treated samples.[46] Copyright 2016, American Chemical Society.

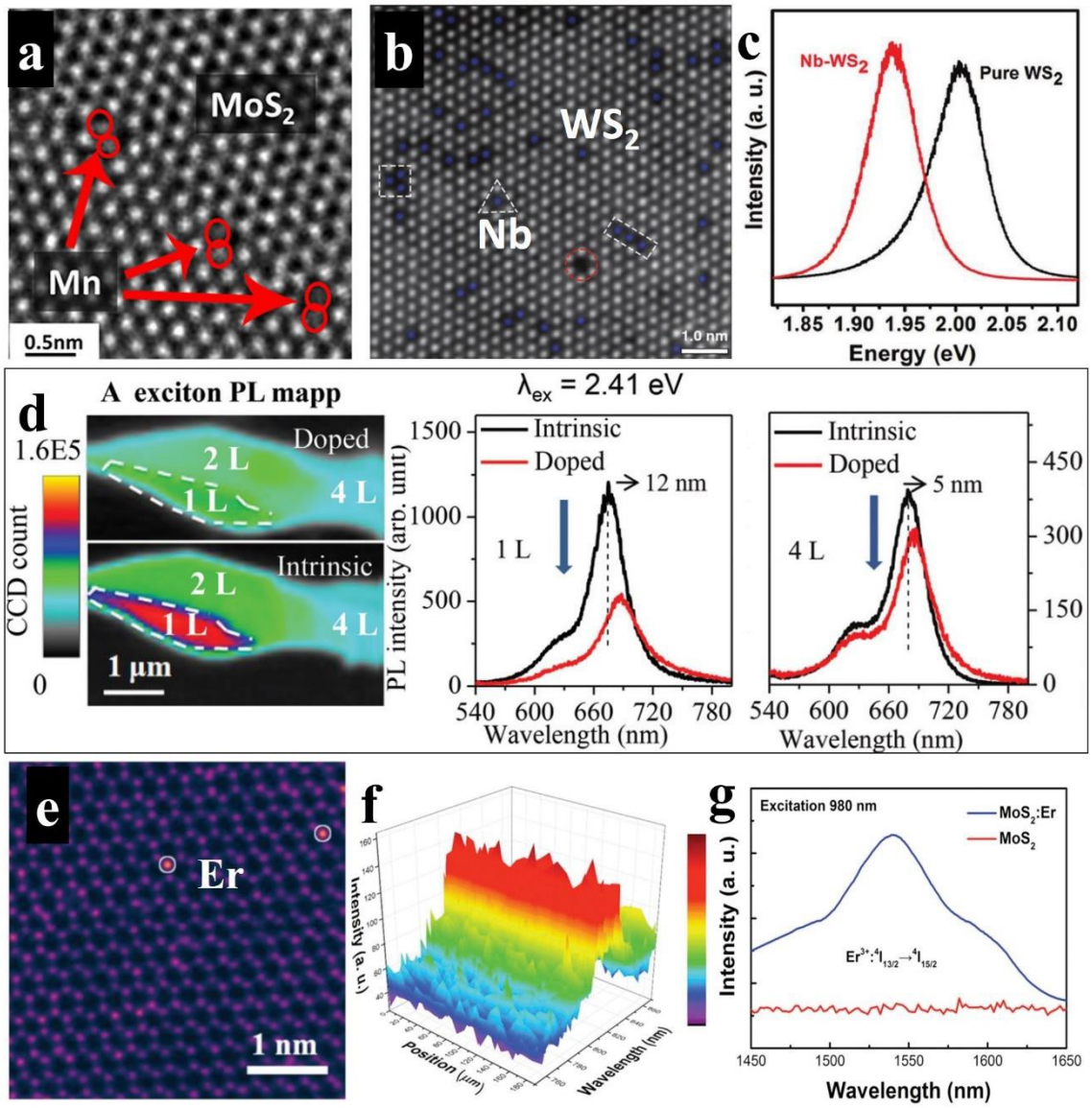

Figure 7. PL in doped 2D TMDs. (a) Atomic scale CS-STEM image of Mn-doped monolayer MoS_2 nanosheets.[136] Copyright 2015, American Chemical Society. (b) Structure model attained from HAADF-STEM image displaying the distribution of Nb dopants in WS_2 nanosheets. (c) The PL spectra of monolayer undoped WS_2 and Nb doped WS_2 nanosheets.[137] Copyright 2016, Wiley-VCH. (d) PL mapping image and spectra of the intrinsic and reduced BV doped MoS_2 films.[138] Copyright 2014, Royal Society of Chemistry. (e) Atomic scale CS-STEM image of Er-doped MoS_2 nanosheets. (f) The PL mapping image of upconversion peaks around 800 nm over an area of 200 µm x 100 µm in Er-doped MoS_2 samples. (g) The downconversion PL emitted at around 1540 nm of Er-doped MoS_2 nanosheets under 980 nm excitation.[139] Copyright 2016, Wiley-VCH.

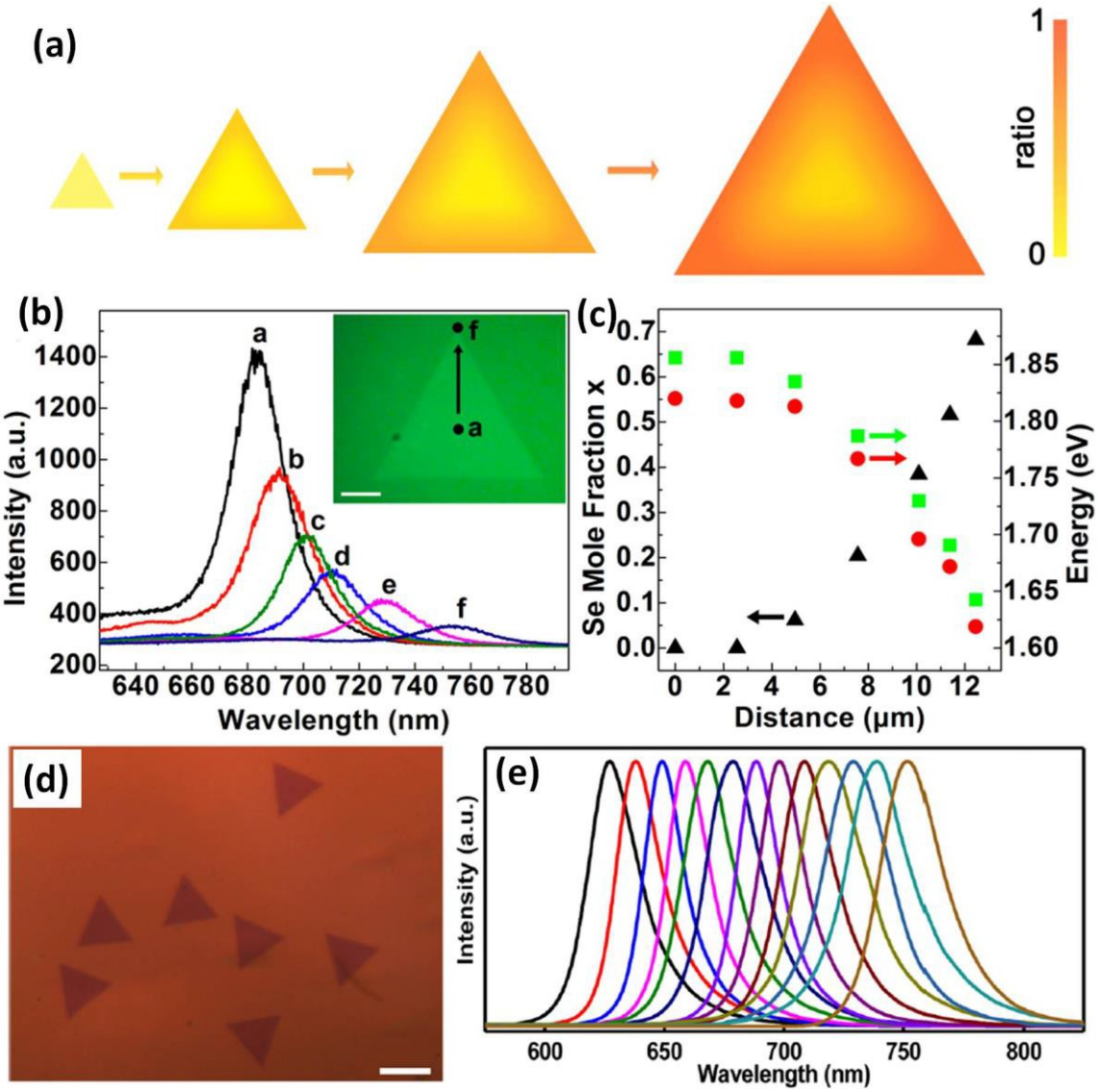

Figure 8. PL in composition graded TMDs nanosheets. (a) Schematic process of the growth of the lateral composition graded bilayer $MoS_{2(1-x)}Se_{2x}$ nanosheet. (b) Position (composition) dependent PL spectra of an individual nanosheet with the postion changed gradully from the center (position **a**) to the edge (**f**) of the nanosheet. Inset: Optical microscopy of the nanosheet. The orrow indicates the postions from the center **a** to the edge **f**. (c) The postion dependent Se ratios and bandgap values from the center to the edge in the nanosheet.[140] Copyright 2015, American Chemical Society. (d) Optical microscopy image of a series of triangular monolayer $WS_{2x}Se_{2-2x}$ nanosheets. (e) PL spectra of a series of composition tunable monolayer $WS_{2x}Se_{2-2x}$ nanosheets.[141] Copyright 2016, American Chemical Society.

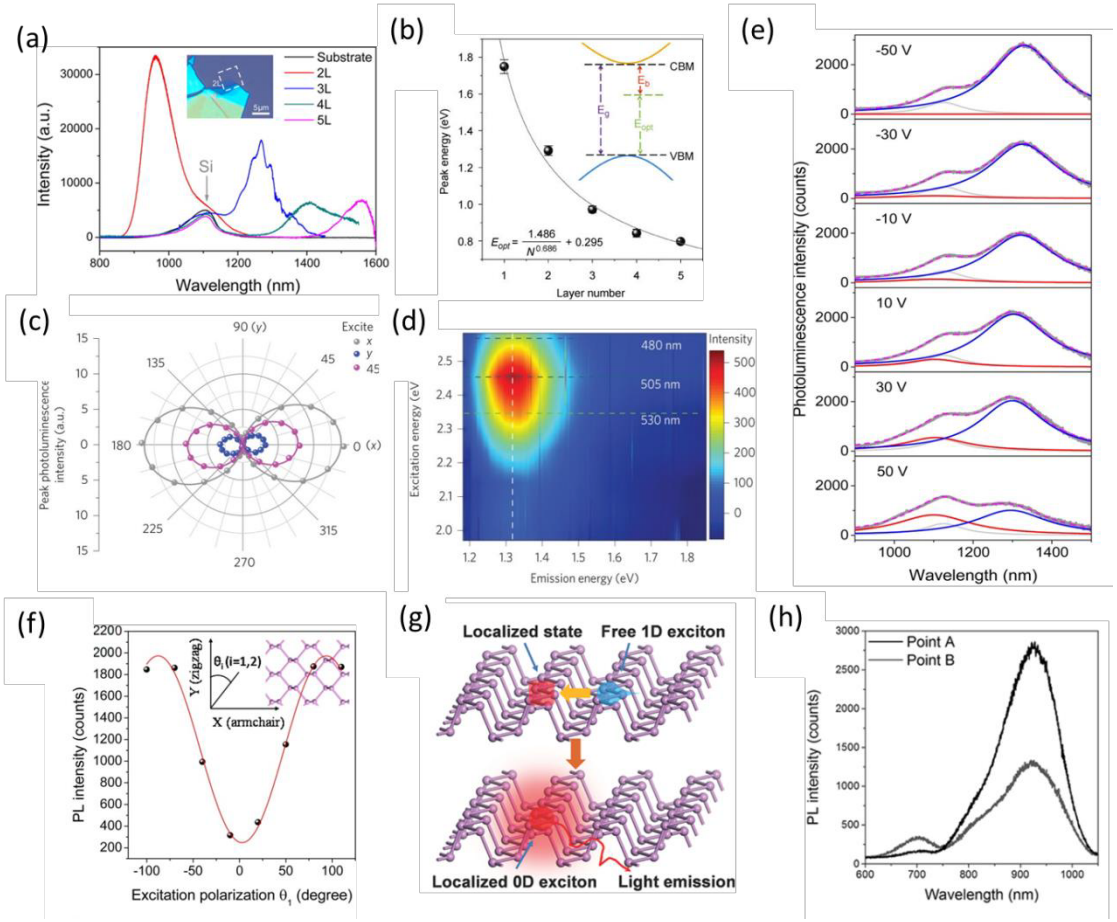

Figure 9. PL in 2D BP. (a) PL spectra of BP nanosheets with different thickness. The inset shows the optical image of bilayer phosphorene.[146] Copyright 2014, American Chemical Society. (b)Peak energy of PL spectra as a function of layer number for few-layer phosphorene. The inset shows the band diagram of phosphorene (upright) and simulation equation for optical band gaps (lower-left).[20] Copyright 2015, Nature Publishing Group. (c) PL peak intensity as a function of detection angles for different polarized excitations. (d) PL intensity mapping as function of both emission and excitation energies.[151] Copyright 2015, Nature Publishing Group. (e) PL spectra under different gate biases. (f) PL intensity as a function of excitation polarization angle. The inset shows the schematic of phosphorene lattice and coordinates for polarization angles.[153] Copyright 2016, American Chemical Society. (g) Schematic of dimensionality modification of BP excitons. (h) PL spectra of different spots on phosphorene/PECVD oxide.[158] Copyright 2016, Wiley-VCH.

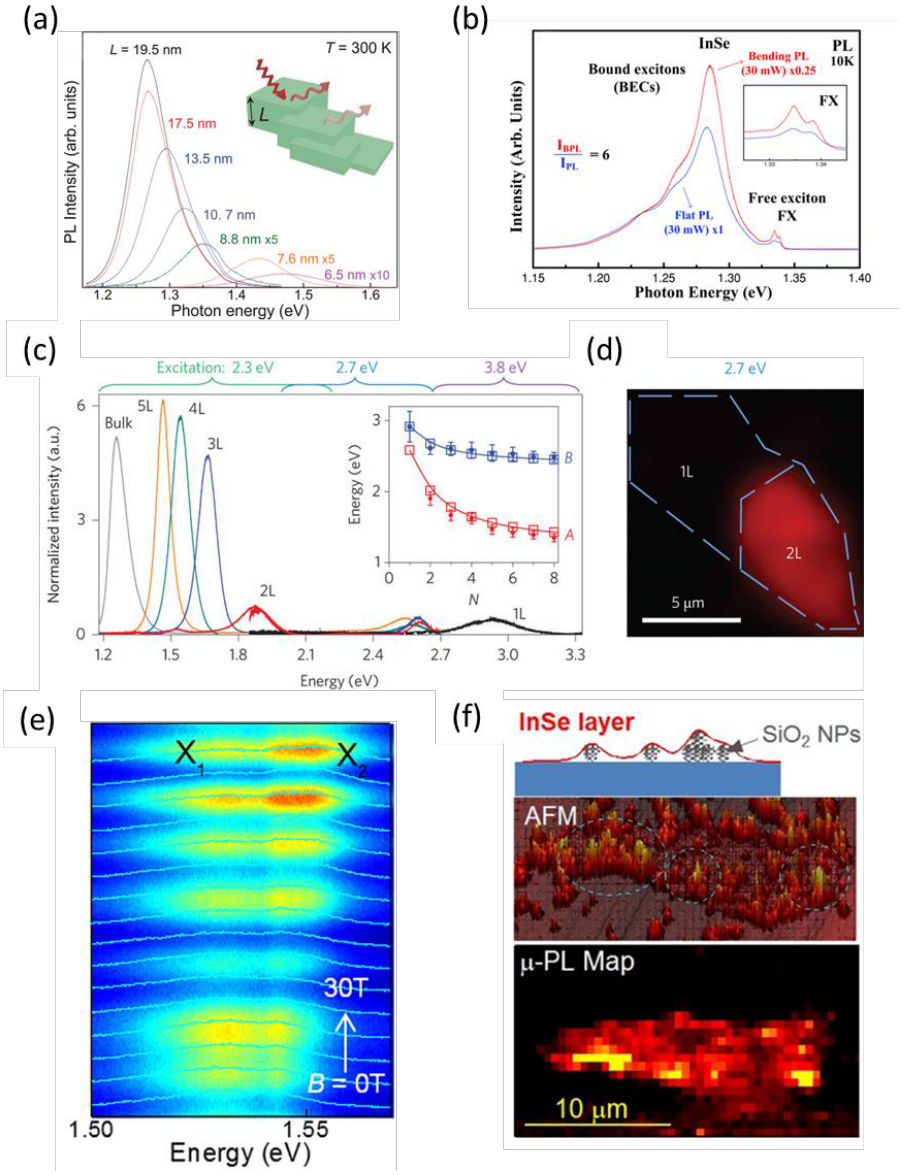

Figure 10. PL in 2D InSe. (a) PL spectra of different thick InSe nanosheets at room temperature. The inset shows the schematic of PL emitted from flakes with different thickness.[162] Copyright 2013, Wiley-VCH. (b) PL spectra of InSe nanosheets under both bending and flat states at 10 K. The inset shows the difference of FX luminescence from both bending and flat states.[163] Copyright 2015, Wiley-VCH. (c) PL spectra of different thick InSe nanosheets by lasers with three excitation energies. The inset shows the energy of both A and B peaks are a function of layer number, which are obtained by both experimental and theoretical ways. (d) PL intensity mapping of both mono- and bilayer InSe.[26] Copyright 2016, Nature Publishing Group. (e) PL intensity mapping of ultrathin InSe flake as a function of *B* and photon energy.[164] Copyright 2016, Nature Publishing Group. (f) Top: the schematic of SiO_2 NPs under InSe layer, which are used for manipulating the luminescence of InSe nanosheet. Middle: Morphology mapping of InSe nanosheet measured by AFM. Bottom: The integrated μPL intensity mapping of InSe.[167] Copyright 2016, American Chemical Society.

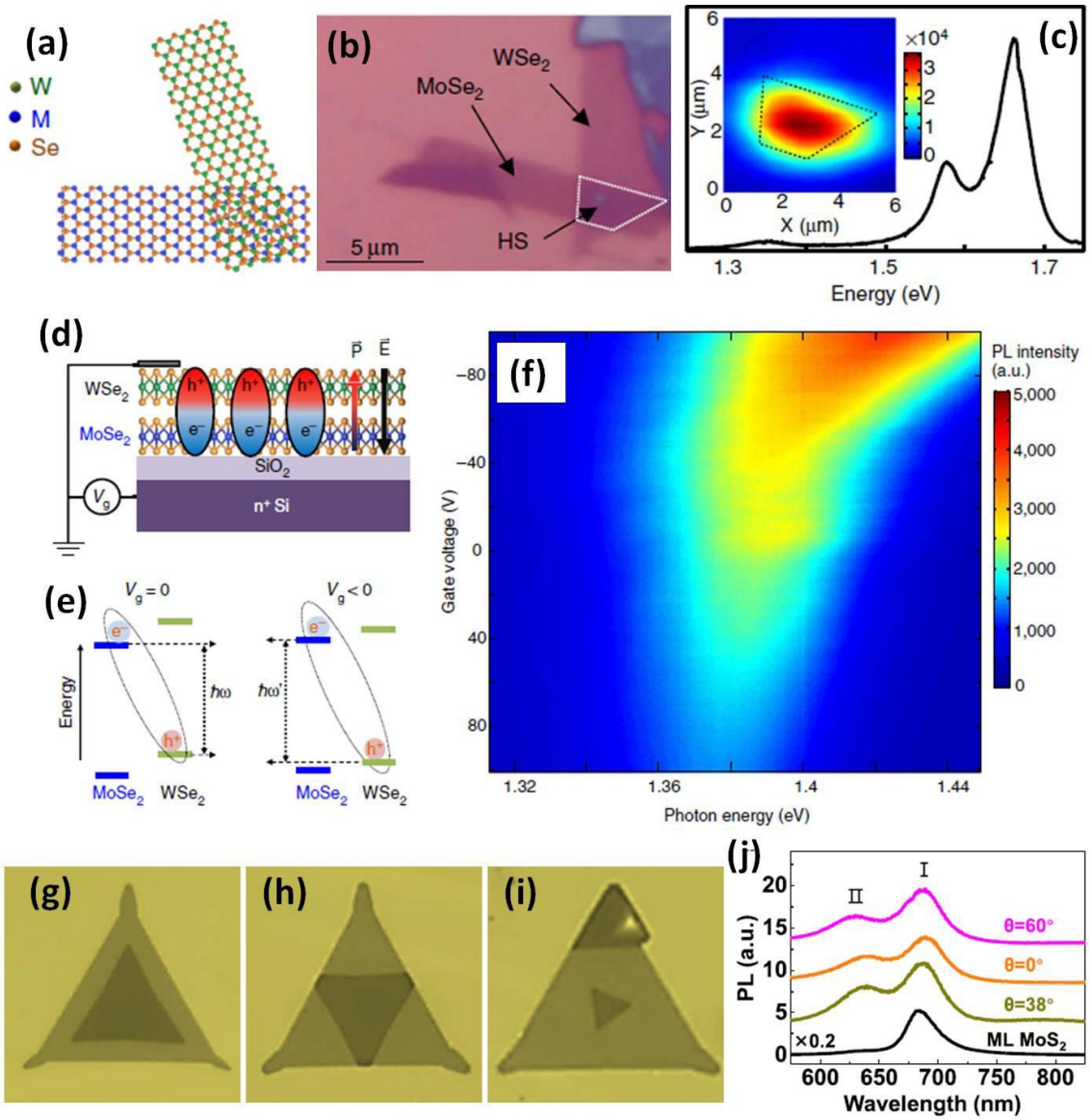

Figure 11. Optical response of monolayer TMDs vertical heterostructure. (a) Schematics of the $MoSe_2/WSe_2$ heterostructure with WSe_2 on the top. (b) Micrograph of a $MoSe_2/WSe_2$ heterostructure. The white dashed line outlines the $MoSe_2/WSe_2$ heterostructure. (c) The PL spectrum of the heterostructure excited by laser (20 mW, 2.33 eV) measured at room-temperature. Inset: spatial mapping image of integrated PL intensity in the energy range of 1.273-1.400 eV. The black dashed line outlines the heterostructure region. (d) Gate control of the dipole in $MoSe_2/WSe_2$ heterostructure with WSe_2 on the top. (e) Gate control of the band alignment and the interlayer relative band-offset. (c) Mapping image of the interlayer excitonic emission tuned by the applied gate voltage excited by laser (70 mW, 1.744 eV). [177] Copyright 2015, Nature Publishing Group. Micrograph of MoS_2/WS_2 bilayers with WS_2 monolayer on top stacked with different twist angles of 0° (g), 60° (h) and 38° (i). (j) PL of MoS_2 monolayer and the twisted bilayers.[173] Copyright 2017, American Chemical Society.

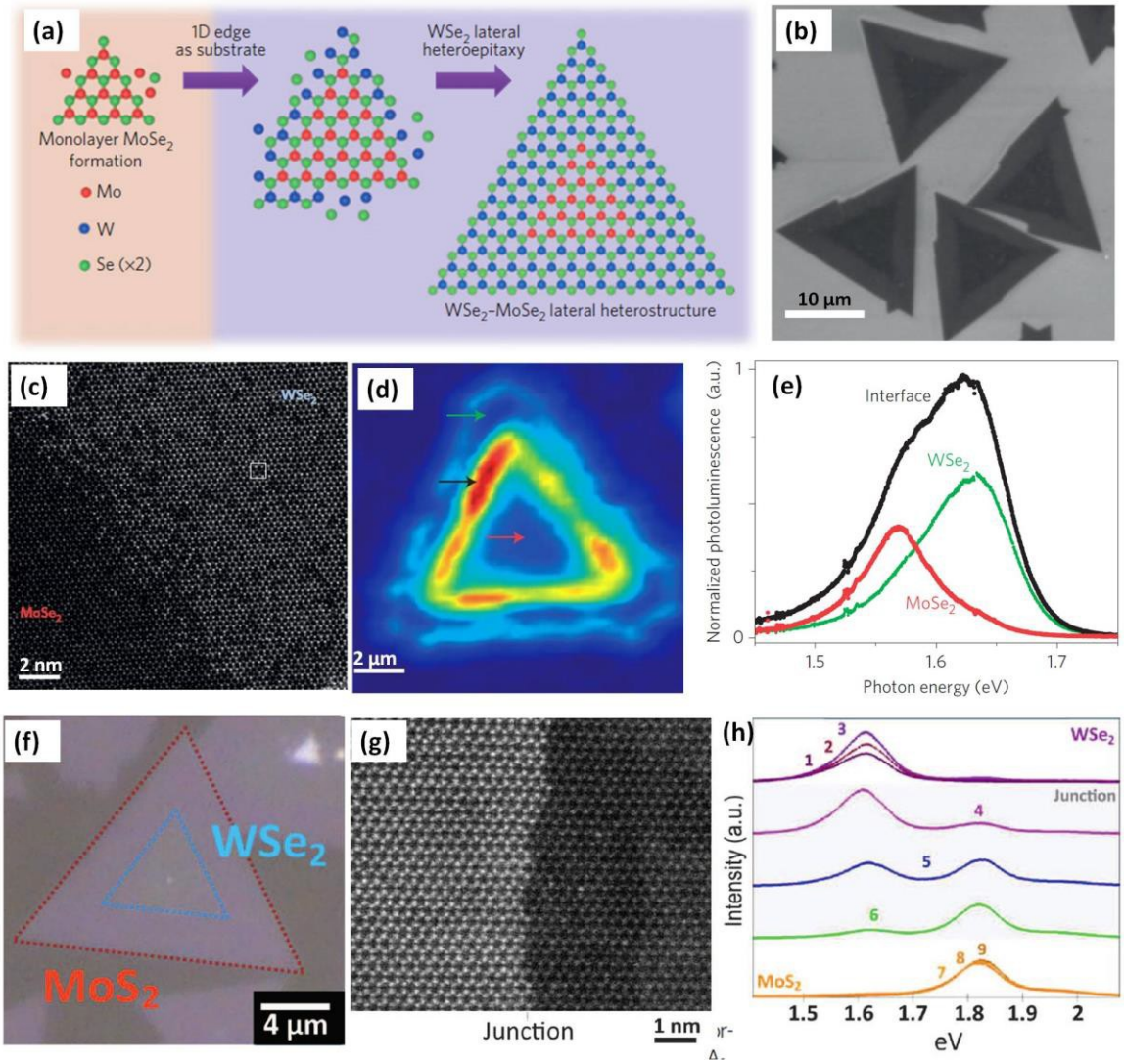

Figure 12. Optical response of monolayer TMDs lateral heterostructure (a) Schematic of the in-plane heteroepitaxy of $MoSe_2/WSe_2$ lateral heterostructure. (b) SEM image of the triangular $MoSe_2/WSe_2$ lateral heterostructure. (c) High-resolution TEM image of the 1D lateral interface of the $MoSe_2/WSe_2$ lateral heterostructure. (d) Integrated PL intensity mapping image of $MoSe_2/WSe_2$ lateral heterostructure. (e) PL spectra of $MoSe_2/WSe_2$ lateral heterostructure measured at the three positions ($MoSe_2$, WSe_2, and the interface) marked by the colored arrows (red, green and dark) in d.[180] Copyright 2014, Nature Publishing Group. (f) SEM image of the triangular WSe_2/MoS_2 lateral heterostructure. (g) High-resolution TEM image of the 1D lateral interface of the WSe_2/MoS_2 lateral heterostructure. (h) PL spectra of $MoSe_2/WSe_2$ lateral heterostructure.[181] Copyright 2015, American Association for the Advancement of Science.

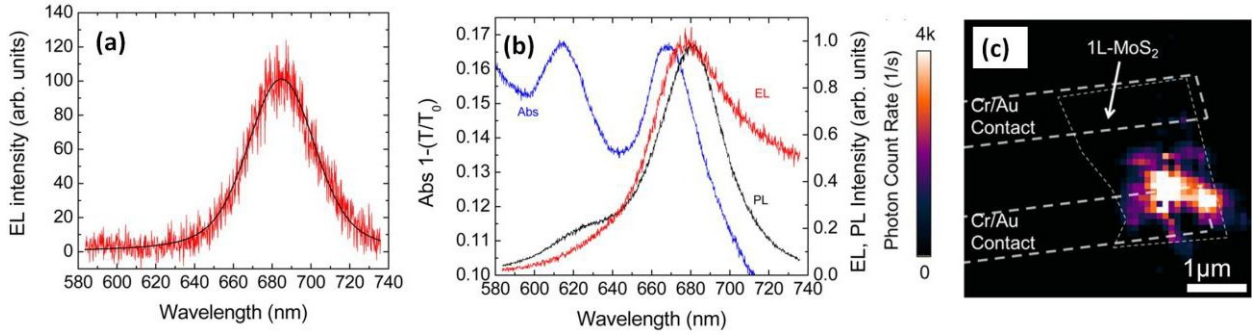

Figure 13. EL in monolayer MoS_2. (a) The optimum EL spectrum of monolayer of MoS_2 when the source drain voltage is biased with 5 V and the current is 100 μA. (b) The spectra of absorption (Abs), EL, and PL of monolayer of MoS_2. The EL spectrum is measured MoS_2 when the source drain voltage is biased with 8 V and the current is 164 μA.(c) The EL mapping image of EL emission. The positions of source and drain electrode are indicated by thick white dashed lines, and the monolayer MoS_2 sample is highlighted by thin gray dashed lines. The EL spectrum is measured MoS_2 when the source drain voltage is biased with 4 V and the current is 180 μA.[185] Copyright 2013, American Chemical Society.

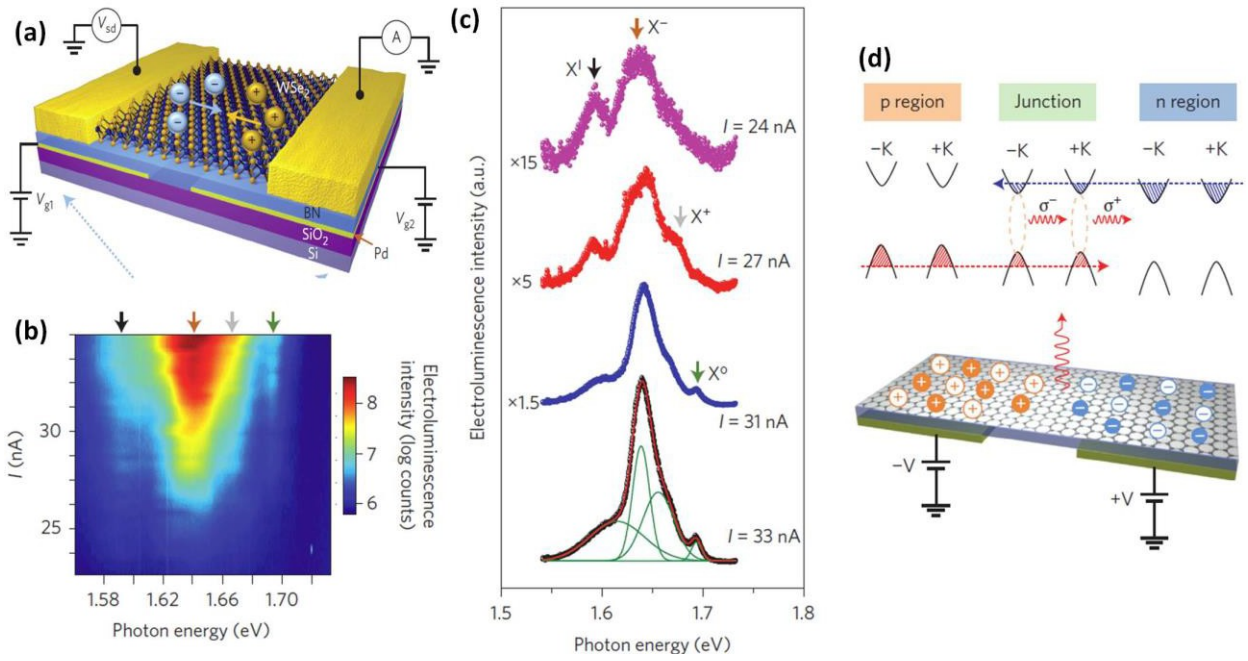

Figure 14. EL in the lateral p-n homojunction based on monolayer WSe_2. (a) Schematic of the lateral p-n homojunction. The exfoliated monolayer WSe_2 and multilayer *h*-BN serve as the channel semiconductor and bottom gate dielectric, respectively, and well patterned palladium as the individual backgate electrodes (V_{g1} and V_{g2}), and gold/vanadium (60/6 nm) as source (S) and drain (D) contacts. The device is fabricated on a silicon substrate. (b) EL intensity as a function of bias (source-drain) current and photon energy measured at 60 K. (c) EL spectra at different bias currents. The bottom spectrum (33 nA) is fit by four Gaussian lineshapes. (d) Schematics of EL generation by plotting the band diagram and the lateral p-n homojunction. Dashed red and blue arrows indicate the hole and electron flow directions, respectively. Filled and empty circles indicate carriers in the +K and − K valleys, respectively.[169] Copyright 2014, Nature Publishing Group.

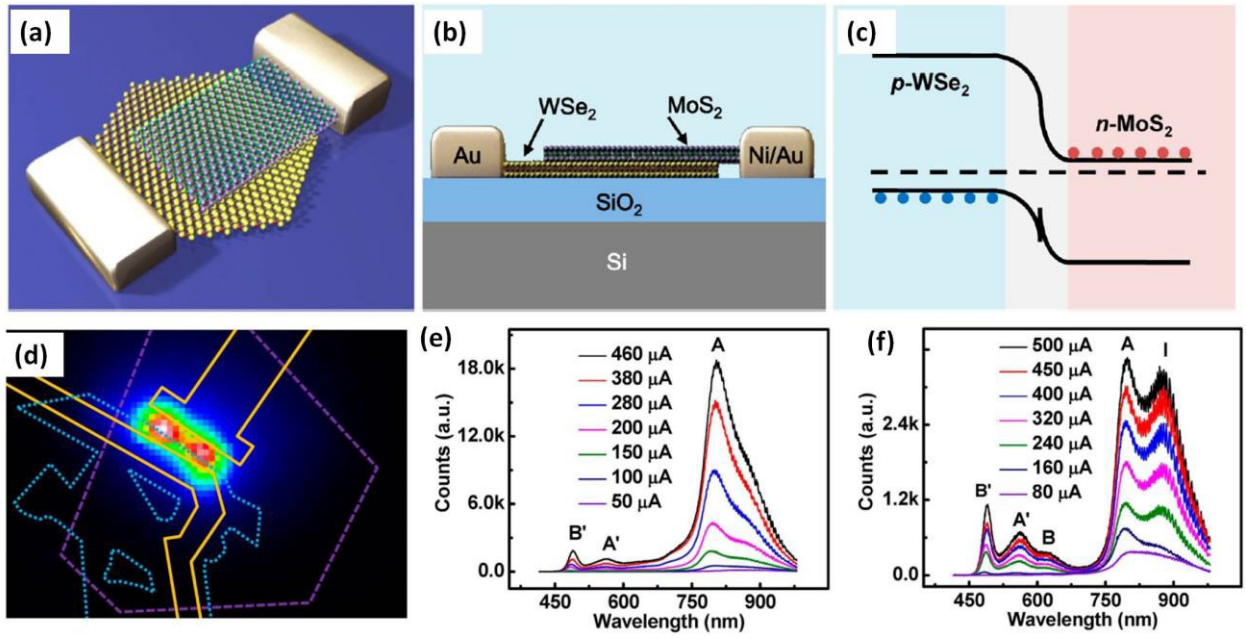

Figure 15. EL in vertical HS based on 2D TMDs. (a) Top and (b) side view for the schematic of the vertical HS based on mechanically exfoliated MoS_2 and CVD-grown WSe_2.(c) The ideal band structure of WSe_2/MoS_2 p-n junction with zero bias. (d) The false color EL image of the WSe_2/MoS_2 p-n junction under an injection current of 100 μA. The purple dashed line indicates monolayer CVD-grown WSe_2, the blue dotted line highlights the transferred MoS_2 and the golden solid line plots the electrodes. (e) The EL spectra of the fabricated monolayer WSe_2/MoS_2 p-n junction with different injection current. (f) The EL spectra of the fabricated bilayer WSe_2/MoS_2 p-n junction with different injection current.[195] Copyright 2014, American Chemical Society.

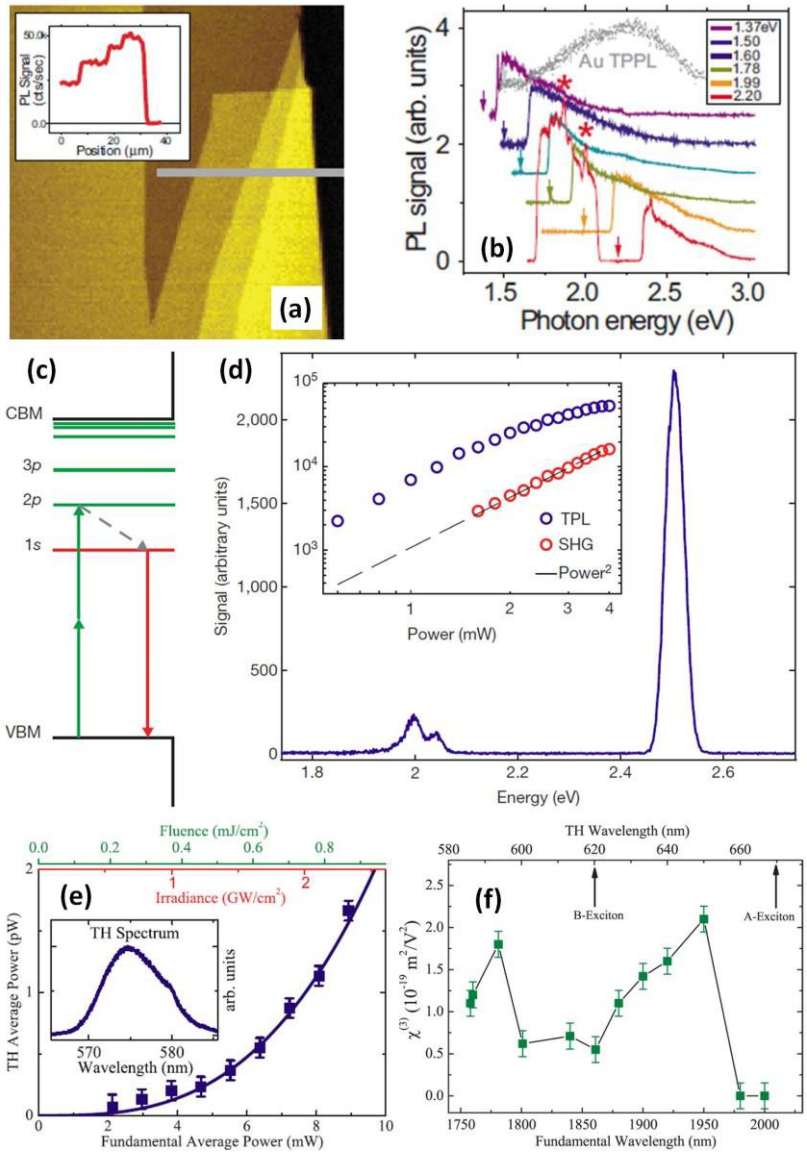

Figure 16. Nonlinear optics in 2D materials. (a) PL image of the mechanically exfoliated graphene sample with different layer numbers excited by 1.5 eV femtosecond laser pulses with signal integrated from 1.66 to 3.11 eV. Inset is the PL intensity along the line cut as marked in the main panel. (b) Representative PL spectra of a few-layer graphene sample under excitation of various frequencies, as marked by the arrows with different colors. The *G* and 2*D* Stokes Raman modes are marked by asterisks "*".[202] Copyright 2010, American Physics Society. (c) Schematic of the TPL process in monolayer WS_2. (d) Emission spectrum of monolayer WS_2 excited by an ultrafast fs laser with energy of 1.25 eV measured at 10 K. The inset shows the quadratic power dependence of both TPL and SHG singals. The TPL signal employs the trion peak amplitude. The trion peak amplitude is selected as our TPL signal. [51] Copyright 2014, Nature Publishing Group. (e) The power dependence of the third harmonic for graphene sample. The solid squares are the experimental data, and the solid line is a cubic fit curve. Inset shows the THG spectrum excited by fs laser of 1720.4 nm.[222] Copyright 2013, American Physics Society. (f) The extracted third-order nonlinear susceptibility of ultrathin MoS_2 flakes as a function of the incident wavelength (bottom axis)

and the generated THG wavelength (top axis).[223] Copyright 2013, American Chemical Society.

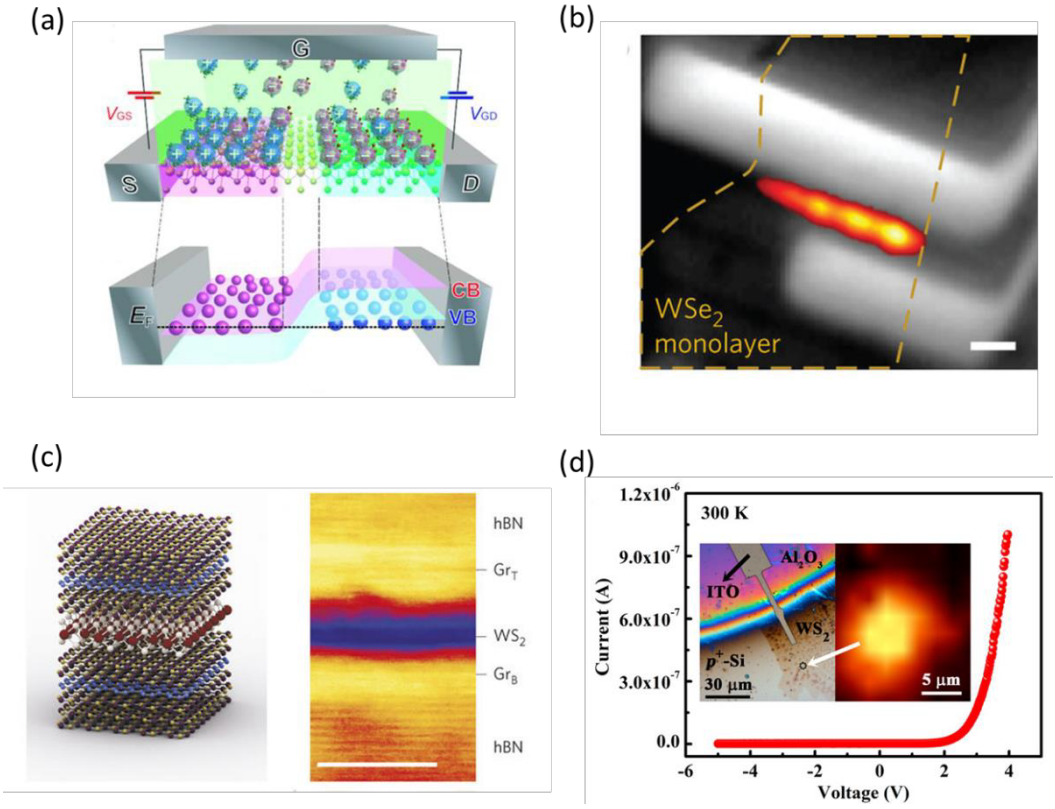

Figure 17. Applications in Light-emitting devices. (a) Schematic of light-emitting transistors based on WSe_2.[30] Copyright 2014, American Association for the Advancement of Science. (b) EL image of LEDs based on WSe_2 p-n junctions. Scale bar, 2 μm.[169] Copyright 2014, Nature Publishing Group. (c) Left: Schematic of heterostructure used for LED. Right: Cross-sectional STEM image of the heterostructure. Scale bar, 5 nm.[29] Copyright 2015, Nature Publishing Group. (d) I−V characteristics of LED based on WS_2 heterostructure. The inset shows the optical picture of the LED and EL map of the area where white arrow indicated.[193] Copyright 2016, American Chemical Society.

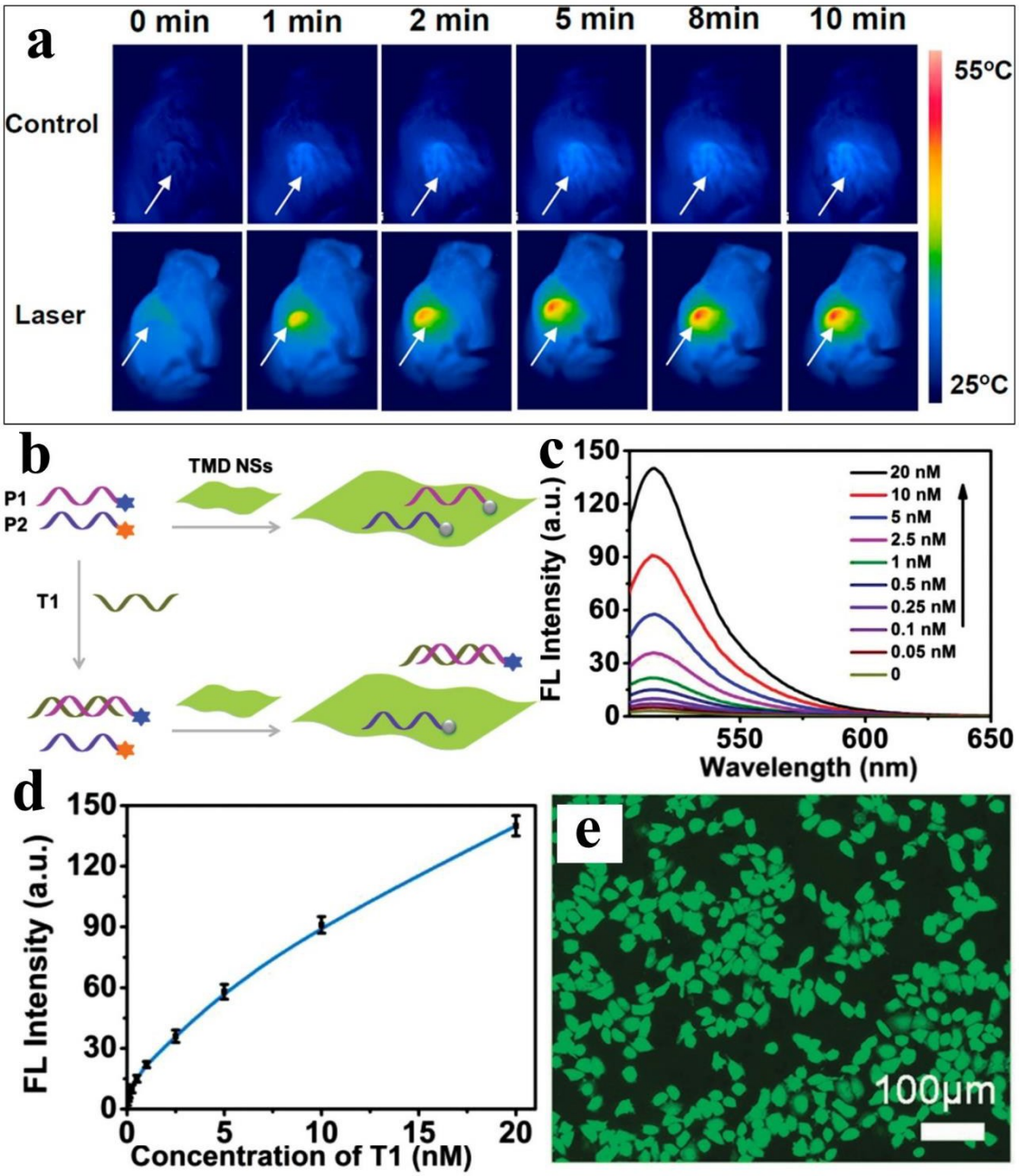

Figure 18. Applications in biomedicine. (a) IR thermal images of 4T1-tumor-bearing mice with injection of WS_2:Gd^{3+}-3-PEG (lower row, dose = 20 mg/kg), under 808 nm laser irradiation with a power density 0.5 W/cm^2 recorded at different time intervals.[243] Copyright 2015, American Chemical Society. (b) Schematic diagram of monolayer TMD nanosheet-based multiplexed luminescent DNA detection. (c) The PL spectra of TaS_2 nanosheet-based nanosensors under different concentrations of DNA. (d) The sensitivity analysis of DNA detection with monolayer TaS_2 nanosheets.[244] Copyright 2015, Wiley-VCH. (e) Intracellular ROS detection treated with MoS_2@Fe_3O_4-ICG nanoflowers, triggered by 808 nm laser (1.0 W cm^{-2}, 5 min).[246] Copyright 2017, Wiley-VCH.

TOC

Luminescence in two-dimensional (2D) materials is not only essential for structural and properties characterization but also significantly important for devices applications in optoelectronics, biomedicine and future quantum technologies. Herein, we review recent advances and new developments in luminescence, including the luminescent mechanism, characterizations, performance and applications based on 2D materials and van der Waals heterostructures.

Keywords: two-dimensional materials, photoluminescence, electroluminescence, nonlinear optics, van der Waals heterostructures

W.J. Jie, Z.B. Yang, G.X. Bai, J.H. Hao*

Luminescence in Two-Dimensional Materials and van der Waals Heterostructures